



JADES Data Release 3: NIRSpec/Microshutter Assembly Spectroscopy for 4000 Galaxies in the GOODS Fields

Francesco D'Eugenio^{1,2,23} , Alex J. Cameron^{3,23} , Jan Scholtz^{1,2,23} , Stefano Carniani^{4,23} , Chris J. Willott^{5,23} , Emma Curtis-Lake⁶ , Andrew J. Bunker³ , Eleonora Parlanti⁴ , Roberto Maiolino^{1,2,7} , Christopher N. A. Willmer⁸ , Peter Jakobsen⁹ , Brant E. Robertson¹⁰ , Benjamin D. Johnson¹¹ , Sandro Tacchella^{1,2} , Phillip A. Cargile¹¹ , Tim Rawle¹² , Santiago Arribas¹³ , Jacopo Chevallard³ , Mirko Curti¹⁴ , Eiichi Egami⁸ , Daniel J. Eisenstein¹¹ , Nimisha Kumari¹⁵ , Tobias J. Looser^{1,2} , Marcia J. Rieke⁸ , Bruno Rodríguez Del Pino¹³ , Aayush Saxena^{3,7} , Hannah Übler^{1,2} , Giacomo Venturi⁴ , Joris Witstok^{1,2} , William M. Baker^{1,2} , Rachana Bhatawdekar¹² , Nina Bonaventura⁸ , Kristan Boyett^{16,17} , Stephane Charlot¹⁸ , A. Lola Danhaive^{1,2} , Kevin N. Hainline⁸ , Ryan Hausen¹⁹ , Jakob M. Helton⁸ , Xihan Ji^{1,2} , Zhiyuan Ji⁸ , Gareth C. Jones³ , Ignas Juodžbalis^{1,2} , Michael V. Maseda²⁰ , Pablo G. Pérez-González¹³ , Michele Perna¹³ , Dávid Puskás^{1,2} , Irene Shivaei¹³ , Maddie S. Silcock⁶ , Charlotte Simmonds^{1,2} , Renske Smit²¹ , Fengwu Sun⁸ , Natalia C. Villanueva^{1,2} , Christina C. Williams^{8,22} , and Yongda Zhu⁸

¹ Kavli Institute for Cosmology, University of Cambridge, Madingley Road, Cambridge CB3 0HA, UK; francesco.deugenio@gmail.com

² Cavendish Laboratory, University of Cambridge, 19 JJ Thomson Avenue, Cambridge CB3 0HE, UK

³ Department of Physics, University of Oxford, Denys Wilkinson Building, Keble Road, Oxford OX1 3RH, UK

⁴ Scuola Normale Superiore, Piazza dei Cavalieri 7, I-56126 Pisa, Italy

⁵ NRC Herzberg, 5071 West Saanich Road, Victoria, BC V9E 2E7, Canada

⁶ Centre for Astrophysics Research, Department of Physics, Astronomy and Mathematics, University of Hertfordshire, Hatfield AL10 9AB, UK

⁷ Department of Physics and Astronomy, University College London, Gower Street, London WC1E 6BT, UK

⁸ Steward Observatory, University of Arizona, 933 North Cherry Avenue, Tucson, AZ 85721, USA

⁹ Cosmic Dawn Center (DAWN), Niels Bohr Institute, University of Copenhagen, Jagtvej 128, DK-2200 Copenhagen, Denmark

¹⁰ Department of Astronomy and Astrophysics, University of California, Santa Cruz, 1156 High Street, Santa Cruz, CA 95064, USA

¹¹ Center for Astrophysics | Harvard & Smithsonian, 60 Garden Street, Cambridge MA 02138, USA

¹² European Space Agency (ESA), European Space Astronomy Centre (ESAC), Camino Bajo del Castillo s/n, 28692 Villafranca del Castillo, Madrid, Spain

¹³ Centro de Astrobiología (CAB), CSICINTA, Cra. de Ajalvir Km. 4, 28850- Torrejón de Ardoz, Madrid, Spain

¹⁴ European Southern Observatory, Karl-Schwarzschild-Strasse 2, 85748 Garching, Germany

¹⁵ AURA for European Space Agency, Space Telescope Science Institute, 3700 San Martin Drive, Baltimore, MD 21210, USA

¹⁶ School of Physics, University of Melbourne, Parkville, 3010 VIC, Australia

¹⁷ ARC Centre of Excellence for All Sky Astrophysics in 3 Dimensions (ASTRO 3D), Australia

¹⁸ Sorbonne Université, CNRS, UMR 7095, Institut d'Astrophysique de Paris, 98 bis bd Arago, 75014 Paris, France

¹⁹ Department of Physics and Astronomy, The Johns Hopkins University, 3400 N. Charles Street, Baltimore, MD 21218, USA

²⁰ Department of Astronomy, University of Wisconsin-Madison, 475 N. Charter Street, Madison, WI 53706, USA

²¹ Astrophysics Research Institute, Liverpool John Moores University, 146 Brownlow Hill, Liverpool L3 5RF, UK

²² NSF's National Optical-Infrared Astronomy Research Laboratory, 950 North Cherry Avenue, Tucson, AZ 85719, USA

Received 2024 April 9; revised 2024 November 17; accepted 2024 December 16; published 2025 February 14

Abstract

We present the third data release of the JWST Advanced Deep Extragalactic Survey (JADES), providing both imaging and spectroscopy in the two GOODS fields. Spectroscopy consists of medium-depth and deep NIRSpec/microshutter assembly spectra of 4000 targets, covering the spectral range 0.6–5.3 μm and observed with both the low-dispersion prism ($R = 30\text{--}300$) and all three medium-resolution gratings ($R = 500\text{--}1500$). We describe the observations, data reduction, sample selection, and target allocation. We measured 2375 redshifts (2053 from multiple emission lines); our targets span the range from $z = 0.5$ up to $z = 13$, including 404 at $z > 5$. The data release includes 2D and 1D fully reduced spectra, with slit-loss corrections and background subtraction optimized for point sources. We also provide redshifts and signal-to-noise ratio > 5 emission-line flux catalogs for the prism and grating spectra, and concise guidelines on how to use these data products. Alongside spectroscopy, we are also publishing fully calibrated NIRCам imaging, which enables studying the JADES sample with the combined power of imaging and spectroscopy. Together, these data provide the largest statistical sample to date to characterize the properties of galaxy populations in the first billion years after the Big Bang.

Unified Astronomy Thesaurus concepts: [Galaxy evolution \(594\)](#); [Galaxy formation \(595\)](#); [Reionization \(1383\)](#); [Early universe \(435\)](#); [Surveys \(1671\)](#)

1. Introduction

The long-awaited launch of JWST has revolutionized our ability to observe the early Universe. Already in the first 2 yr of operations, JWST enabled an amazing number of discoveries and studies. Many of these breakthroughs have been made possible by the unprecedented sensitivity and wavelength coverage of the NIRSpec instrument (P. Jakobsen 2022). These

²³ These authors contributed equally to this work.



include the spectroscopic confirmation of galaxies beyond redshift $z = 11$ (P. Arrabal Haro et al. 2023; E. Curtis-Lake et al. 2023; B. Wang et al. 2023)—including through emission lines (A. J. Bunker et al. 2023); the discovery of substantial neutral-gas absorption in galaxies at $z = 9–11$ (e.g., K. E. Heintz et al. 2023; H. Umeda et al. 2024); the first studies of metallicity and chemical abundances using well-known optical lines (e.g., M. Curti et al. 2023; K. Nakajima et al. 2023); the discovery of massive, quiescent and old galaxies at $z = 3–5$ (e.g., A. C. Carnall et al. 2023; K. Glazebrook et al. 2024); the first “miniquenched” galaxies (T. J. Looser et al. 2024; V. Strait et al. 2023); neutral-phase outflows in massive quiescent galaxies (S. Belli et al. 2024; R. L. Davies et al. 2024; F. D’Eugenio et al. 2024a); the discovery of bright, metal-poor active galactic nuclei (AGN; e.g., D. D. Kocevski et al. 2023; H. Übler et al. 2023); the most distant AGN (A. D. Goulding et al. 2023; R. Maiolino et al. 2024a); and even tentative evidence of the first generation of stars (R. Maiolino et al. 2024b).

However, for spectroscopy, sample sizes are still small, of the order of tens to 100 objects (T. J. Looser et al. 2023; K. Nakajima et al. 2023; M. Curti et al. 2024). The availability of large samples is key to characterizing the properties of galaxy populations, studying their cosmic evolution, and disentangling the intricate pattern of cause and effect between the observed properties of galaxies. Studies of galaxies at redshifts $z < 1$ rely on thousands or even hundreds of thousands of spectroscopic targets (e.g., K. N. Abazajian et al. 2009; DESI Collaboration et al. 2016; S. P. Driver et al. 2018). By studying several physical properties at a time (e.g., G. Kauffmann et al. 2003a, 2003b; G. J. Graves & S. M. Faber 2010; Y.-j. Peng et al. 2010), or by using machine learning techniques (e.g., A. F. L. Bluck et al. 2022; W. M. Baker et al. 2022; S. Barsanti et al. 2023; M. Walmsley et al. 2023), these studies have made tremendous progress in understanding the links between many galaxy properties like morphology, star formation rate (SFR), age, gas fraction, star formation efficiency, supermassive black hole mass, local and global environment, and metallicity. In the last decades, large spectroscopic surveys in the near-infrared have enabled the study of hundreds of galaxies at redshifts $z = 1–4$ (e.g., M. Kriek et al. 2015; E. Wisnioski et al. 2015; J. P. Stott et al. 2016). In the near future, new surveys will observe even more galaxies at redshifts $z \lesssim 4$ (G. Dalton et al. 2012; N. Tamura et al. 2016; R. S. de Jong et al. 2019; R. Maiolino et al. 2020). However—at least for the next decade—nothing other than JWST and, in particular, NIRSpec will be able to obtain deep rest-frame optical spectroscopy for large samples of galaxies at redshifts of 3–10, the crucial early phases of galaxy formation.

The NIRSpec microshutter assembly (MSA; P. Ferruit et al. 2022) was designed to observe more than 100 targets simultaneously, and is now the highest-multiplicity slit-based spectrograph in the near-infrared. In the NIRSpec/MSA, this high multiplicity marries an unprecedented combination of large collecting area, low background, and long wavelength coverage, which all together enable us, for the first time, to efficiently observe large samples of galaxies at redshifts $z > 4$, covering their strongest rest-frame optical features (e.g., T. Treu et al. 2022, S. Fujimoto et al. 2023, P. A. Oesch et al. 2023a, R. Bezanson et al. 2024; A. J. Bunker et al. 2024, hereafter B24).

One of the goals of the JWST Advanced Deep Extragalactic Survey (JADES; D. J. Eisenstein et al. 2023a), is to observe a statistical sample of galaxies at redshifts $z > 3$, thus enabling spectroscopic studies to move from the “discovery” stage to a more quantitative understanding of galaxy populations. To enable this progress, JADES—a collaboration between the JWST NIRCам and NIRSpec Guaranteed Time Observations (GTO) teams—was designed to fully exploit the synergy between photometry and spectroscopy. The JADES strategy divides the survey time between two tiers: medium-depth and deep observations (for the least deep and widest tier of the NIRSpec GTO, see M. V. Maseda et al. 2024). All observations are in the two Great Observatories Origins Deep Survey (GOODS) fields (M. Giavalisco et al. 2004), but the medium tier is divided between the GOODS South and North fields (hereafter, GOODS-S and GOODS-N), whereas the deep tier is in GOODS-S only. Two previous public releases have published GOODS-S data only, Data Release 1 (DR1), which is split between imaging (M. J. Rieke et al. 2023) and spectroscopy (B24), and Data Release (DR2), which provided new GOODS-S imaging (D. J. Eisenstein et al. 2023b).

In this article, we present medium-depth spectra from both GOODS-S and GOODS-N, as well as new “ultradeep” NIRSpec observations in the Hubble Ultra-Deep Field (HUDF; S. V. W. Beckwith et al. 2006). The latter were obtained in parallel to NIRCам imaging of the JADES Origins Field (also located within GOODS-S, just south of the HUDF; D. J. Eisenstein et al. 2023b). We provide fully reduced and calibrated 1D and 2D spectra, as well as measurements of redshift and emission-line fluxes.²⁴ The NIRSpec data presented here cover all JADES observations up to 2023 October; spectroscopic data collected from 2023 November will be the subject of a future data release. In support of this spectroscopy, we also present previously unpublished NIRCам imaging in GOODS-N, including photometric catalogs and photometric redshifts (photo- z). After presenting the new NIRCам data (Section 2), we move to spectroscopy with a summary of the NIRSpec observations and sample selection (Sections 3 and 4) and of the data reduction (Section 5). We then outline the measurements of spectroscopic redshifts and line fluxes (Sections 6–8). In Sections 9 and 10 we present an assessment of the data products and guidelines for their use, and in Section 11 we showcase exciting highlights from the current data. We conclude with a short summary and brief outlook (Section 12).

Note that the current data release employs the same data reduction as the previous NIRSpec data release (DR1; B24), with the only difference being a different algorithm for the measurement of emission-line fluxes. This is the third JADES data release (hereafter, DR3), but only the second data release for spectroscopy; JADES DR2 included only NIRCам imaging. Throughout this work, we use the AB magnitude system (J. B. Oke & J. E. Gunn 1983).

2. Release of NIRCам Imaging in GOODS-N

GOODS-N is a very important deep field, as it includes the iconic Hubble Deep Field (HDF; R. E. Williams et al. 1996) and the many other programs that followed in and around it. Of particular note are the substantial Hubble Space Telescope

²⁴ Available on the JADES website at <https://jades-survey.github.io/scientists/data.html>.

(HST) optical and near-infrared imaging from GOODS (M. Giavalisco et al. 2004) and CANDELS (N. A. Grogin et al. 2011; A. M. Koekemoer et al. 2011), very deep X-ray imaging from Chandra (D. M. Alexander et al. 2003; Y. Q. Xue et al. 2016), (sub)millimeter observations (E. L. Chapin et al. 2009; J. R. Mullaney et al. 2012; B. Magnelli et al. 2013; L. L. Cowie et al. 2017), and broadband radio coverage (G. E. Morrison et al. 2010; E. J. Murphy et al. 2017). This region also has extensive ground-based spectroscopy (e.g., G. D. Wirth et al. 2004; T. Treu et al. 2005; J. A. Newman et al. 2013; M. Kriek et al. 2015), HST grism spectroscopy (I. G. Momcheva et al. 2016), and hosts other JWST NIRSpec programs such as AURORA (Program ID, PID 1914; A. E. Shapley et al. 2021).

As a part of JADES DR3, we are including images and catalogs from the NIRCcam imaging in GOODS-N, observed as the Medium Prime part of JWST Program 1181 (PI: Eisenstein). These data were observed in 2023 February and include seven overlapping medium-deep pointings, each with 8–9 separate filters. Four of the pointings are mildly deeper than the other three; details are in D. J. Eisenstein et al. (2023a). The imaging data are supplemented with F182M, F210M, and shallow F444W imaging from the FRESCO survey (P. A. Oesch et al. 2023a).

The reduction of these images follows closely the processing used for JADES DR1 (M. J. Rieke et al. 2023) and DR2 (D. J. Eisenstein et al. 2023b). For the photometric catalog release, we follow the methods described in M. J. Rieke et al. (2023), D. J. Eisenstein et al. (2023b), and B. Robertson et al. (2024). These methods were engineered on the deeper JADES GOODS-S imaging. To remove some spurious extended low-surface-brightness (SB) sources, we conservatively remove objects with an average SB < 0.045 nJy pixel⁻¹ within the detection segmentation. Beyond this revision, the techniques follow exactly B. Robertson et al. (2024) and will be described in more detail in B. Robertson et al. (2025, in preparation). As before, the JADES GOODS-N release includes mosaic imaging in all bands, object detection, and photometric catalogs from the JADES reduction pipelines, and photometric redshifts determined using EAZY (G. B. Brammer et al. 2008). An interactive FITSMAP (R. Hausen & B. E. Robertson 2022) website displaying the images, catalogs, and NIRSpec slit overlays and extracted spectra is available via <https://jades-survey.github.io/viewer/>. Figure 1 shows the extent of the JADES NIRCcam imaging in the release, visualized as a red–green–blue false-color image using F444W, F200W, and F090W, respectively. To provide a sense of the depth of the image, which reaches ~ 30 mag in some JADES filters, we show in Figure 2 the JADES NIRCcam F444W/F200W/F090W image of the HDF footprint. This image highlights the advance of JWST in sensitivity and resolution, providing a deep near-infrared view of the iconic HDF.

In total, this JADES release covers 56 arcmin² of NIRCcam imaging in GOODS-N, detecting 85,709 distinct objects. A summary of the area, median depths, and median exposure times in each filter is provided in Table 1. Maps of the local 5 σ point-source, aperture-corrected depths measured in circular apertures of radius $r=0''.15$ are shown for each filter in Figure 3, along with the location of the HDF footprint for reference.

In releasing the JADES NIRSpec spectroscopic and NIRCcam imaging data jointly, we note the unique synergy between these JWST data sets. Beyond the scientific synergies,

the NIRCcam data complement the NIRSpec data by providing targets, enabling consistency checks on the flux calibration of NIRSpec spectral modes, improved slit-loss corrections by providing information on source morphologies, and providing important checks on possible slit contamination by faint sources proximate to the primary NIRSpec targets. The design and execution of the NIRSpec spectroscopic surveys benefit from deep NIRCcam imaging, and cospatial NIRCcam imaging data enhance the science return of complex NIRSpec MSA campaigns.

3. NIRSpec/Microshutter Assembly Observations

All observations used NIRSpec in multiobject spectroscopy mode, with the NIRSpec/MSA (P. Ferruit et al. 2022). The MSA configurations were planned as described in Section 4 using the strategy detailed in D. J. Eisenstein et al. (2023a). For each visit, a set of target acquisition (TA) objects (stars and compact galaxies) were identified on the same images as those used for measuring the positions of the science targets. All TA objects were visually inspected to ensure they were compact, symmetric, and did not have color gradients or nearby sources. All TAs used the NIRSpec clear filter and longest readout time (mode `nrsrapid6`) because the GOODS fields only contain faint TA objects. Further details on the TA setups are provided in D. J. Eisenstein et al. (2023a). All 35 TAs performed for JADES so far have been successful.

There were some technical issues with JADES NIRSpec observations that resulted in visits being skipped or having only partial data collection. The two sources of these issues are guide-star acquisition or reacquisition failures from the fine guidance sensor and “shorts” (electrical short circuits with the NIRSpec MSA; T. D. Rawle et al. 2022). For cases where observations of an MSA configuration were partially successful, our strategy is to return with the same MSA configuration 1 yr later to complete the data acquisition on the same targets. For cases where no data were obtained for an MSA configuration, we have replanned at either the same or at a different orientation.

Table 2 gives a summary of all JADES NIRSpec observations, including the typical integration time (we provide the minimum, mean, and maximum integration time for each spectral configuration). We used everywhere the `nrsirs2` readout mode (improved reference sampling and subtraction, or `irs2`; M. Rauscher et al. 2012; B. J. Rauscher et al. 2017). In the following subsections, we provide an outline of the observations that are the subject of this data release. The DR3 electronic files provide more details such as observation dates and actual integration times per target. We generally describe the observations with a label structured as “depth/selection,” where depth is either “Medium,” “Deep,” or “Ultradeep,” and selection is either “HST” or “JWST,” depending on how the majority of targets was selected; these labels are then “translated” into the `TIER` column in the published tables, and are part of the file names for the published spectra.

3.1. 1210: GOODS-S Deep/HST (+JWST)

Observations from the first deep tier of JADES were already presented and extensively described in B24. We refer the reader to that article for all information concerning the observations in Program 1210.

3.2. 1180: GOODS-S Medium/HST (+JWST)

The intent of this program was to observe galaxies mainly selected from HST imaging, before any JWST NIRCcam images

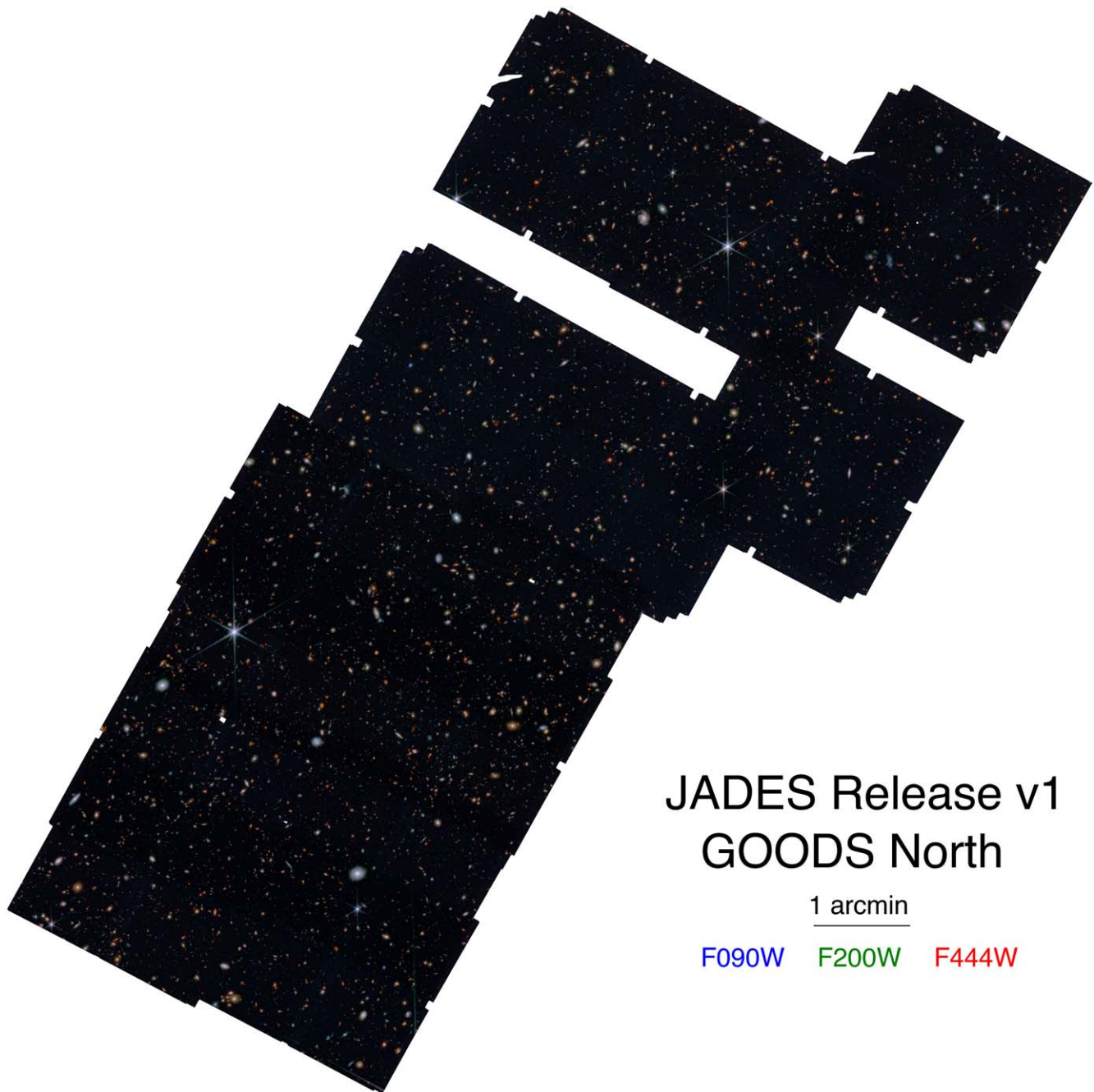


Figure 1. Mosaic of JADES JWST/NIRCam data in the GOODS-N field acquired in 2023 February. The F444W, F200W, and F090W mosaics are shown as the red, green, and blue channels, respectively, in this multicolor image. The scale bar indicates 1'.

were available. Six observations were planned, each consisting of two pointings offset by $\approx 7''$ to dither over the short-wave detector gap in the parallel NIRCam observations. Unfortunately, these observations in 2022 October were heavily impacted by MSA shorts (see also D. J. Eisenstein et al. 2023a for the specific case of shorts in Program 1180). As a result, only four of the 12 target sets were successfully observed in 2022, with three more completed in 2023 October. Even though these failed observations were compensated with replanned observations (as described below), they can still be used to measure redshifts for sufficiently bright galaxies. For this reason, we provide reduced data also for the shorts-affected observations. Examples of shorts-contaminated data are provided in Appendix A; a “data-reduction” flag signals spectra

affected by data-reduction problems; this includes all spectra from shorts-affected observations, including when the data quality was not severely affected (`DR_flag`). The time for the five remaining pointings was replanned as two observations targeted from NIRCam imaging, with target selection criteria closely matching that of GOODS-S Medium/JWST Program 1286. These are referred to as 1180 GOODS-S Medium/JWST.

The seven completed GOODS-S Medium/HST pointings were observed in a single three-point nodding pattern with each of the prism, G140M, G235M, and G395M dispersers yielding total integration times of 3.8, 3.1, 3.1, and 3.1 ks, respectively. The highest priority targets were observed in more than one pointing when possible, so some targets have longer integration times.



Figure 2. Mosaic of JADES JWST/NIRCam data covering the HDF region. Shown are the F444W, F200W, and F090W mosaics as the red–green–blue channels of this multicolor image, respectively. The iconic HDF (R. E. Williams et al. 1996) footprint is shown as a silver line. We note the linear diffuse green feature in the center of the image results from local noise in the F200W image and is not an astrophysical object.

The two replanned observations in 1180 are known as 1180 GOODS-S Medium/JWST. Due to the amount of time available, observation 134 has two subpointings whereas observation 135 has three. Each subpointing has the same dispersers and integration times as in Medium/HST above. The pointings were no longer constrained to be offset by $7''$, and we adopted a strategy to maximize the exposure times of different objects. These observations were executed in 2023 January.

3.3. 1181: GOODS-N Medium/HST

This program consists of four observations planned similarly to the six of GOODS-S Medium/HST, with each observation

comprising two pointings offset by $\approx 7''$. However, for GOODS-N, the total time used with the prism per pointing was increased to a median value of 6.3 ks, using two sets of the three-point nodding pattern. All but one observations were successfully completed in 2023 February. The resulting average is 2.0 hr (Table 2).

3.4. 1181: GOODS-N Medium/JWST

This program was planned using JWST NIRCam imaging for target selection. Four observations were planned, each with three subpointings offset by $\approx 1''$. Three of the observations were completed between 2023 April and May. The fourth was

Table 1
GOODS-N JWST/NIRCam Depths

Band	Area (arcmin ²)	Median Exposure Time (s)	Median Depth ^a (nJy)	Median Depth (AB)
JADES F090W	56.4	11,338	9.8	29.92
JADES F115W	56.4	22,676	6.9	29.30
JADES F150W	56.4	11,338	7.6	29.19
FRESCO F182M ^b	63.0	12,211	11.3	28.77
JADES F200W	56.4	11,338	6.4	29.38
FRESCO F210M ^b	60.6	10,558	14.4	28.50
JADES F277W	55.5	11,338	3.8	29.95
JADES F335M	47.1	8503	6.0	29.45
JADES F356W	55.5	11,338	3.7	29.97
JADES F410M	55.5	8503	7.7	29.19
JADES + FRESCO ^b F444W	83.0	10,393	6.4	29.38

Notes.

^a Median $r = 0''.15$ aperture-corrected 5σ point-source depth.

^b This filter uses data from the FRESCO Program (P. A. Oesch et al. 2023a).

delayed until late May by a guide-star acquisition failure and then partially impacted by MSA shorts. It is scheduled to be completed in 2024 May. Each subpointing uses the prism, G140M, G235M, G395M, and G395H dispersers with total integration times of 3.1 ks each. The MSA configurations are designed to maximize commonality of the targets in each of the three subpointings to yield total integration times of 9.3 ks per disperser.

3.5. 1286: GOODS-S Medium/JWST

Program ID 1286 is the main GOODS-S Medium/JWST program. These observations were planned the same way as those of GOODS-N Medium/JWST above, each with three subpointings separated by $\approx 1''$. Only one of the eight observations was executed during Cycle 1 in 2023 January. The remaining seven were observed in 2023 October and December. Only the visit from 2023 January is included in this data release. For this visit the integration times per subpointing in some dispersers were reduced from 3.1 to 2.7 ks to fit within the available allocation.

3.6. 3215: GOODS-S UltraDeep/JWST

Program ID 3215 is a Cycle 2 GO program that builds on the parallel NIRSpec and NIRCam JADES observations in Program 1210 (D. J. Eisenstein et al. 2023b). The NIRSpec MSA observation consists of five subpointings within $2''$, close to the three subpointings of Deep/HST. For each subpointing the total integration time is 33 ks in each of prism and G395M and 8.3 ks in G140M. Four subpointings were successfully executed in 2023 October. The fifth suffered from a bright MSA short. All of the grating and 25% of the prism exposures in visit 5 were unusable. These are scheduled to be reobserved in 2024 October.

A subset of the observed spectra across all tiers is shown in Figure 4, where the targets are in order of increasing redshift from the bottom to the top row. The varying noise level reflects the combination of exposures of different depth.

4. Sample Selection

As described in our first JADES NIRSpec data release paper (B24), we employ a priority class system to most efficiently use the MSA of NIRSpec (see P. Ferruit et al. 2022). The highest priority classes are reserved for objects that are few in number (i.e., having low sky density), typically targeting very high-redshift candidates. We use these galaxies to optimize each pointing of NIRSpec (see Section 4.5). Lower-priority classes contain many more galaxies, only a fraction of which actually get placed on shutters. With this, we aim to achieve a statistical sample, and JADES aims to span galaxy evolution from Cosmic Noon to within the Epoch of Reionization. As outlined in D. J. Eisenstein et al. (2023a), the JADES spectroscopy has a tiered “wedding cake” survey design, where a smaller number of deep pointings (with long exposure times) are supplemented with medium-depth pointings covering a larger area. As JADES spans a range of science cases, there is not a single selection function for the spectroscopic sample. Instead, each tier has its own prioritization scheme (Tables 3–5). However, each of these schemes is structured in broadly the same way, with the exact criteria changing to reflect the differing input catalogs and differing sensitivity of the observations in each tier.

B24 presented deep spectroscopic observations around the HUDF, including details of the prioritization scheme used for target selection. The data release presented in this paper predominantly introduces the medium tiers of JADES, and the new deep pointing from Program ID 3215.

Some spectroscopic observations were obtained before having JWST/NIRCam imaging. For these, we had to rely on targets selected from existing imaging, predominantly HST, augmented by data from other facilities: we refer to observations planned in this way as Medium/HST (Section 4.2).

Later observations benefited from JWST/NIRCam imaging, and targets were selected from these new data sets where possible. These are called Medium/JWST (Section 4.3). However, we note that in some Medium/JWST observations, the MSA footprint extended beyond the NIRCam coverage. These areas of the MSA had to be filled by HST-based catalogs with selection criteria detailed in column (4) of Table 4, which was designed to mimic the Medium/JWST criteria as best as possible.

We note that Medium/JWST observations were typically deeper than Medium/HST, so although the overall aims of the two tiers are similar, the exact magnitude cuts are different. This is discussed in more detail below.

4.1. Deep/HST

The sample selection for Program 1210 is described in B24.

4.2. Medium/HST

Our observations span the two well-studied fields GOODS-S and GOODS-N, meaning that our HST-based input target catalogs for our initial spectroscopic observations already had a high target density.

GOODS-S. As described in B24, we assembled an HST-based catalog in GOODS-S by compiling $z > 5.7$ candidates from multiple literature sources that had used a combination of Lyman-break dropout criteria and/or photometric redshifts (A. J. Bunker et al. 2004; H. Yan & R. A. Windhorst 2004; P. A. Oesch et al. 2010, 2013; H.-J. Yan et al. 2010;

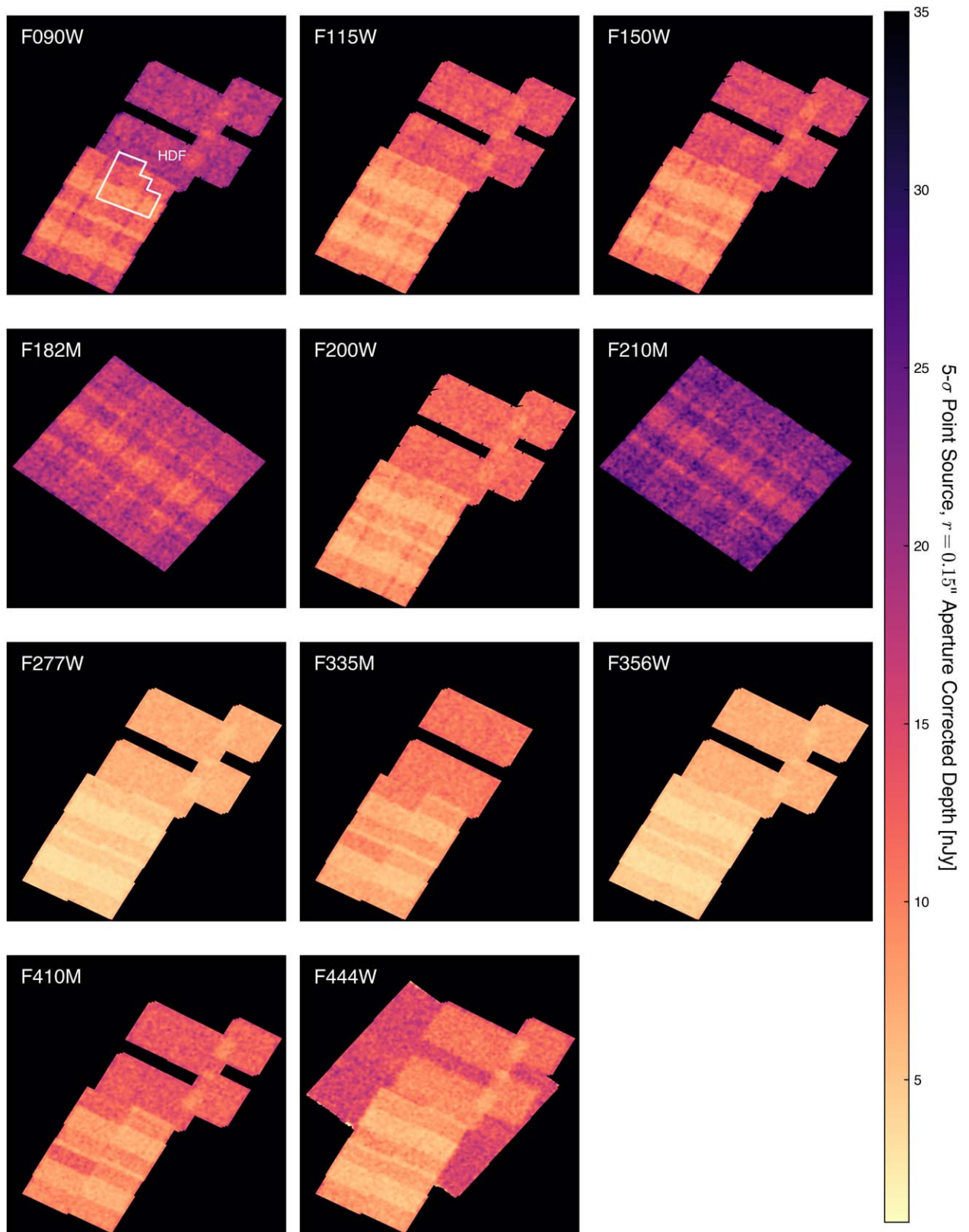


Figure 3. Depth maps of the JWST/NIRCam imaging in the GOODS-N field. Shown are the local, aperture-corrected 5σ point-source depths measured in circular apertures with radii $r = 0''.15$. The F090W, F115W, F150W, F200W, F277W, F335M, F356W, and F410M images use data from the JADES program. The F182M and F210M data were acquired by the FRESCO survey (P. A. Oesch et al. 2023a). The deep F444W data are from the JADES program, and the shallow/wide F444W tier is from FRESCO. The aperture correction is performed using the model point-spread functions from Z. Ji et al. (2024). The color bar indicates the local depth in each filter, as measured in units of nJy. For reference, the outline of the HDF (R. E. Williams et al. 1996) is shown in white on the F090W depth map.

Table 2
Summary of JADES NIRSpec/Microshutter Assembly Observations

PID	Field	Depth	Selection	Tier Name	Prism (hr)	G140M (hr)	G235M (hr)	G395M (hr)	Targets	Release
1210	GOODS-S	Deep	HST/JWST	goods-s-deephst	(7.8/16.5/28.0)	(2.3/4.1/7.0)	(2.3/4.1/7.0)	(2.3/4.1/7.0)	253	B24
1180 ^a	GOODS-S	Medium	HST	goods-s-mediumhst	(0.9/1.0/4.3)	(0.9/1.0/4.3)	(0.9/1.0/4.3)	(0.9/1.0/4.3)	1342	This work
1180	GOODS-S	Medium	JWST	goods-s-mediumjwst1180	(0.3/2.1/5.2)	(0.9/1.8/4.3)	(0.9/1.8/4.3)	(0.9/1.8/4.3)	533	This work
1181	GOODS-N	Medium	HST	goods-n-mediumhst	(0.6/2.0/6.9)	(0.9/1.0/3.5)	(0.9/1.0/3.5)	(0.9/1.0/3.5)	853	This work
1181	GOODS-N	Medium	JWST	goods-n-mediumjwst	(0.3/1.6/5.2)	(0.9/1.7/5.2)	(0.9/1.7/5.2)	(0.9/1.7/5.2)	709	This work
1286	GOODS-S	Medium	JWST	goods-s-mediumjwst	(0.5/2.1/2.2)	(0.7/ 2.1/2.2)	(0.9/2.4/2.6)	(0.9/2.4/2.6)	169	This work
3215	GOODS-S	Ultradeep	JWST	goods-s-ultradeep	(2.8/32.4/61.6)	(2.8/7.7/11.2)	...	(11.2/23.0/33.6)	228	This work
1286 ^b	GOODS-S	Medium	JWST	...						2025
1287	GOODS-S	Deep	JWST	...						2025

Notes. Under each disperser we report the (minimum/mean/maximum) exposure times; the minimum exposure time can be 0 s, due to disobedient shutters (for prism) and for protecting high-priority targets from overlap (for the gratings).

^a Two-thirds of these observations were affected by “shorts.” See Section 3.2 and Appendix A for more details.

^b This data release includes only one of eight observations from PID 1286; the remaining seven observations were obtained in 2023 December and will be part of a future data release.

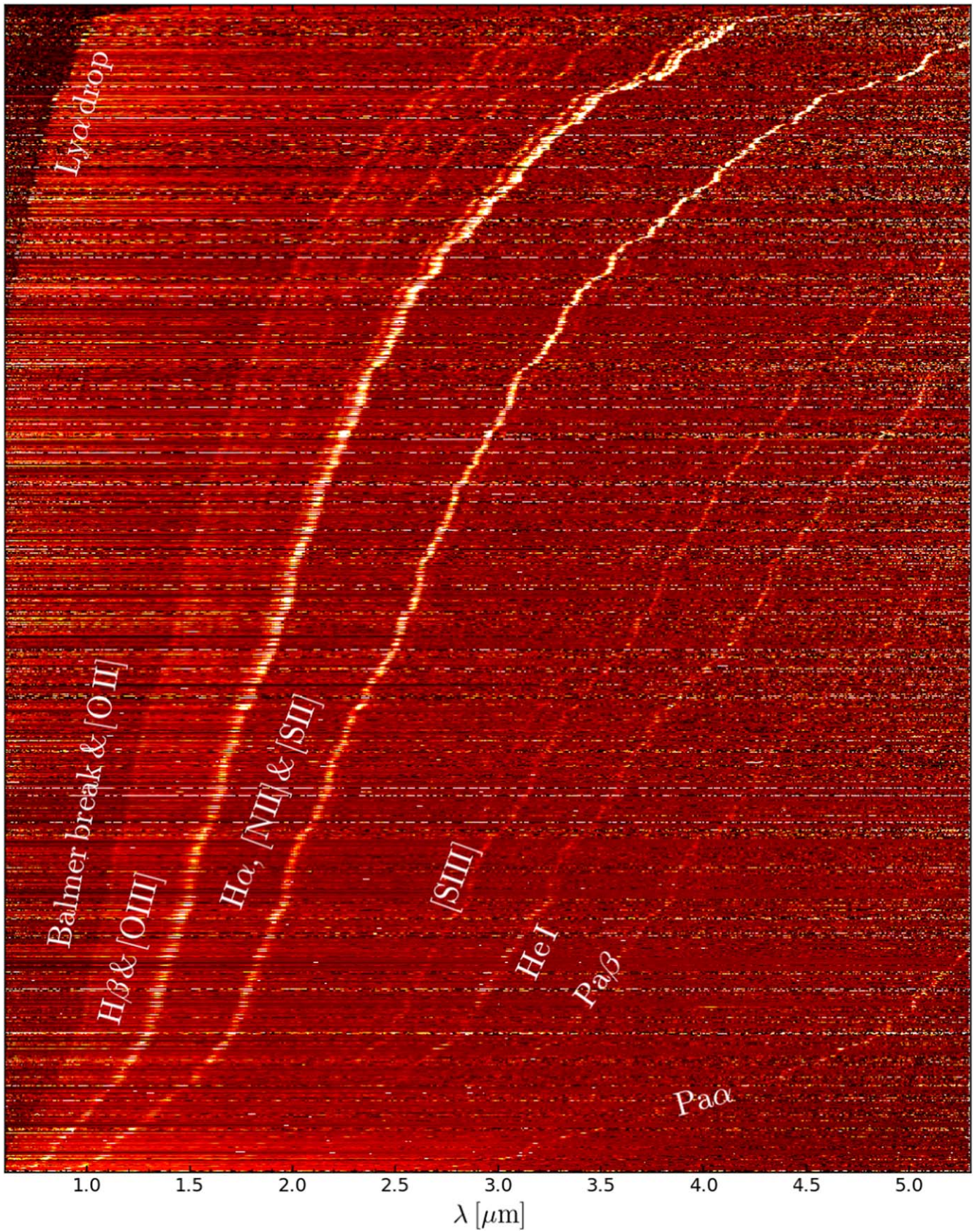


Figure 4. A subset of the observed spectra with multiple emission lines, sorted from bottom to top by increasing redshift. A number of continuum and line features is apparent, illustrating the simultaneous coverage of the rest-frame UV and optical ranges before cosmic noon.

Table 3
Target Prioritization Categories for Medium/HST

Priority	Redshift	Criteria	Targets Observed
1	$z > 5.7$	F160W < 27.5; VI Class ^a 0	68
2.0	$z > 5.7$	F160W < 27.5; VI Class 1	
		27.5 < F160W < 29; VI Classes 0, 1	93
3.0	$1.5 < z < 5.7$	Rare target (e.g., quiescent, AGN, Atacama Large Millimeter/sub-millimeter Array (ALMA)...)	27
3.5	$1.5 < z < 5.7$	F160W < 23.5	43
4.1	$4.5 < z < 5.7$	F160W < 25.5	14
5.1	$4.5 < z < 5.7$	F160W < 27	87
6.1	$4.5 < z < 5.7$	Signal-to-noise ratio (S/N) of H α > 15	44
4.2	$3.5 < z < 4.5$	F160W < 25.5	45
5.2	$3.5 < z < 4.5$	F160W < 27	148
6.2	$3.5 < z < 4.5$	S/N(H α) > 15	63
4.3	$2.5 < z < 3.5$	F160W < 25.5	122
5.3	$2.5 < z < 3.5$	F160W < 27	171
6.3	$2.5 < z < 3.5$	S/N(H α) > 15	59
4.4	$1.5 < z < 2.5$	F160W < 25.5	176
5.4	$1.5 < z < 2.5$	F160W < 27	219
6.4	$1.5 < z < 2.5$	S/N(H α) > 15	54
7	$z > 1.5$	Has Gaia DR2 coordinates and F160W > 23.5	265
7.5	$z < 1.5$	Has Gaia DR2 coordinates 23.5 < F160W < 27	317
7.6	$z < 1.5$	Has Gaia DR2 coordinates F160W > 27	87
8	any z	Anything else with F160W > 23.5	115

Note.

^a Targets were assigned one of the following visual inspection (VI) classes: (0) most compelling, (1) plausible $z > 5.7$, but less compelling, (2) real object but likely $z < 5.7$, and (−1) reject.

S. Lorenzoni et al. 2011, 2013; R. S. Ellis et al. 2013; R. J. McLure et al. 2013; M. A. Schenker et al. 2013; R. J. Bouwens et al. 2015, 2021; S. L. Finkelstein et al. 2015; Y. Harikane et al. 2016). These were supplemented by targets of any redshift from large photometric catalog releases, including R. E. Skelton et al. (2014), K. E. Whitaker et al. (2019), M. Rafelski et al. (2015), Y. Guo et al. (2013), J. A. R. Caldwell et al. (2008), and D. Coe et al. (2006). Critical to assembling our HST-based catalog was ensuring the astrometry of these literature sources was accurate relative to the Gaia DR2 astrometric frame used in TA. The details of how this was achieved, by relating catalogs to the Complete Hubble Archive for Galaxy Evolution re-reduction of the HST imaging (V. Kokorev et al. 2022; G. Brammer 2023),²⁵ are given in Appendix A of B24.

To establish photometry and a redshift for target prioritization, we crossmatched targets across each of these catalogs. HST broadband magnitudes were adopted from the latest available catalog in which the targets appeared in K. E. Whitaker et al. (2019), R. E. Skelton et al. (2014), M. Rafelski et al. (2015), and Y. Guo et al. (2013), or the discovery paper for targets not appearing in any of these catalogs. If the target did not have a reported magnitude, we remeasured the aperture photometry at

the given coordinates. For $z > 5.7$ candidates, we adopt the photometric redshifts of the discovery paper. Other targets are assigned a photometric redshift according to the most recent catalog that reports one. We also crossmatched targets with literature spectroscopic redshift catalogs in GOODS-S (B. Garilli et al. 2008; J. Kurk et al. 2013; D. P. Stark et al. 2013; M. Kriek et al. 2015; A. M. Morris et al. 2015; I. G. Momcheva et al. 2016; H. Inami et al. 2017; E. C. Herenz et al. 2017; L. A. M. Tasca et al. 2017; L. Pentericci et al. 2018a, 2018b; M. V. Maseda et al. 2018). Where we identify matches, these redshifts supersede any photometric redshifts, provided the quality flagging from those catalogs indicated that the redshift was based on either multiple high-S/N emission lines, or a high-S/N detection of an asymmetric Ly α emission profile.

GOODS-N. The GOODS-N HST-based catalog was assembled in largely the same way. Many of the $z > 5.7$ selection papers listed above also extend their samples to GOODS-N (P. A. Oesch et al. 2014; R. J. Bouwens et al. 2015, 2021; S. L. Finkelstein et al. 2015; Y. Harikane et al. 2016). Again, these were supplemented by targets from large HST photometric releases. R. E. Skelton et al. (2014) also cover GOODS-N and their data were included in our catalog, while we also add in targets from the G. Barro et al. (2019) catalog. Astrometry was corrected following exactly the same procedure as in GOODS-S.

Photometry was taken from the most recent catalogs of G. Barro et al. (2019) and R. E. Skelton et al. (2014) if available, otherwise from the discovery paper, or, failing that, from our own remeasured aperture magnitudes. Photometric redshifts were established in the same way as above, and these were again superseded by spectroscopic redshifts if a positional match was identified with a target in a literature catalog, as described above (N. A. Reddy et al. 2006; A. J. Barger et al. 2008; D. P. Stark et al. 2011, 2013; M. Kriek et al. 2015; V. U et al. 2015; I. G. Momcheva et al. 2016; M. V. Maseda et al. 2018).

Additionally, for a small number of our Medium/HST observations in GOODS-N, one of the MSA quadrants partially extended beyond the main GOODS-N CANDELS footprint (see Figure 4 in D. J. Eisenstein et al. 2023a). CANDELS imaging only extended into this area in one band (F814W) of HST/WFC3 imaging (N. A. Grogin et al. 2011). Thus, this MSA real estate could not be populated with targets with robust photometric redshifts in this region. We identified eight objects in this area with X-ray counterparts from the Chandra Deep Field North X-ray survey (Y. Q. Xue et al. 2016), and these were included in Class 3.0 (see Table 3). We then populated the input catalog in this region with targets from more extended imaging, either from Spitzer/IRAC (M. L. N. Ashby et al. 2013) or ground-based imaging from Subaru (P. Capak et al. 2004). The astrometry of these catalogs is less reliable, and thus, all of these targets were placed only in Class 8, although ~60 were observed since there was very little competition for shutter real estate in this part of the MSA, and these formed the vast majority of targets from this class that were observed.

Medium/HST target prioritization. For each of GOODS-S and GOODS-N, these catalogs were then divided into priority classes for Medium/HST observations following the scheme outlined in Table 3. The highest priority targets in Medium/HST comprised high-redshift galaxies with photometric redshifts $z > 5.7$, with the lower-redshift cut corresponding to the “*i*-band dropout” galaxies with the Lyman break in the

²⁵ <https://s3.amazonaws.com/grizli-stsci/Mosaics/index.html>

Table 4
Target Prioritization Categories for Medium/JWST

Priority	Redshift	Criteria (if JWST Based)	Criteria (if HST Based)	Targets
1	$z > 8$	$m_{UV} < 28.0$ (VI Class = 0) ^b		20
2	$z > 8$	$m_{UV} < 28.0$	$z > 8.5, F160W < 28.0$	7
3	$z > 8$	$28.0 < m_{UV} < 28.5$	$z > 8.5, 28.5 < F160W < 28.0$	11
4	$5.7 < z < 8$	$m_{UV} < 26.5$ or $LE^a (F_{line} \geq 10^{-17.3})$		19
5	$z > 2$	$m_{AB} < 22$	$2 < z < 5.7 F160W < 22$	5
6.0 and 6.1	$5.7 < z < 9$	$26.5 < m_{UV} < 28$ or $LE^a 10^{-17.8} < F_{line} < 10^{-17.3}$,	$F160W < 28$	78
6.2	$5.7 < z < 8.5$	$28 < m_{UV} < 28.5$	$F160W > 28$	10
7.1	$4.5 < z < 5.7$	UVJ and F444W < 27; X-ray sources	$F160W < 28$	3
7.2	$3.5 < z < 4.5$	UVJ and F444W < 27; X-ray sources	$F160W < 28$	6
7.3	$2.5 < z < 3.5$	UVJ and F444W < 27; X-ray sources	$F160W < 27.5$	14
7.4	$1.5 < z < 2.5$	UVJ and F444W < 27; X-ray sources	$F160W < 27.5$	19
7.5	$4.5 < z < 5.7$	$F444W < 27$	$F160W < 28$	65
7.6	$3.5 < z < 4.5$	$F444W < 27$	$F160W < 28$	108
7.7	$2.5 < z < 3.5$	$F444W < 27$	$F160W < 27.5$	177
7.8	$1.5 < z < 2.5$	$F444W < 26$	$F160W < 27.5$	155
7.9	$1.5 < z < 2.5$ $z < 5.7$	$26 < F444W < 27$; or $LE^a 10^{-17.9} < F_{line} < 10^{-17.3}$		50
8.0 and 8.1	$z > 1.5$	$F444W < 28$ mag or $S/N(H\alpha) > 20$	$F160W > 28.5$ and has Gaia DR2 coordinates	352
8.2	$z < 1.5$	$F444W < 28$ mag	$24.5 < F160W < 29$ and has Gaia DR2 coordinates	171
8.3	no redshift cut	$F444W < 29$	$F160W > 29$ and has Gaia DR2 coordinates	99
9	...		$F160W > 24.5$	46

Notes.

^a Strong line emitters (LEs; units of $\text{erg cm}^{-2} \text{s}^{-1}$) were selected based on measurements from FRESCO or MUSE, or targets with an F410M excess.

^b VI Class = 0 are the most robust candidates.

HST/Advanced Camera for Surveys (ACS) F775W filter (see A. J. Bunker et al. 2004). These targets were subdivided based on an F160W magnitude cut, prioritizing the brightest sources. Additionally, we performed a VI of the HST imaging, placing the most robust candidates in our highest class. More marginal targets we retained in Class 2, and unconvincing targets were removed.

The next priority classes comprised targets with low surface density, including very bright ($m_{F160W} < 23.5$) $z > 2$ objects (to obtain exceptionally high-S/N spectra of a small subset), and any targets considered likely to be AGN, quiescent, or Lyman-continuum leakers at $1.5 < z < 5.7$.

To include more typical star-forming galaxies over this redshift range, we subdivide our input catalog into four photometric redshift slices ($4.5 \leq z < 5.7$; $3.5 \leq z < 4.5$; $2.5 \leq z < 3.5$; and $1.5 \leq z < 2.5$), with the higher-redshift slices having higher priority given that the surface density of these targets is typically lower.

Each redshift slice is then subdivided into three priority classes, the first two based on the HST F160W magnitude (which is the reddest available band in HST, and the best single-band approximation to a stellar-mass selection). This is then supplemented by an SFR-based selection (using SFRs from the 3D-HST catalog of R. E. Skelton et al. 2014). We converted the SFRs to $H\alpha$ line fluxes, and then to expected S/N for the $H\alpha$ line accounting for typical slit losses of the MSA. Those predicted to have $S/N(H\alpha) > 15$ in the NIRSpec prism were included in this priority class.

Class 7 then comprised any other literature source with coordinates that could be robustly tied to the Gaia DR2 astrometric frame (as described in B24) with a photometric redshift $z > 1.5$, and sources at lower redshift (also with Gaia

DR2) subject to F160W magnitude cuts. Finally, we included anything else that was not at risk of saturating exposures in Class 8.

4.3. Medium/JWST

For Medium/JWST, our primary target list came from the recent NIRCcam images, which extend to longer wavelengths (and in many cases greater depth) than the HST images, and hence revealed more targets with more robust photometric redshifts at high redshift. The target selection criteria are detailed in Table 4.

The JADES team produced photometric catalogs (see, e.g., M. Rieke et al. 2023) and we performed spectral energy distribution (SED) fitting with BEAGLE and EAZY (see, e.g., K. N. Hainline et al. 2024) to determine photometric redshift probability distributions for each target. In addition to the SED-fitting-based photometric redshifts, we also used color cuts to identify Lyman-break candidates at $z \gtrsim 5.7$. We note that the photometric catalog was being frequently updated as imaging depth was added and NIRCcam data reduction was improved. Target selection was always performed with the latest catalog available to us at the time of designing the observations. For this reason, in general, the input catalogs differ from catalogs associated with later public data releases of the imaging.

Throughout this section, where we refer to magnitudes, these are usually the ‘‘CIRC2’’ apertures from the photometric catalogs (radius of $0''.15$), which was selected to approximate the open area of an NIRSpec microshutter. However, for Class ≥ 7.0 where we move to F444W-based selections, we switch to using larger apertures, to better approximate a stellar-mass-based selection. For GOODS-S, we used the Kron apertures, while for GOODS-N we used the ‘‘CIRC4’’ aperture

Table 5
Target Prioritization Categories for 3215 UltraDeep

Priority	Redshift	Criteria	Targets
1.1	$z > 11$	$m_{AB} < 30$	4
1.2	$z > 11$	$m_{AB} < 30$ and less reliable photo- z	0
2.1	$10 < z < 11$	$m_{AB} < 30$	0
2.3	$8 < z < 10$	$m_{AB} < 30$	6
2.4	$8 < z < 10$	$m_{AB} < 30$ and less reliable photo- z	2
3.1		rare objects ^a	5
3.2		rare objects ^b	4
4.1	$7 < z < 8$	$m_{AB} < 30$ from R. Endsley et al. (2024)	
	$5.7 < z < 8$	$m_{AB} < 28.5$ from other photo- z	3
4.2	$5.7 < z < 7$	$m_{AB} < 30$ from R. Endsley et al. (2024)	8
5.1	$4 < z < 5.7$	$m_{AB} < 28$	15
5.2	$4 < z < 5.7$	$m_{AB} < 29$	23
6.1	$5.7 < z < 8$	$28.5 < m_{AB} < 30$	14
6.2	$4 < z < 5.7$	$m_{AB} < 30$	29
7.1	$2.5 < z < 4$	$25 < m_{AB} < 28$	15
7.2	$2.5 < z < 4$	$28 < m_{AB} < 29$	12
7.3	$1.5 < z < 2.5$	$25 < m_{AB} < 28$	14
7.4	$1.5 < z < 2.5$	$28 < m_{AB} < 29$	15
7.5	$z > 1.5$	$29 < m_{AB} < 30$	17
8.1	$z < 1.5$	$25 < m_{AB} < 28$	21
8.2	$z < 1.5$	$28 < m_{AB} < 29$	7
8.3	$z < 1.5$	$29 < m_{AB} < 30$	5
9		Class 9 objects in Deep/HST	9

Notes.

^a Rare objects includes blue UV slopes, AGN $7 < z < 12$, MIRI $z > 7$, X-ray $z > 4$, and medium-band $\log(\text{line flux/erg cm}^{-2} \text{s}^{-1}) > -18.3$.

^b Rare objects includes ALMA, MIRI $z < 7$, AGN $4 < z < 7$, and medium-band $\log(\text{line flux/erg cm}^{-2} \text{s}^{-1}) < -18.3$.

(radius of $0''.30$) because the Kron aperture photometry was not available in GOODS-N at the time of target selection.

We placed galaxies with photometric redshifts higher than eight in the top priorities, with those brighter than $m_{AB} = 28$ mag in the rest-frame UV ranked top, followed by those with $28 < m_{AB} < 28.5$ mag.

Priority Class 4 covers galaxies with $5.7 < z < 8$ with a magnitude cut on the filter which best approximates to the rest-frame UV around 1500 \AA . As with the Deep/HST Class 4 in B24 we set a relatively bright magnitude cut such that we would expect the rest-frame optical emission lines to be well detected to facilitate line ratio diagnostics (with $S/N(H\alpha) > 25$ in the prism). For Medium/JWST, this rest-frame UV cut corresponds to $m_{AB} < 26.5$ mag, following the methodology in Section 2.1 of B24. We supplemented this class with some emission-line-selected objects with fluxes $> 10^{-17.3} \text{ erg cm}^{-2} \text{ s}^{-1}$ drawn from the FRESCO survey (P. A. Oesch et al. 2023a; using a custom data reduction; F. Sun et al. 2023), from MUSE (H. Inami et al. 2017; E. C. Herenz et al. 2017) and galaxies exhibiting flux excesses in the F410M NIRCcam filter consistent with strong line emission.

Following this, the next class was a small number of very bright ($m_{AB} < 22$ mag) $1.5 < z < 5.7$ targets to enable continuum science. We then targeted more galaxies in the range $5.7 < z < 8$ but fainter than Class 4, split into two rest-frame UV magnitude bins ($26.5 < m_{AB} < 28$ mag and $m_{AB} > 28$ mag). We supplemented this class with emission-line-selected objects with fluxes below $10^{-17.3} \text{ erg cm}^{-2} \text{ s}^{-1}$. In the very first epoch of Medium/JWST observations, taken in

2023 January, we had subprioritized these LEs as Class 6.0, slightly ahead of the $26.5 < m_{AB} < 28$ mag magnitude cut (Class 6.1). But in all subsequent epochs, these were folded in together as Class 6.1.

For lower-redshift galaxies ($1.5 < z < 5.7$) we used the same four redshift slices as for Medium/HST. We created a class of upweighted sources with low target density comprising candidate passive galaxies (selected through the UVJ color criterion; R. J. Williams et al. 2009; J. Leja et al. 2019; and with $F444W < 27$ mag), along with X-ray-selected sources (B. Luo et al. 2017), and these were allocated in descending order of redshift slice. We then turned to the remainder of the galaxies in each redshift bin, where we used the reddest NIRCcam wide filter F444W as a proxy for a stellar-mass-selected sample (selecting on $F444W < 27$ mag), placing each redshift slice in turn as before. We note that this differs from our Medium/HST selection (which is F160W based), as we take advantage of the availability of the redder filter to better approximate to a stellar-mass-limited sample.

Any unused MSA real estate was filled with fainter targets as described in Table 4, Classes 8.0–8.3 and 9. The exact criteria defining Class ≥ 8.0 were not fixed across all epochs of the Medium/JWST survey. We note that these lower classes were never constructed with a view toward being able to conduct well-defined sample-based studies, and were rather aimed at potentially capturing a few extra worthwhile spectra with what is otherwise spare MSA real estate. For our first Medium/JWST pointings in GOODS-S, Class 8.0 was made up of leftover targets for which, based on the UV magnitude, we predicted $S/N(H\alpha) > 20$ based on the SFR, and Class 8.1 was remaining candidates with $F444W < 28$ mag. However, it turned out that many of the targets in this Class 8.0 were pushing below the noise threshold such that this did not end up being a very successful selection, and in later iterations we did not keep this delineation. As a result, we advise caution when considering Class ≥ 8.0 objects in the context of sample-based analyses.

4.4. Ultradeep 3215

Our primary input catalogs for the ultradeep NIRSpec MSA observations came from the work of R. Endsley et al. (2024) at $6 \lesssim z < 9$ and K. N. Hainline et al. (2024) at $z > 8$, both based on the JADES NIRCcam imaging. These were supplemented with photometric redshifts fits on all galaxies in NIRCcam JADES catalog (down to a flux limit) using the BEAGLE and EAZY codes. These photometric redshifts were combined using a permissive consensus criterion to avoid missing good high-redshift candidates.

The ultradeep spectroscopy in this tier has long exposure times, and, based on our experience with the Deep/HST NIRSpec observation (B24), redshifts could be obtained for galaxies as faint as $m_{AB} < 30$. Our highest priority was $z > 11$ galaxies with confident photometric redshifts and $m_{AB} < 30$, followed by those with less confident redshift solutions. Because this program had very nearly the same footprint as 1210 (Section 3.6), the highest priority targets of 3215 include three of the four very high-redshift targets already observed in Deep/HST (E. Curtis-Lake et al. 2023, B24). The next class was galaxies at $10 < z < 11$ and $m_{AB} < 30$, followed by $8 < z < 10$ (again split into those with convincing photometric redshifts followed by those which had lower confidence).

The next class comprised galaxies with unusual properties, such as extremely blue rest-frame UV spectral slopes (two targets), evidence for quiescence (two targets), high-redshift AGN (two targets), an object with a large flux excess in the F410M medium-band filter consistent with strong [O III] λ 5007 emission at $z \approx 7$, and FRESCO strong LEs (two targets).

We then considered the standard sample of objects, moving down in the redshift range. Class 4 includes targets in the range $5.7 < z < 8$ from the R. Endsley et al. (2024) catalog, subdividing these into Subclasses 4.1 and 4.2, based on a redshift cut of 7. These objects went down to our $m_{AB} < 30$ mag cut. We supplemented Subclass 4.1 with $5.7 < z < 8$ targets from the full JADES catalog, for which we impose a brighter magnitude cut of $m_{AB} < 28.5$ mag since objects fainter than this had less reliable photometric redshifts.

We then move in redshift to $4 < z < 5.7$ from our JADES photometric catalog, prioritizing $m_{AB} < 28$ mag (Subclass 5.1) and then $28 < m_{AB} < 29$ mag (Subclass 5.2). Then in Class 6, we place leftover objects down to $m_{AB} < 30$ mag in these $5.7 < z < 8$ and $4 < z < 5.7$ slices (as Subclasses 6.1 and 6.2).

We then move to Class 7, which places objects in redshift slices of $2.5 < z < 4$ and $1.5 < z < 2.5$, with each slice subdivided into two classes based on $m_{AB} < 28$ mag and $28 < m_{AB} < 29$ mag. Class 7.5 then places all remaining $z > 1.5$ objects with $m_{AB} < 30$ mag.

Class 8 then places $z < 1.5$ objects divided into three magnitude slices ($m_{AB} < 28$ mag, $28 < m_{AB} < 29$ mag, and $29 < m_{AB} < 30$ mag). Finally, Class 9 contains filler objects from the HST-based catalogs described above.

4.5. Target Assignment with EMPT and Visual Inspection

Target placement was performed using the EMPT software (N. Bonaventura et al. 2023) and proceeded using the same method as described in B24. Pointing centers are driven by the highest priority class in each tier; Class 1 for Medium/HST and Medium/JWST, and Class 1.1 for Ultradeep 3215. For all candidates with $z > 5.7$, we visually inspected the individual images and quality of the photometric fits before running EMPT to ensure they had good redshift fidelity. An inspection of the full input catalog of many tens of thousands of galaxies was not practical, but we did inspect everything that EMPT had allocated shutters to when designing trial MSA configurations. Sources that were badly contaminated by neighboring objects were removed, and EMPT was rerun at the same location to assign new targets in place of those rejected (this was typically fewer than 10 objects per MSA pointing). In allocating shutters, we require the centroid of the object to fall within an ‘‘admittance zone’’ as described in B24. For the low-dispersion prism, we do not allow the spectra of any target to overlap. As with our Deep/HST observations, we keep the same MSA configuration for the grating spectra as for the prism, which means that the higher-dispersion spectra (which are more extended on the array) do overlap, and we use the prism spectra to avoid confusion in line identifications. The grating spectra of a small number of sources (the highest priority sources and very bright objects) are protected against overlap by closing the shutters of lower-priority targets in nearby rows. This means that a small number of objects are observed in the prism alone.

5. NIRSpec/MSA Data Reduction

The data-reduction pipeline for this release is the same as in B24. However, the larger data set enables us to discuss more in detail some of the calibration issues highlighted in DR1.

The pipeline is developed by the ESA NIRSpec Science Operations Team and GTO NIRSpec teams (C. Alves de Oliveira et al. 2018; P. Ferruit et al. 2022). Most of the processing steps are similar to those adopted by the STScI pipeline used to generate the MAST archive products, but the background subtraction, rectification, 1D extraction, and spectra combination steps have been optimized for the targets observed in JADES programs (see details in B24). In particular, we apply a wavelength correction to compensate for the wavelength bias of noncentered compact sources. This bias arises for sources that are smaller than the slit width, when they are spatially offset within the shutter along the dispersion axis. The issue is discussed in P. Ferruit et al. (2022), and we apply the correction they propose (see their Figure 9).

During the quality assessment of NIRSpec observations, we noted that some shutters failed to open when the MSA was configured at each pointing. These unexpected disobedient shutters might corrupt both the estimate of the background emission and the science spectrum during the data processing workflow. The impact of disobedient shutters is evident in the prism/clear observations where the background and target emission are prominent. Therefore, we initially analyzed the presence of these failed shutters by processing the data without background subtraction and identifying those shutters in which the signal is consistent with no emission. We removed such disobedient shutters from the MSA mask and reprocessed the data following the standard procedure. Only 3% of the targets are affected by disobedient shutters, reducing the total exposure time dedicated to the selected galaxy. In most cases, we just removed only one of the three shutters forming the target slitlet, but for a few targets, the number of disobedient shutters for the slitlet was two and even three.

In Figure 5 we illustrate our current flux and wavelength calibration issues using 199773 (panel (c)), a massive quiescent galaxy at redshift $z=2.8$, where we detect several stellar absorption lines in the medium-resolution gratings. In panel (a) we show the prism spectrum (solid black) and the combined G140M and G395M spectra (blue; no G235M observations are present in PID 3215). The yellow line is the grating spectrum rebinned to the prism wavelength grid, the red line shows the grating spectrum after matching the resolution of the prism (using a Gaussian kernel) and then rebinning. In principle, the red and black lines should overlap, but we can see substantial mismatches in both flux level and wavelength; this is illustrated in panel (b), where we show the ratio between the flux densities of the gratings and prism (after rebinning, in yellow, and after smoothing and rebinning, in red). At wavelengths $\lambda < 1.3 \mu\text{m}$ the flux levels agree to within 5%, but at $1.3\text{--}1.5 \mu\text{m}$ the G140M flux increases reaching a ratio of 10%–15%, before going down again from $1.5 \mu\text{m}$. Being part of PID 3215, this object has no G235M data, but the G395M data show instead a higher flux mismatch of 15% on average with respect to the prism, though with tapering both at the blue and red ends of the grating spectrum (see also Figure 16 in Section 11, illustrating another source with continuum detected in the medium gratings).

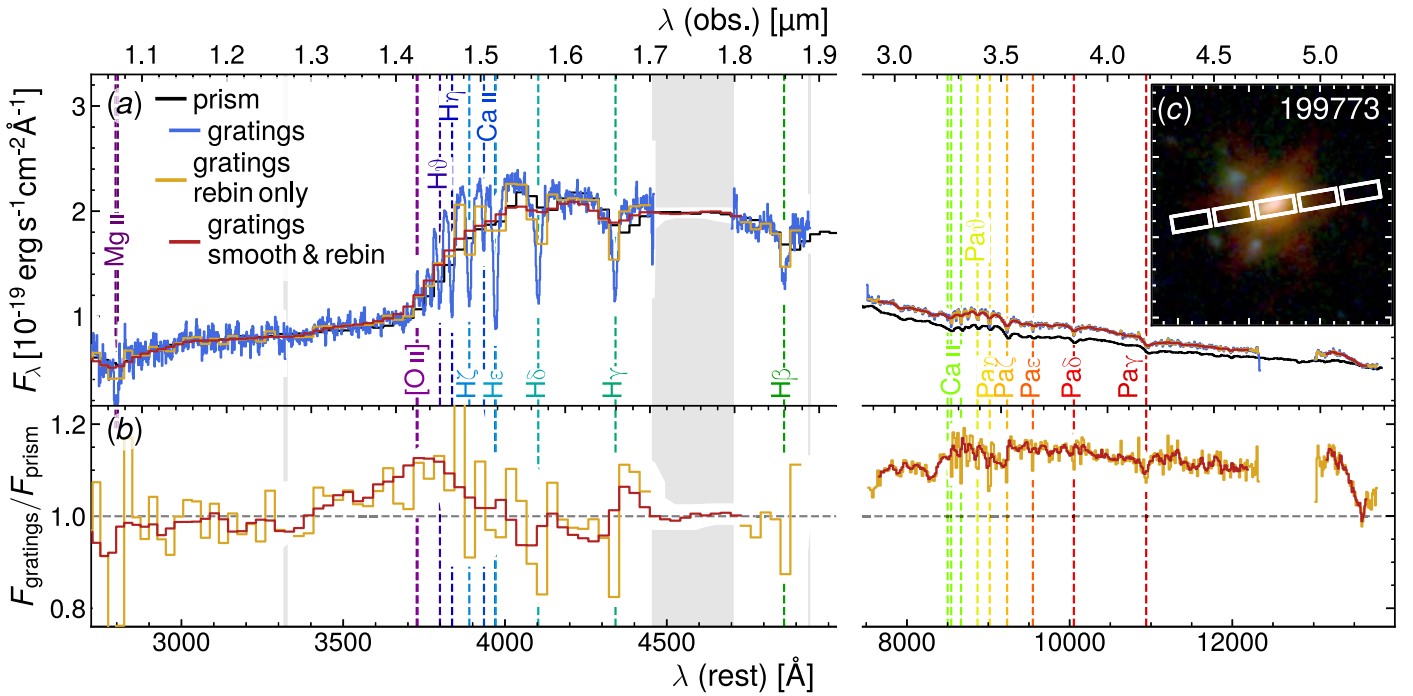


Figure 5. Target ID 199773 from PID 3215, illustrating remaining calibration problems. Panel (a) shows the prism and grating data (in black and blue, with G140M to the left and G395M to the right), and the grating data after rebinning to the prism grid (yellow) and after matching the nominal resolution of the prism and then rebinning (red; vertical gray areas highlight spectral regions where we interpolated over missing grating data, due to bad pixels or the detector gap; the red line is clipped at the edges of the wavelength range due to the size of the convolution kernel). Panel (b) shows the ratio between the rebinned and smoothed-then-rebinned grating spectrum and the prism spectrum (same line colors as in panel (a)). The flux-calibration mismatch between the prism and gratings is wavelength dependent, and is most severe in G395M. The galaxy image is shown in panel (c), with the MSA shutters overlaid. From Z. Ji et al. (2025, in preparation).

At the same time, we confirm that overall the medium gratings require a lower-redshift solution than the prism (Section 9 and B24).

6. Preliminary Redshift Identification

Prior to running the flux measurement software, we measure an initial redshift estimate using a two-step process. In the first step, we run the spectral modeling software BAGPIPES (A. C. Carnall et al. 2019) on the prism data. Our setup is optimized for time-efficient redshift measurement, by using a parametric star formation history which may not fit well the stellar continuum. This step returns both a redshift estimate and a fiducial model spectrum. A detailed description of this procedure is available in B24; an example BAGPIPES model fit is reported in Figure 6 (orange line). Each galaxy is then visually inspected by at least two team members, who use a rudimentary graphics interface to compare the BAGPIPES model to all the available data, including the grating spectra, if available. To assist in the decision, the interface displays a set of strong spectral features (Section 6.1). In this step, the astronomers can change the redshift and assign a quality flag.

6.1. Visual Redshift Determination

The VI is performed using a program which presents the user simultaneously with all the available information in a compact interface. The console is shown in Figure 6, open on target ID 5591 (GN-z11; P. A. Oesch et al. 2016; A. J. Bunker et al. 2023; R. Maiolino et al. 2024a) from Medium/JWST GOODS-N. The top panel shows the 1D prism spectrum, with the BAGPIPES model overlaid, and a set of reference spectral features (vertical dashed lines). Various buttons enable the user

to display the 1D S/N, the 1D uncertainty, additional lines and, crucially, data from other dispersers. The bottom panel shows the 2D S/N map. Finally, the console automatically opens FITSMAP (R. Hausen & B. E. Robertson 2022) centered on the current target; FITSMAP gives the user access to the panchromatic JWST/NIRCam and HST photometry (M. J. Rieke et al. 2023), including the photometric redshifts based on EAZY (G. B. Brammer et al. 2008; K. N. Hainline et al. 2024).

The user is able to change the redshift interactively and judge different solutions. The outcome of this inspection is a user-validated redshift (or no redshift) and a set of flags (Table 6). Users can optionally enter comments; the only mandatory comment is to specify when there is a serendipitous source in the shutter. Typical comments include prominent or peculiar morphologies and doubt about alternative possibilities.

Each galaxy has been inspected by at least two people and by up to four. When the sample is fully inspected, the user sends the resulting catalog of redshifts and flags for merging. The catalogs are compared based on their redshift value. Redshifts that agree to within a tolerance of a spectral pixel are averaged; targets that have different redshifts or redshift flags are reinspected and a final decision is taken. The resulting redshifts are then used as input in various analysis steps, ranging from emission-line measurements (as described in this article), to Bayesian spectral modeling (e.g., BEAGLE or PROSPECTOR).

The distribution of visual redshift flags from this procedure is illustrated in Figure 7.

7. Prism Emission-line Fluxes

We use the spectral fitting software PPF (M. Cappellari 2023) to model the data as a linear combination of spectral

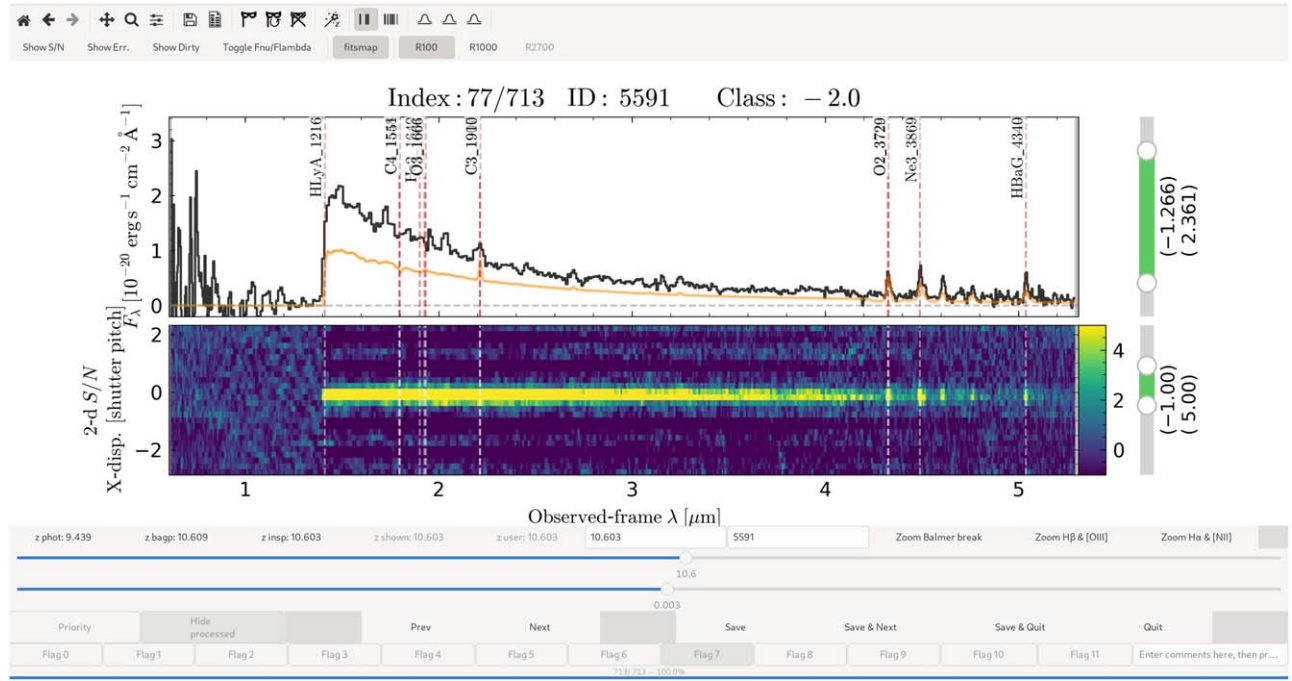


Figure 6. The interface used to visually inspect NIRSpec data, showing GN-z11 (ID 5591 in Medium/JWST GOODS-N; P. A. Oesch et al. 2016; A. J. Bunker et al. 2023; R. Maiolino et al. 2024a). The console displays simultaneously the 1D spectrum and 2D S/N map. The user is able to move a set of bright spectral features to be used as reference (vertical dashed lines). The bottom row of console is the set of flags the user can assign.

templates. As input templates, we use a set of simple stellar population (SSP) spectra from FSPS (C. Conroy et al. 2009). The spectra were calculated using MIST isochrones (J. Choi et al. 2016), the C3K model atmospheres (C. Conroy et al. 2019), and a Salpeter initial mass function (E. E. Salpeter 1955). The spectral resolution is $R = 10,000$ between $0.1 < \lambda < 3 \mu\text{m}$; these templates are available from C. Conroy upon reasonable request. We consider a subset of the templates grid spanning logarithmically ages of 0.03–20 Gyr and metallicities $[Z/H]$ of -2.5 – 0 . We adjust the age grid to each target, ensuring that the oldest available SSP is consistent with the age of the Universe at the redshift of the target (see, e.g., T. J. Looser et al. 2023).

In addition to these stellar templates, we use a set of Gaussian templates to represent nebular emission lines. The gas templates are of three kinds: single Gaussians that represent individual emission lines that are spectrally isolated at any redshift (e.g., He I $\lambda 10830$ [$\lambda 5787$], or Pa β), single Gaussians that represent multiple, spectrally blended lines (e.g., H α + [N II] $\lambda\lambda 6548, 6583$ or H γ + [O III] $\lambda 5007$ [$\lambda 4363$]), and doublet Gaussians representing doublets with fixed ratios (e.g., [O III] $\lambda\lambda 4959, 5007$ or [S III] $\lambda\lambda 9069, 9532$). A summary of emission-line templates and their redshift range is shown in Table 7. Note that the exact set of templates used depends on the source initial redshift—this is because the spectral resolution of the prism is a strong function of wavelength (P. Jakobsen 2022), causing emission-line groups to be spectrally resolved or unresolved at different redshifts. Moreover, we include a step function that is meant to capture very strong Balmer jumps (e.g., A. J. Cameron et al. 2024). All these templates are bound to have nonnegative coefficients in the linear combination. Finally, we use a tenth-order multiplicative Legendre polynomial to adapt the shape of the continuum to the data; this can be thought of as a combination of physical effects (e.g., dust reddening) and flux calibration

Table 6
Flag Values and Meanings Used in the Visual Inspection

Value	Description
0 ^a	Not inspected
1 ^b	Impossible to determine
2	Tentative
3	Peculiar ^c
4	From continuum
5	Single prism line
6	Multiple prism lines
7	Multiple medium-grating lines
8	Multiple high-resolution grating lines
9	Prism data corrupted
10	Medium-resolution data corrupted
11	High-resolution data corrupted

Notes. These can be thought of as bit flags, hence in general a target has multiple flags.

^a Cannot be combined with other flags.

^b Cannot be combined with other flags, except 9, 10, and 11.

^c Usually a serendipitous source in the shutter. User must enter a comment.

(e.g., incorrect slit-loss corrections, for extended objects and for objects with strongly wavelength-dependent morphology). Before running PPXF, each input template is smoothed to twice the spectral resolution of the data, the templates are truncated to match the approximate rest-frame wavelength range of the data, and stellar flux blueward of Ly α is set to zero (we do not include this region in the fit). The templates are additionally convolved with a velocity distribution, modeled as a Gaussian. We run PPXF two times for each galaxy; in the first instance, we “tie” the templates in kinematic subsets, constrained to have the same velocity and velocity dispersion. The kinematic groups are Balmer lines and stellar templates, rest-frame UV lines, rest-frame optical lines, and rest-frame near-infrared lines.

Table 7
List of the Emission Lines Fit in the Prism Spectra

Line(s)	λ (Å)	Tied	z Range	Column Name
C IV $\lambda\lambda 1549, 1551$	1549.48	C4_1549
He II $\lambda 1640 + \text{O III} \lambda\lambda 1661, 1666$	1650.00	Blnd_He2_O3_1650
C III] $\lambda\lambda 1907, 1909$	1907.71	C3_1907
Mg II $\lambda\lambda 2796, 2803$	2799.94	Mg2_2796
[O II] $\lambda\lambda 3726, 3729$	3728.49	O2_3727
[Ne III] $\lambda\lambda 3869, 3968$	3869.86, 3968.59	...	$0 < z < 5.3$	Ne3_3869, Ne3_3968
[Ne III] $\lambda 3869$ [$\lambda 3869$]	3869.86	...	$z \geq 5.3$	Ne3_3869
[Ne III] $\lambda 3869$ [$\lambda 3968$] + He ϵ	3968.59	...	$z \geq 5.3$	Ne3_3968
H δ	4102.86	HD_4102
H γ + [O III] $\lambda 5007$ [$\lambda 4363$]	4341.65	...	$0 < z < 5.3$	Blnd_HG_O3
H γ	4341.65	1	$z \geq 5.3$	HG_4341
[O III] $\lambda 5007$ [$\lambda 4363$]	4363.44	1	$z \geq 5.3$	O3_4363
H β	4862.64	2	$0 < z < 2$	Blnd_HB_O35007d
[O III] $\lambda\lambda 4959, 5007$	4960.30, 5008.24	2	$0 < z < 2$	Blnd_HB_O35007d
H β	4862.64	3	$2 \leq z < 5.3$	HB_4861
[O III] $\lambda\lambda 4959, 5007$	4960.30, 5008.24	3	$2 \leq z < 5.3$	O3_5007d
H β	4862.64	4	$z \geq 5.3$	HB_4861
[O III] $\lambda\lambda 4959, 5007$	4960.30, 5008.24	4	$z \geq 5.3$	O3_4959, O3_5007
He I $\lambda 10830$ [$\lambda 5875$]	5877.25	He1_5875
[O I] $\lambda\lambda 6300, 6363$	6302.05, 6363.67	O1_6300
H α + [N II] $\lambda\lambda 6548, 6583$	6564.52	5	$0 < z < 2$	Blnd_HA_N2_S2
[S II] $\lambda\lambda 6716, 6731$	6725.00	5	$0 < z < 2$	Blnd_HA_N2_S2
H α + [N II] $\lambda\lambda 6548, 6583$	6564.52	6	$z \geq 2$	HA_6563
[S II] $\lambda\lambda 6716, 6731$	6725.00	6	$z \geq 2$	S2_6725
He I $\lambda 10830$ [$\lambda 7065$]	7067.14	He1_7065
[S III] $\lambda\lambda 9069, 9532$	9071.10, 9533.20	S3_9069, S3_9532
Pa δ	10052.12	PaD_10049
He I $\lambda 10830$ [$\lambda 10829$]	10832.06	7	...	He1_10829
Pa γ	10940.98	7	...	PaG_10938
Pa β	12821.43	PaB_12818
Pa α	18755.80	PaA_18751

Note. All wavelengths are in vacuum. The set of templates used to fit any given galaxy depends on its initial redshift guess; this is because the spectral resolution of the prism is a strong function of wavelength (P. Jakobsen 2022), causing emission-line groups to be spectrally resolved or unresolved at different redshifts. Empty redshift ranges indicate the template is used at all redshifts. Rows with the same value in the Tied column indicate emission-line pairs/groups that have tied velocity and velocity dispersion.

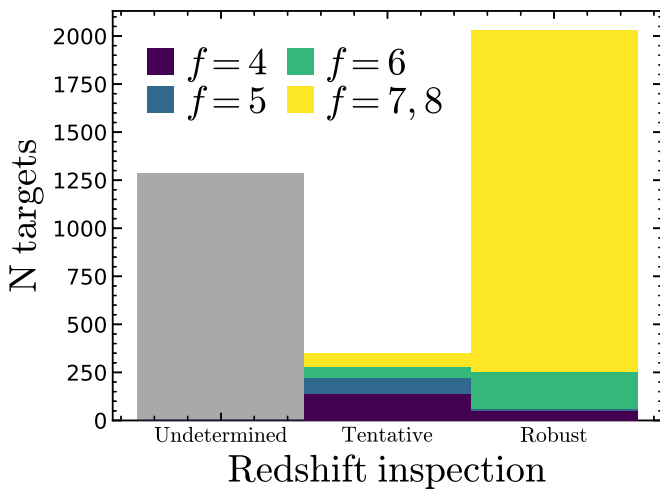


Figure 7. Summary of the VI; the left column shows targets for which a redshift could not be determined (flag 1). Galaxies with uncertain redshifts (center) and with secure redshifts (right) are split by the highest-confidence redshift flag, colored as labeled. Overall, the current success rate of JADES redshifts is 65%.

After this first pass, all lines detected to at least 5σ are kept, whereas the others are discarded. In the second run, we fix the kinematics of the stellar continuum absorption, use only previously detected emission-line templates, and remove almost all kinematic groups. Exceptions to the latter rule are the blend group formed by [S II] $\lambda\lambda 6716, 6731$ and the blend H α + [N II] $\lambda\lambda 6548, 6583$; the group formed by H β and [O III] $\lambda\lambda 4959, 5007$; the group formed by H γ and [O III] $\lambda\lambda 4363$; and the group of He I $\lambda 10830$ [$\lambda 10830$] and Pa γ , whose kinematics are always tied together. We note that He I $\lambda 10830$ [$\lambda 10830$] is resonant, therefore this emission line tends to be redshifted relative to the systemic velocity; however, leaving the line kinematics free relative to Pa γ tended to produce bad fits due to low spectral resolution. Therefore, we opted to keep these lines tied. These conditions track the setup of B24, and are necessary due to the limited spectral resolution of the prism, particularly in the range 1–2 μm . A difference with respect to B24 is that we fix the flux ratio between the emission lines of the [O III] $\lambda\lambda 4959, 5007$ and [S III] $\lambda\lambda 9069, 9532$ doublets. Other doublets with fixed line ratios are not enforced due to being unresolved (e.g., O III] $\lambda\lambda 1661, 1666$) or blended with other lines (e.g., [Ne III] $\lambda\lambda 3869, 3968$).

Table 8
Structure of the Prism Flux Table

Column Name	Description
NIRSpec_ID	ID of the target in EMPT ^b
TIER	Name of subset ^b
PID	Program ID
RA_TARG	Target R.A. [degrees]
Dec_TARG	Target decl. [degrees]
Field	Name of field (GOODS-S or GOODS-N)
NIRCam_ID	ID of matched NIRCam source ^a
RA_NIRCam	NIRCam R.A. [degrees]
Dec_NIRCam	NIRCam decl. [degrees]
x_offset	Intrashutter target offset [arcseconds]
y_offset	Intrashutter target offset [arcseconds]
ObsDate	Date of observations
Priority	Target priority
assigned_Prism	True if has prism observations
assigned_G395H	True if has G395H observations
nDither_Pr	Number of dithers for prism
nDither_Gr	Number of dithers for gratings
nInt_Prism	Number of integrations for prism
nInt_G395H	Number of integrations for G395H
tExp_PRISM	Exposure time for prism [seconds]
tExp_G395H	Exposure time for F290LP/G395H [seconds]
DR_flag	True if problem in reduction or shorts
PRISM_flux_flag	True if at least one line flagged
z_spec	Redshift (both prism and gratings)
z_spec_flag	Redshift flag (both prism and gratings)
z_PRISM	Prism-based redshift
C4_1549_flux	C IV $\lambda\lambda 1549, 1551$ flux
C4_1549_err	C IV $\lambda\lambda 1549, 1551$ flux uncertainty
PaA_18751_flux	Pa α flux
PaA_18751_err	Pa α flux uncertainty

Notes. The full list of emission lines is reported in Table 7; all fluxes are in units of $\times 10^{18}$ erg s⁻¹ cm⁻².

^a NIRSpec_ID are not unique in the table, but the combination of NIRSpec_ID and TIER is unique.

^b NIRCam_IDs are unique, but whether they match the NIRSpec_IDs depends on target selection (HST versus JWST selection), as well as on whether the NIRCam catalog was revised after the NIRSpec observation (which may result in sources being lost to blending and to crossing the non-detection threshold).

After each fit, we postprocess the line fluxes as follows. Below redshift $z < 2$, we combine H β and [O III] $\lambda\lambda 4959, 5007$, and H α + [N II] $\lambda\lambda 6548, 6583$ and [S II] $\lambda\lambda 6716, 6731$; the line uncertainties are added in quadrature. Between $2 \leq z < 5.3$, we combine the flux from the [O III] $\lambda\lambda 4959, 5007$ doublet. Unlike for DR1, the flux of Ly α is never provided, due to the difficulty of modeling the source continuum in the vicinity of this line. We refer the reader to G. C. Jones et al. (2025) for Ly α emitters.

The resulting best-fit spectra were visually inspected for artifacts and bad fits. The most common of these are low equivalent width emission lines near the Balmer break, emission lines due to contaminants, and outliers, especially in shorts-affected observations. The low equivalent width emission lines near the Balmer break arise when the shape of the break is not fit correctly, and the algorithm may use [O III] $\lambda\lambda 4959, 5007$, [Ne III] $\lambda\lambda 3869, 3968$, and H δ to add to the continuum. Contaminants and artifacts may escape the sigma clipping in PPXF when they fall close to strong emission lines in the intended target. All these instances were masked in the data table, and are flagged with a

Table 9
List of the Emission Lines Fit in the Medium-resolution Grating Spectra

Line(s)	λ (Å)	Tied	Column Name
C IV $\lambda\lambda 1549, 1551$	1549.48	1	C4_1549
He II $\lambda 1640$	1640.00	1	He2_1640
O III] $\lambda\lambda 1661, 1666$	1663.00	1	O3_1663
C III] $\lambda\lambda 1907, 1909$	1907.71	...	C3_1907
[O II] $\lambda\lambda 3726, 3729$	3728.49	2	O2_3727
[Ne III] $\lambda 3869$ [$\lambda 3869$]	3869.86	2	Ne3_3869
H δ	4102.86	...	HD_4102
H γ	4341.65	3	HG_4341
[O III] $\lambda 5007$ [$\lambda 4363$]	4363.44	3	O3_4363
H β	4862.64	4	HB_4861
[O III] $\lambda\lambda 4959, 5007$	4960.30, 5008.24	4	O3_5007
He I $\lambda 10830$ [$\lambda 5875$]	5877.25	...	He1_5875
[O I] $\lambda\lambda 6300, 6363$	6302.05	...	O1_6300
H α	6564.52	5	HA_6563
[N II] $\lambda\lambda 6548, 6583$	6585.27, 6549.86	5	N2_6584
[S II] $\lambda\lambda 6716, 6731$	6718.29, 6732.67	5	S2_6718, S2_6732
He I $\lambda 10830$ [$\lambda 7065$]	7067.14	...	He1_7065
[S III] $\lambda\lambda 9069, 9532$	9071.10, 9533.20	...	S3_9069, S3_9532
Pa δ	10052.12	...	PaD_10049
He I $\lambda 10830$ [$\lambda 10829$]	10832.06	...	He1_10829
Pa γ	10940.98	...	PaG_10938
Pa β	12821.43	...	PaB_12818
Pa α	18755.80	...	PaA_18751

Note. All wavelengths are in vacuum. Rows with the same value in the Tied column indicate emission lines that were fitted using the same redshift and FWHM during the same fit because they are sufficiently close in wavelength that the continuum can be modeled simultaneously.

dedicated flag PRISM_flux_flag. A demonstrative set of table column names is reported in Table 8.

We note that the approach used in this data release is different from DR1; B24 mostly used Gaussian model fluxes, with a local-continuum subtraction (except near the lowest prism resolution, where they integrate the continuum-subtracted data). In contrast, the approach used here uses a global continuum model, which includes stellar absorption features.

8. Medium-resolution Gratings Emission-line Fluxes

We fitted the medium-resolution spectra using QubeSpec's²⁶ fitting module. Each emission line was fitted using a single Gaussian component and the continuum was fitted as a power law. This simplistic approach is sufficient for describing a narrow range of the continuum around an emission line of interest (± 100 Å), because usually the continuum is poorly detected. The majority of the emission lines are fitted in isolation except for a group of emission lines that are close to each other. We show the full list of emission lines fitted in this work and the groups fitted together in Table 9.

To estimate the model parameters we use QubeSpec, a Bayesian modeling code implemented with the Markov Chain Monte Carlo (MCMC) integrator emcee (D. Foreman-Mackey et al. 2013). To measure the emission-line fluxes, we need to set prior probabilities for each of the variables. The peaks of the Gaussian profiles and the continuum normalization are given a log-uniform prior, while the FWHMs are set to a uniform distribution spanning from the minimum spectral resolution of the

²⁶ <https://github.com/honzascholtz/Qubespec>

Table 10
Structure of the Gratings Flux Table

Column Name	Description
NIRSpec_ID	ID of the target in EMPT ^a
TIER	Name of subset ^a
tExp_G395H	Exposure time for F290LP/G395H [s]
z_spec	Redshift (both prism and gratings)
z_spec_flag	Redshift flag (both prism and gratings)
z_PRISM	Prism-based redshift
C4_1549_flux	C IV $\lambda\lambda$ 1549, 1551 flux
C4_1549_err	C IV $\lambda\lambda$ 1549, 1551 flux uncertainty
PaA_18751_flux	Pa α flux
PaA_18751_err	Pa α flux uncertainty

Note. The initial rows are the same as for the prism (between NIRSpec_ID and z_PRISM; see Table 8); all fluxes are in units of 10^{18} erg s⁻¹ cm⁻².

^a NIRSpec_IDs are not unique in the table, but the combination of NIRSpec_ID and TIER is unique.

NIRSpec/MSA (~ 200 km s⁻¹) up to a maximum of 800 km s⁻¹. The prior on the redshift was a truncated normal distribution centered on the redshift from the VI and with a standard deviation of 300 km s⁻¹ and with a maximum allowed deviation of 1000 km s⁻¹.

For emission lines that lie in the overlap of the gratings, we fit both sets of the data and report the properties of the fit with the highest S/N. We do not attempt to stack these spectral overlaps due to different line-spread function and potential flux-calibration offsets between the gratings. This will be further investigated in a future data release.

We fit only a single Gaussian per emission line in the medium-resolution grating. We note that there are some objects with detected outflows or broad-line regions. These fits will be further investigate in I. Juodžbalis et al. (2025, in preparation) and S. Carniani et al. (2025, in preparation).

After the initial fitting run, we visually inspect every model for any incorrect fits or spurious line detection that are caused by unflagged outliers. These flagged fits are then refitted and reinspected. The fluxes are calculated using the MCMC chains (after discarding the burn-in chains) and the final reported values and their uncertainties are the median value and standard deviation from the chains. We only report detections at S/N > 5; for nondetections we report the 1σ uncertainties for the user to define their own upper limits. The final redshift from the medium-resolution spectra is the redshift inferred from the emission line with the highest S/N. This implies that there are galaxies where strong outflows can skew the redshift, but these cases require a tailored analysis beyond the scope of this data release.

The structure of the gratings emission-line catalog is presented in Table 10 in units of 10^{-18} erg s⁻¹ cm⁻². The names of the individual emission lines column are the same as reported in Table 9. For the emission-line doublets with fixed line ratios (such as [N II] $\lambda\lambda$ 6548, 6583 and [O III] $\lambda\lambda$ 4959, 5007) we only report the flux of the stronger emission line. Alongside the fluxes and their uncertainties, the initial rows are the same as for the prism table.

9. Quality Assessment

9.1. Redshift Combination and Comparison: Prism versus Medium Gratings

In Figure 8 we compare the redshift measurements from the prism and from the medium gratings, where both are available.

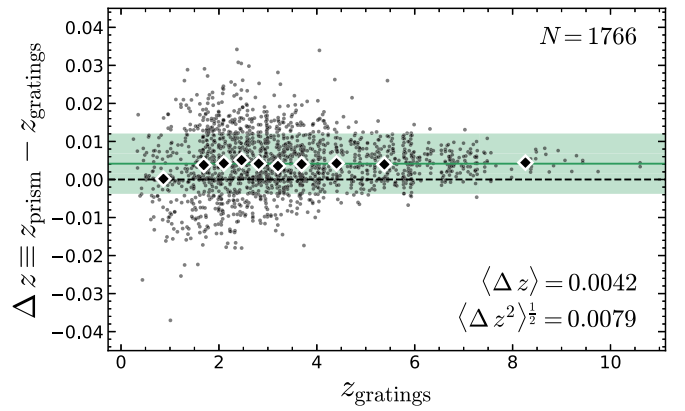


Figure 8. Comparison of redshifts between the prism and the medium-resolution gratings. We find a redshift-independent offset $\Delta z = 0.0042$ (blue line), consistent with B24; the shaded region is the standard deviation. The increased dispersion at low redshifts is expected from the strong dependence of the prism spectral resolution with wavelength. The black diamonds are the moving median; there is some evidence for a reduced bias around $z < 1$.

Having defined $\Delta z \equiv z_{\text{prism}} - z_{\text{gratings}}$, we find a mean of 0.0042 ± 0.0002 and a standard deviation of 0.079, consistent with the findings of B24. This statistically significant offset points to a residual wavelength calibration problem in the prism or medium gratings. We find the offset to be redshift independent; a line fit with the robust least trimmed squares algorithm (using the Python implementation `ltsfit`;²⁷ P. J. Rousseeuw & K. Driessen 2006; M. Cappellari et al. 2013) is consistent with a flat slope of 0.0002 ± 0.0001 . The increased scatter at low redshift is a consequence of the rapid increase of the prism spectral resolution with wavelength; multiplying Δz by $R/(1+z)$ the scatter becomes approximately uniform with z (where R is the prism spectral resolution of the [O III] λ 5007 line at redshift z of each source).

Whenever we have a strong line detection (5σ) in the medium gratings, we adopt the redshift of this line as the object redshift (flag A). Using a single emission line is warranted because medium-resolution fits are made only for galaxies with a VI flag of 7 (Section 6). We checked that there are no cases where the grating and prism spectra disagree by more than $\Delta z = 0.05$, so we can rule out any misidentified lines. Large offsets ($|\Delta z - \langle \Delta z \rangle| > 0.015$, Figure 8) were visually inspected, and are mostly due to uncertainties in the H β + [O III] $\lambda\lambda$ 4959, 5007 blend and to low-S/N data. If no lines have been detected in the medium gratings, we use the prism redshift, requiring at least two emission lines for a secure redshift (flag B), or the combination of a line and/or a strong continuum break (for a less secure or less precise redshift, flag C). An even lower class is reserved for redshifts identified as tentative in the VI; in this case, we report the VI redshift (flag D). All other redshifts are assigned -1 (flag E). To summarize, the final redshift flags are

- (A) redshift from at least one emission line in the medium-resolution grating;
- (B) redshift from two or more prism emission lines;
- (C) redshift from the continuum, or from the continuum and a single prism emission line;
- (D) tentative, from VI; and
- (E) no redshift.

Note that the first three flags are the same as in B24.

²⁷ <https://pypi.org/project/ltsfit/>

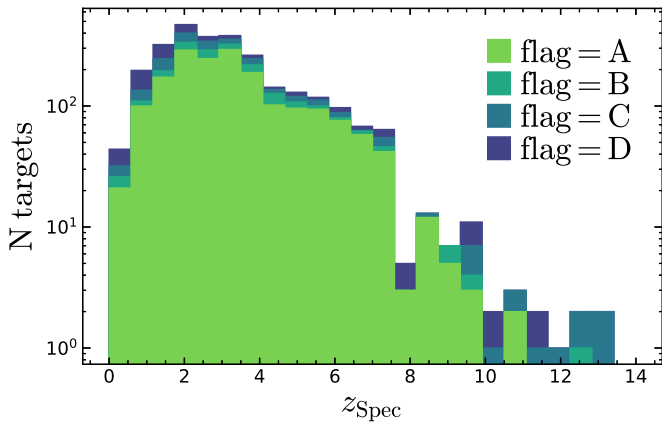


Figure 9. Redshift distribution of the sample, color coded by the final redshift flag (Section 9). We note a drop in redshift distribution at $z_{\text{Spec}} \sim 7.5$; this reflects a similar drop in the distribution of photometric redshifts of the targets selected for observation.

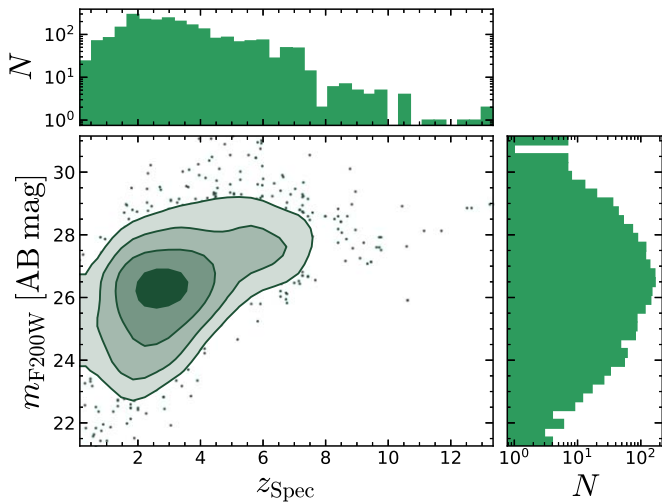


Figure 10. Redshift vs. magnitude distribution of the sample; NIRSpec deep spectroscopy can measure redshifts for targets fainter than 30 mag.

The combined redshift distribution of the sample is shown in Figure 9, color coded by flag. There is a drop in the distribution at $z_{\text{Spec}} \sim 7.5$, which reflects at least in part a similar dearth of targets in the distribution of photometric redshifts of the targets selected for observation. The overall distribution of the spectroscopic sample versus magnitude is displayed in Figure 10 (we show only targets with flags A–C, and with a secure match in NIRCам). The effect of the cosmic evolution of the luminosity function is clearly visible from the shape of the 2D distribution in magnitude–redshift space. In addition, there is a lack of galaxies fainter than 29 mag at redshifts lower than $z_{\text{Spec}} \lesssim 2$ and higher than $z_{\text{Spec}} \gtrsim 9$; this is caused by both sample selection and sensitivity as follows. At low redshifts, NIRCам photometry becomes less able to clearly distinguish line excesses, because the spacing of strong emission lines reduces as $1 + z$; the lower sensitivity of NIRSpec at wavelengths $\lambda < 1 \mu\text{m}$ compounds the problem. At redshifts higher than $z_{\text{Spec}} \approx 9.5$, instead, the strongest emission lines ([O III] $\lambda\lambda 4959, 5007$) are redshifted out of the NIRSpec coverage, so redshifts measurements rest solely on the Ly α break and on less prominent lines—both of which are harder to detect in faint targets.

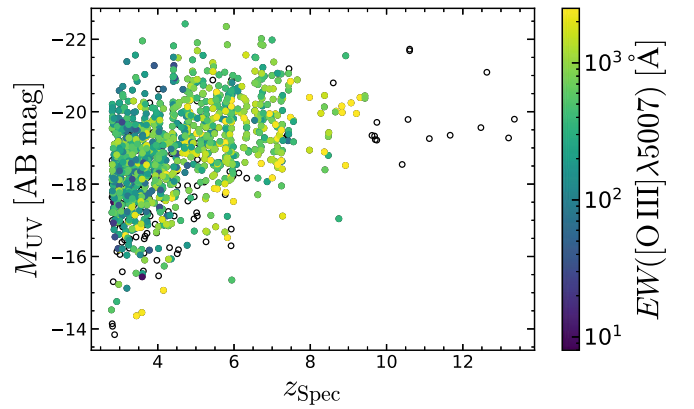


Figure 11. Redshift vs. UV magnitude distribution of the sample, color coded by the equivalent width of [O III] $\lambda 5007$ (empty symbols are galaxies with no detected [O III] $\lambda 5007$). Magnitudes were calculated directly from the prism spectra, using aperture corrections estimated by comparing the prism magnitude to the 0.35 radius magnitude (CIRC5 in the catalogs) in the NIRCам filter nearest to rest-frame 1500 Å. [O III] $\lambda 5007$ falls outside of the NIRSpec wavelength range at $z \gtrsim 9.5$.

In Figure 11 we show M_{UV} versus redshift, for the sample where magnitudes could be measured directly from the NIRSpec data; to this end, we used a nominal top-hat filter between rest-frame 1400 and 1600 Å. The resulting magnitudes were corrected for aperture effects upscaling by the ratio between the observed and synthetic magnitude in the NIRCам band nearest in wavelength (to capture the magnitude of extended objects, we used circular apertures with a 0.35 radius, CIRC5 in the catalogs). The color coding is the equivalent width of [O III] $\lambda 5007$, measured directly on the prism data (empty symbols are galaxies with no detected [O III] $\lambda 5007$). There are clear trends of equivalent width with both M_{UV} at fixed redshift and with redshift at fixed M_{UV} ; the first trend arises from the sublinear slope of the star-forming main sequence, where galaxies have a lower specific SFR with increasing stellar mass. The second trend follows the decreasing normalization of the star-forming sequence with increasing cosmic time (K. Boyett et al. 2024).

9.2. Flux Comparison: Prism versus Medium Gratings

In Figure 12 we compare the flux measurements from the medium gratings to the corresponding measurements from the prism; the top, middle, and bottom rows show, respectively, [O II] $\lambda\lambda 3726, 3729$, [O III] $\lambda\lambda 4959, 5007$ and H α + [N II] $\lambda\lambda 6548, 6583$. For [O III] $\lambda\lambda 4959, 5007$, we consider only galaxies at $z > 2$, where in the prism catalog the doublet is clearly separated from H β ; for H α + [N II] $\lambda\lambda 6548, 6583$, we take the grating measurements of H α and [N II] $\lambda 6584$ and add them, upscaling [N II] $\lambda 6584$ by 1.34 to take into account [N II] $\lambda 6584$ [6548]. For each set of emission lines, we consider the ratio $f_{\text{rat}} \equiv F_{\text{gratings}}/F_{\text{prism}}$, and study this value as a function of F_{prism} (left column) and redshift; due to the requirement to have both prism and medium-grating measurements, redshift is always z_{gratings} .

For [O II] $\lambda\lambda 3726, 3729$, we find that the grating fluxes are 17% higher than the prism values, with large scatter (25%), and have no trend with line flux (panel (a)), but a weak yet statistically significant decreasing trend with redshift ($p < 0.0005$; panel (d)). We interpret this discrepancy as due to how the continuum is modeled by the prism; in particular, the the continuum near the Balmer limit can display a break

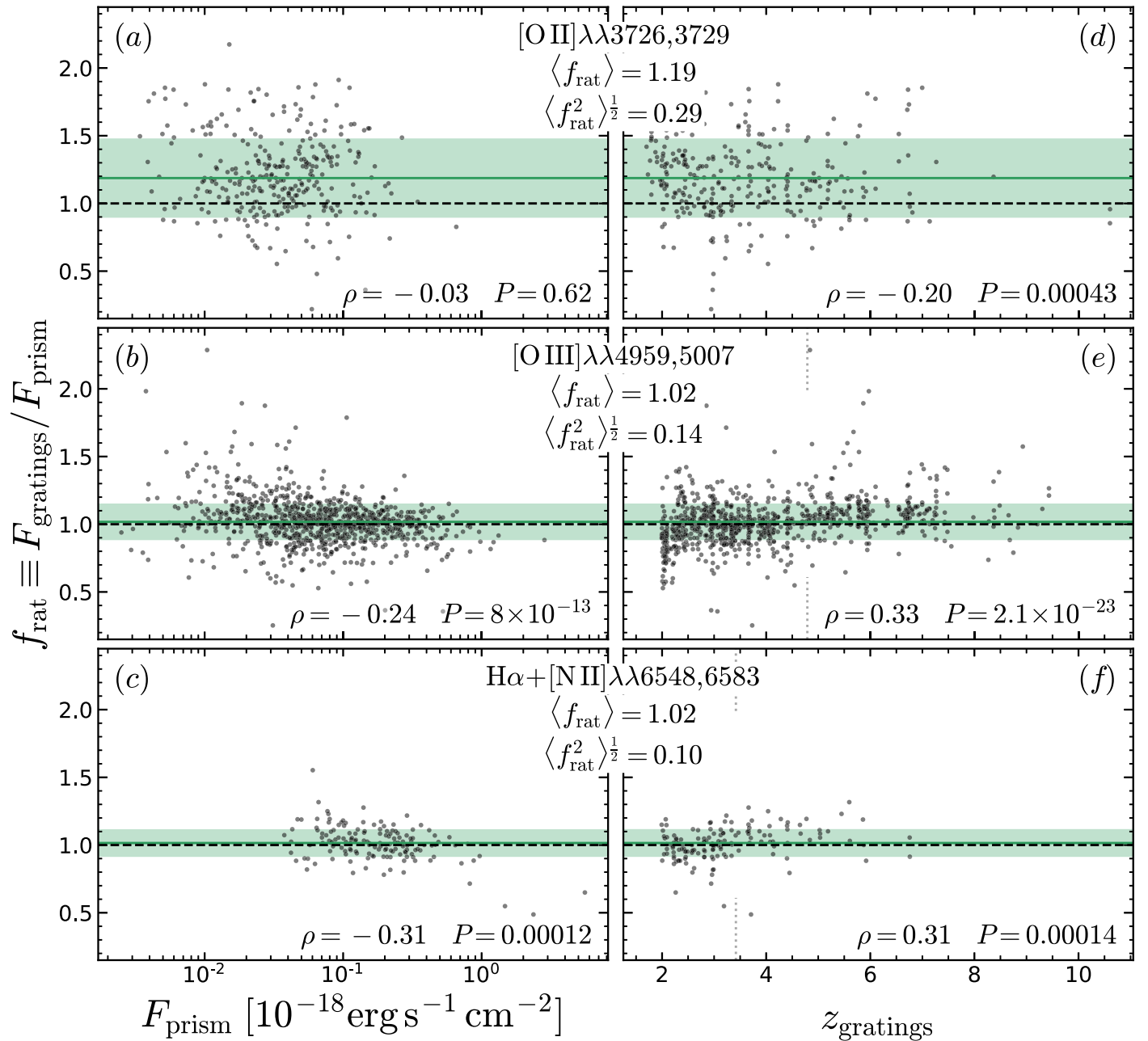


Figure 12. Comparison of the emission-line fluxes measured from the prism and from the medium-resolution gratings, as a function of prism flux (left column) and redshift (right column). The central insets between the columns are the median and standard deviation for each emission-line complex (also displayed as green horizontal lines and shaded regions), while the bottom right corner of each panel reports the Spearman rank correlation coefficient and associated p -value. [O II] $\lambda\lambda 3726, 3729$ (panels (a) and (d)) shows the regime where the gratings-to-prism flux ratio f_{rat} is dominated by systematics in the continuum model; [O III] $\lambda\lambda 4959, 5007$ (panels (b) and (e)) illustrates with high significance the strong correlation between f_{rat} and redshift, which indicates the flux-calibration mismatch between the prism and gratings is most severe in G395M. The dotted vertical lines in panels (e) and (f) show the redshift where [O III] $\lambda 5007$ and $\text{H}\alpha$ are observed at $2.9 \mu\text{m}$ —the bluest wavelength captured by the G395M/F290LP disperser–filter combination. Finally, $\text{H}\alpha + [\text{N II}] \lambda\lambda 6548, 6583$ shows that the total fluxes measured by the prism (where we do not separate $\text{H}\alpha$ from [N II] $\lambda\lambda 6548, 6583$) match the fluxes measured by the gratings well (where the emission-line complex is well resolved); the trends with flux and redshift are consistent with what we see for [O III] $\lambda\lambda 4959, 5007$.

(stellar Balmer break; e.g., T. J. Looser et al. 2024; or nebular Balmer jump; e.g., A. J. Cameron et al. 2024). When the resolution is insufficient, the strength of the break is degenerate with the flux of the nearest lines, with [O II] $\lambda\lambda 3726, 3729$ being the most affected line. This is aggravated by using an incorrect value of the spectral resolution due to slit underfill. All these issues can significantly affect the recovered [O II] $\lambda\lambda 3726, 3729$ flux, particularly in the low-resolution regimes

found at low redshift, which could possibly explain the weak observed trend with redshift in panel (d).

For [O III] $\lambda\lambda 4959, 5007$, we find good agreement (median ratio of 1.01) but a large scatter (albeit smaller than for [O II] $\lambda\lambda 3726, 3729$, of 14%). We believe the better agreement is due to the fact that the galaxy continuum around 5000 \AA is relatively featureless, compared to the region of [O II] $\lambda\lambda 3726, 3729$. We find a decreasing trend with F_{prism} (panel (b)) and an

increasing trend with z_{grating} (panel (d)). A partial-correlation analysis confirms that the redshift correlation is the main one, and that the flux correlation arises from the anticorrelation between flux and redshift. The fact that the ratio increases with redshift is in agreement with the findings of Figure 5, where it seems that the flux discrepancy between the prism and medium-resolution gratings is smallest in G140M and highest in G395M.

Finally, panels (c) and (f) show $H\alpha + [N\text{ II}] \lambda\lambda 6548, 6583$; the results here are consistent with what found for $[O\text{ III}] \lambda\lambda 4959, 5007$. The significant correlation between f_{rat} and flux is driven by the outliers at $F_{\text{prism}} > 60 \times 10^{18} \text{ erg s}^{-1} \text{ cm}^{-2}$; removing these points also removes the correlation.

Figure 12 shows jumps in f_{rat} at certain values of z_{grating} ; for example, in Figure 12(e) these jumps happen at $z_{\text{grating}} \approx 2.5$ and 4.7, which correspond to when the observed wavelength of $[O\text{ III}] \lambda\lambda 4959, 5007$ moves respectively from G140M into G235M, and from G235M into G395M. To estimate the average flux-calibration offset in our data, we divide the sample in three redshift bins, determined by when $[O\text{ III}] \lambda\lambda 4959, 5007$ (our brightest line on average) is observed with G140M, G235M, or G395M (respectively, $0 < z_{\text{grating}} < 2.5$, $2.5 < z_{\text{grating}} < 4.7$, and $z_{\text{grating}} > 4.7$). In these bins, we find average values of f_{rat} of 0.90 ± 0.03 , 1.00 ± 0.01 , and 1.10 ± 0.02 . However, the scatter is large, and galaxies with a clearly detected continuum (e.g., Figures 5 and 16) show that the flux-calibration mismatch is wavelength dependent. We did not find statistical evidence for a dependence of f_{rat} on the target location on the MSA.

To further investigate this discrepancy between the medium gratings and prism we compared the fluxes of emission lines that are observed in two different gratings. This occurs for lines in the region of the spectrum probed by two configurations simultaneously; i.e., $1.6 \lesssim \lambda \lesssim 1.8 \mu\text{m}$ for G140M/F070LP and G235M/F170LP, and $2.9 \lesssim \lambda \lesssim 3.1 \mu\text{m}$ for G235M/F170LP and G395M/F290LP. We find that the average flux ratios are $f_{G140MG235M} = 1.07 \pm 0.01$ and $f_{G395MG235M} = 1.01 \pm 0.01$. These results seem to contradict the findings from comparing the emission-line fluxes from the gratings to the prism (where G140M is lower than the prism, G235M is consistent, and G395M is higher than the prism; Figure 12). However, this analysis focuses on a specific region of the wavelength range, where two gratings overlap, whereas the emission-line comparison spans the entire wavelength range of NIRSpec. As shown in Figure 5, the flux-calibration bias between the prism and G395M seems to be wavelength dependent.

9.3. Accuracy of the Wavelength Calibration

To assess the accuracy of the wavelength calibration, we use the metric Δv ; for each target, $\Delta v \equiv v(1 < \lambda < 2 \mu\text{m}) - v(\lambda > 3 \mu\text{m})$, where $v(1 < \lambda < 2 \mu\text{m})$ is the mean velocity of emission lines with observed wavelengths between 1 and 2 μm , and $v(\lambda > 3 \mu\text{m})$ is the mean velocity of emission lines with observed wavelengths between 3 μm and the maximum wavelength. For this test, we consider only galaxies with more than three independent emission lines having $S/N > 7$. In Figure 13 we show Δv as a function of the intrashutter source positions, δx (closely aligned along the dispersion direction) and δy ; the gray dots are individual galaxies, the green line with bands is a robust least-squares fit (M. Cappellari et al. 2013). For an unbiased solution, both the zero-point and slope of the

best-fit line should be zero. In contrast, we find an average zero-point offset of 300 km s^{-1} (for the prism) and 30 km s^{-1} (for the gratings); these values correspond to 0.1–1 pixels (prism) to 0.1–0.3 pixels (medium gratings). These offsets indicate an overall bias of the wavelength solution. In addition to this zero-point offset, there is also a clear negative correlation between Δv and δx for both prism and gratings. The correlation for the prism is both stronger and more statistically significant, reaching an excursion of 0.5–3 pixels. Before interpreting these correlations, we remark that the coordinates of the MSA are opposite to the pixel coordinates of the detector on the focal plane assembly (see P. Ferruit et al. 2022, their Figure 4; P. Jakobsen 2022, their Figure 4); this means that positive δx values are offset toward bluer wavelength values. With this in mind, the anticorrelation we find means that the correction to the wavelength solution due to intrashutter offsets of compact sources (Section 5 and P. Ferruit et al. 2022) is insufficient. A solution to these remaining calibration issues is beyond the time constraints of this data release, and will be presented in a future work. In Appendix C we further show that on average the wavelength bias of the prism depends on the global position of the source in the MSA.

10. Using the NIRSpec Data Products

In this section, we provide a concise summary on how to use the data products, and a list of the limitations of the current data release. The prospective user of the data provided in this release is encouraged to consider these limitations carefully.

1. *Data-reduction problems and short circuits.* Spectra with data-reduction problems are flagged with `DR_flag=True`; if a redshift was given, it is guaranteed to be accurate from VI. However, for any purpose other than redshift, these data should be visually inspected to assess whether they are suitable. Under this flag we also collect observations affected by MSA short circuits, which may present an abnormally bright background, including steep background gradients across the detector. In all cases, this results in lower-S/N spectra than one would expect given the source magnitudes and integration time. In the most severe cases, shorts cause incorrect background subtraction and no useful observations (Section 3, Appendix A).
2. *Aperture correction.* Aperture corrections assume the target has point-source geometry; for extended sources, this implies both the total flux and the color of the spectrum are inaccurate. For calculating emission-line ratios over long wavelength separations (e.g., $H\alpha/H\beta$, $[O\text{ III}] \lambda 5007/[O\text{ II}] \lambda\lambda 3726, 3729$, or $\text{Pa}\alpha/H\alpha$), we recommend using aperture corrections derived from the photometry. Sources more extended than one shutter should be considered with particular care, or even excluded (see background subtraction below).
3. *Background subtraction.* The background-subtraction strategy is optimized for compact sources; while shutters affected by contaminants are preidentified and not considered in the subtraction, shutters affected by the same source cause self-subtraction. Depending on the source size and spatial gradients, this may bias the shape of the spectrum and the total flux. This data release does not include size measurements, so users are encouraged to check individually.

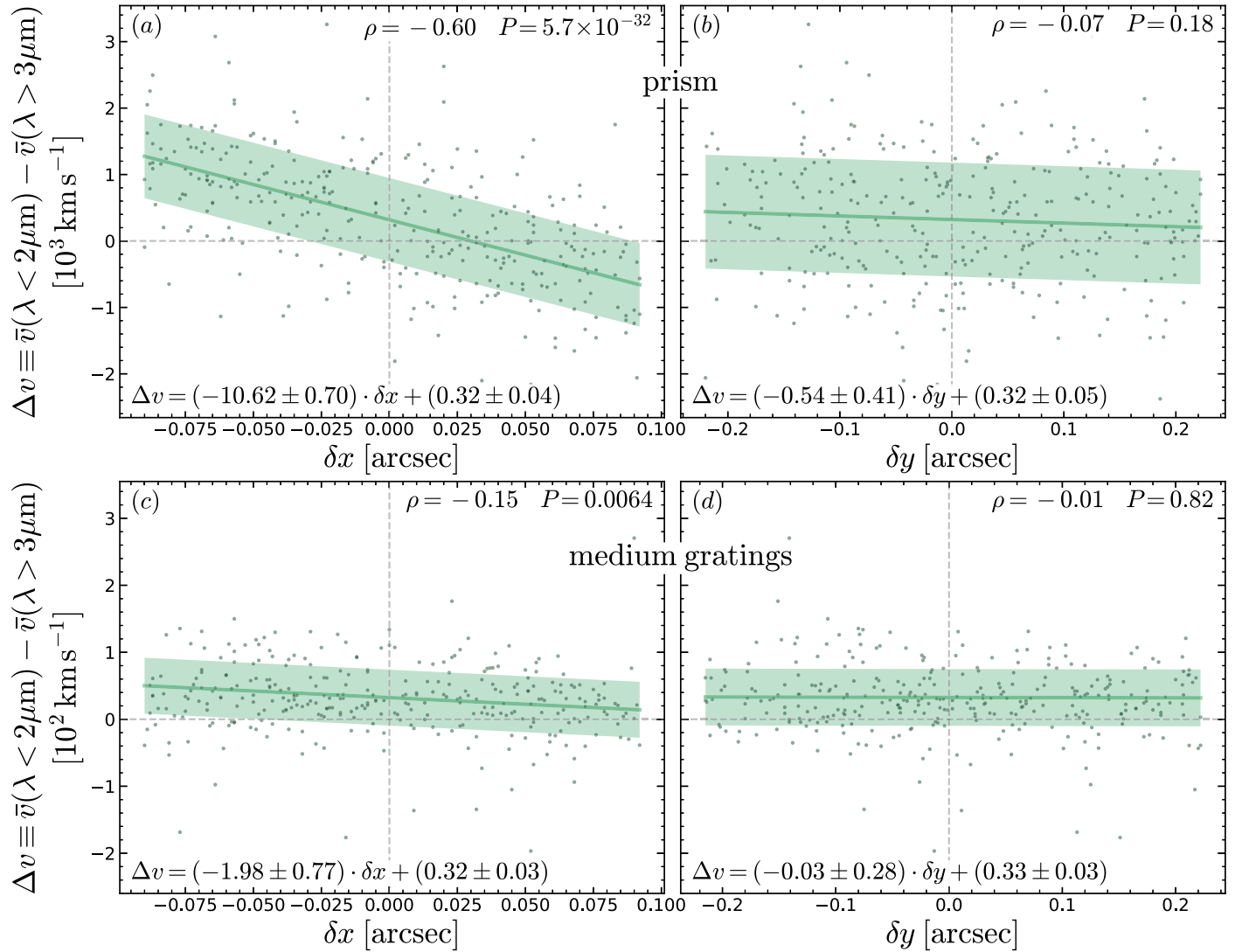


Figure 13. Wavelength calibration bias as a function of intrashutter source position, for both the prism (top) and medium gratings (bottom). δx is the spatial offset of the target with respect to the center of the microshutter, measured along the dispersion direction. For an unbiased wavelength solution, we would expect $\Delta v = 0$ at $\delta x = 0$ and $\delta y = 0$, and no correlation. The observed correlation with δx means that the correction we adopted for the intrashutter source position is insufficient (see Section 5 and P. Ferruit et al. 2022); δx increases toward bluer wavelengths. Neglecting intrashutter source position entirely would result in an even larger bias than what reported here.

4. *Noise spectrum.* The noise spectrum is based on variance-conserving resampling, to mitigate the effect of correlated noise (B. Dorner 2012). A full analysis of correlated noise in NIRSpec will be presented in a future work (P. Jakobsen 2025, in preparation).
5. *Wavelength calibration.* There is a discrepancy between the wavelength calibration of the prism and gratings (causing a typical $\Delta z = 0.0042$; Figure 8). In addition, we find an overall offset in the wavelength calibration of both the prism (mean value of 300 km s^{-1}) and for the gratings (mean value of 30 km s^{-1}). We apply a correction for the wavelength offset due to the intrashutter position of each source, but there is still a residual bias. After correcting empirically for this bias, we show that the prism wavelength offset depends on the spatial location in the MSA (Section 9.3 and Appendix C); for the medium gratings the residual wavelength dependence on the intrashutter position is milder, and we find no detectable trend with spatial location on the MSA.

6. *Flux calibration.* The relative flux calibration between the prism and gratings is accurate to within 15%, and depends on the wavelength (e.g., Figures 5, 16, and 12). The user is encouraged to consider this problem when measuring flux ratios, particularly when comparing between different dispersers and between lines with wide wavelength separation. In addition, the wavelength-dependent flux discrepancy between prism and gratings suggests that emission-line fluxes within the same disperser may also suffer from flux-calibration issues.

11. Highlights

The diversity of the JADES DR3 spectroscopic sample is illustrated by comparing some highlights (Figures 14–20). In Figure 14 we show 200733, an example of a low-redshift quiescent galaxy at $z = 2.86$. NIRCcam photometry (panel (a)) indicates a smooth, peaked light profile with an extended halo, suggesting a high Sérsic index and, therefore, a dynamically

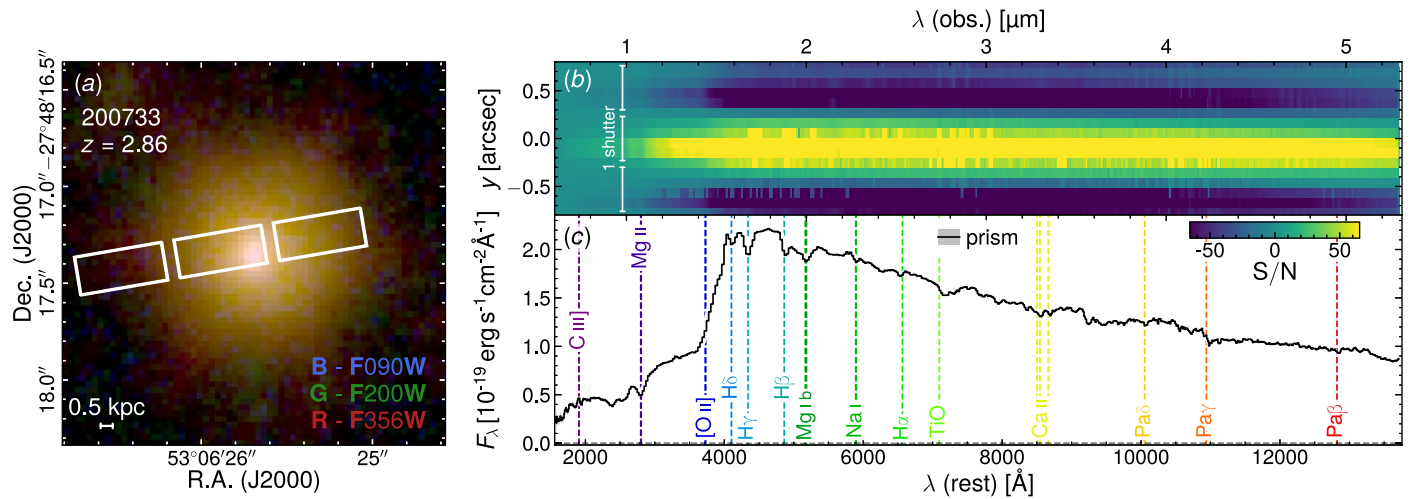


Figure 14. A low-redshift quiescent galaxy, displaying a smooth, peaked light distribution and an evolved stellar population. Panel (a) shows a false-color NIRCам image, with the adopted filters in the bottom right corner. Panel (b) is the NIRSpect/MSA 2D S/N map of the prism spectrum; three shutters are indicated. Here and in all other 2D maps (Figures 15(b)–20(b)), negative S/N is caused by the nod-and-subtract strategy for removing the background. Panel (c) is the 1D, 5 pixel box-car extracted spectrum. Besides the strong 4000 Å break, several stellar and interstellar medium (ISM) absorption features are detected. Notice that the aperture correction applied in this data reduction is optimized for pointlike sources; extended galaxies like 200733 would require both a different aperture correction and a different background-subtraction strategy, to avoid self-subtraction. From W. M. Baker et al. (2024).

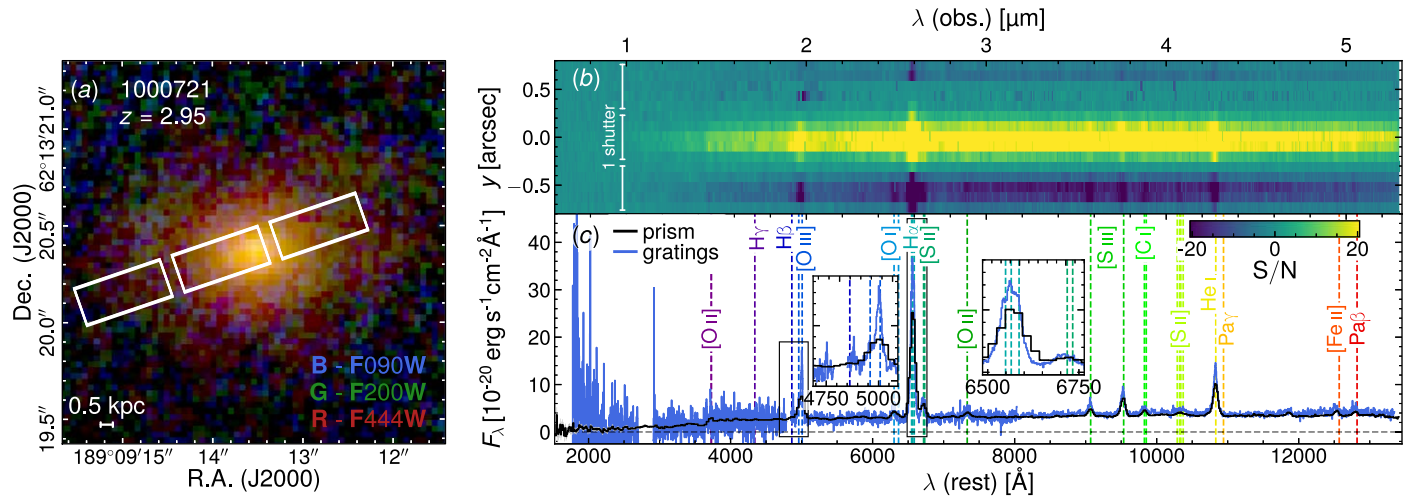


Figure 15. Example of a dust-reddened AGN host, with clear outflows (as seen in the broad component of forbidden [O III] $\lambda\lambda 4959, 5007$, [S II] $\lambda\lambda 6716, 6731$, and [S III] $\lambda\lambda 9069, 9532$), stellar continuum (there is evidence of a Balmer break), and high temperature lines (from the detection of several auroral lines, [O II] $\lambda\lambda 7319\text{--}7332$ and [S II] $\lambda\lambda 10290\text{--}10373$). The blue line in panel (c) is the (spliced) medium-resolution grating spectra (gaps are due to the gaps between the NIRSpect detectors). The black rectangles show details of the $H\beta + [O III] \lambda\lambda 4959, 5007$ and $H\alpha + [N II] \lambda\lambda 6548, 6583$ to [S II] $\lambda\lambda 6716, 6731$ emission-line regions. All other symbols are the same as Figure 14.

evolved system (see W. M. Baker et al. 2024, who find $n = 2.7$). The 1D spectrum (panel (c)) displays the signatures of an evolved stellar population, with a distinct Balmer break (≈ 3750 Å), indicating a 0.5–1 Gyr old stellar population. The galaxy displays a number of stellar absorption features with high equivalent width; the Balmer series, Mg I $\lambda\lambda 5167\text{--}5184$, and the “calcium triplet,” Ca II $\lambda\lambda 8498\text{--}8662$.

At slightly higher redshift ($z = 2.95$) we find 1000721 (Figure 15), an AGN host galaxy with a Type 1 AGN and high-velocity outflows, a secure signature of an active supermassive black hole. The host galaxy is clearly seen in NIRCам; the lack of flux in F090W (see Figure 14(a)) indicates high dust reddening, which is indeed seen in the NIRSpect data (panel (c)). Emission from the [O III] $\lambda\lambda 4959, 5007$ and $H\alpha + [N II] \lambda\lambda 6548, 6583$ complexes is spatially extended (panel (b)), indicating a resolved disk or narrow-line region. In the medium-resolution grating spectra (blue line in panel (c)) the

presence of an outflow can be clearly seen in [O III] $\lambda\lambda 4959, 5007$ and [S II] $\lambda\lambda 6716, 6731$, while $H\alpha$ shows evidence of both ionized-gas outflows and a broad-line region. The prism spectrum (black line) reveals a Balmer break, indicating that the continuum emission is dominated by stars; a number of auroral lines is readily detected in rest-frame r and Y bands.

Pablo’s Galaxy (197911, GS-10578; Figure 16) is a marvelous massive galaxy at $z = 3.06$, identified as quiescent via the UVJ color-color diagram (R. J. Williams et al. 2009). This extraordinary galaxy displays stellar rotation (F. D’Eugenio et al. 2024a), an X-ray and MIR-detected Type 2 AGN (C. Circosta et al. 2019), fast ionized-gas outflows in [O III] $\lambda 5007$, neutral-gas outflows with high mass loading (Na I $\lambda\lambda 5890, 5896$ absorption in panel (c); F. D’Eugenio et al. 2024a), and negligible amounts of molecular gas (molecular gas fraction $f_{\text{gas}} < 0.05\text{--}0.01$; J. Scholtz et al. 2024). Medium-resolution observations spanning the entire NIRSpect wavelength

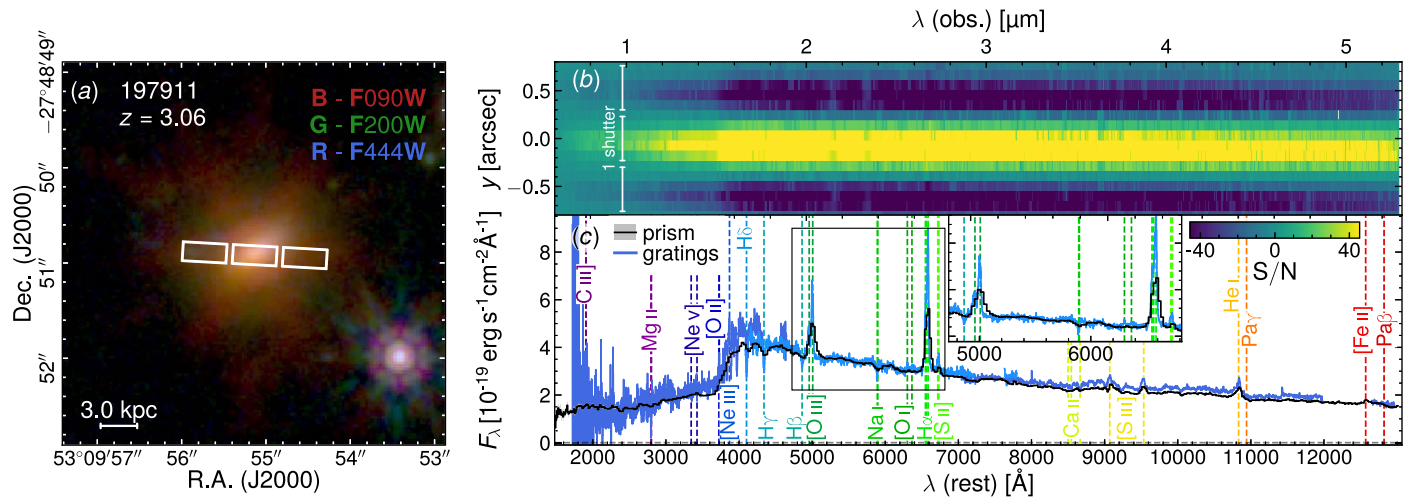


Figure 16. “Pablo’s Galaxy,” a UVJ-quiet galaxy at $z = 3$ hosting an X-ray and mid-infrared (MIR) AGN and multiphase outflows. This system displays a rich set of stellar and ISM absorption lines (Mg II $\lambda\lambda 2796, 2803$ and Na I $\lambda\lambda 5890, 5896$, the latter tracing a fast neutral-gas outflow; F. D’Eugenio et al. 2024a). Emission lines trace both low-ionization gas, including [O II] $\lambda\lambda 3726, 3729$, [O I] $\lambda\lambda 6300, 6363$, [N II] $\lambda\lambda 6548, 6583$, and [S II] $\lambda\lambda 6716, 6731$, possibly due to shocked or stripped gas, as well as higher-ionization species ([Ne V] $\lambda\lambda 3346, 3426$). Note the flux-calibration offset between G140M (blue) and G235M and G395M (light blue; 10%) and G235M and G395M (blue; 7%). Like 200733 (Figure 14), Pablo’s Galaxy is fairly extended, meaning the standard aperture correction and background subtraction are not optimal. From J. Scholtz et al. (2024). All symbols are the same as Figure 14.

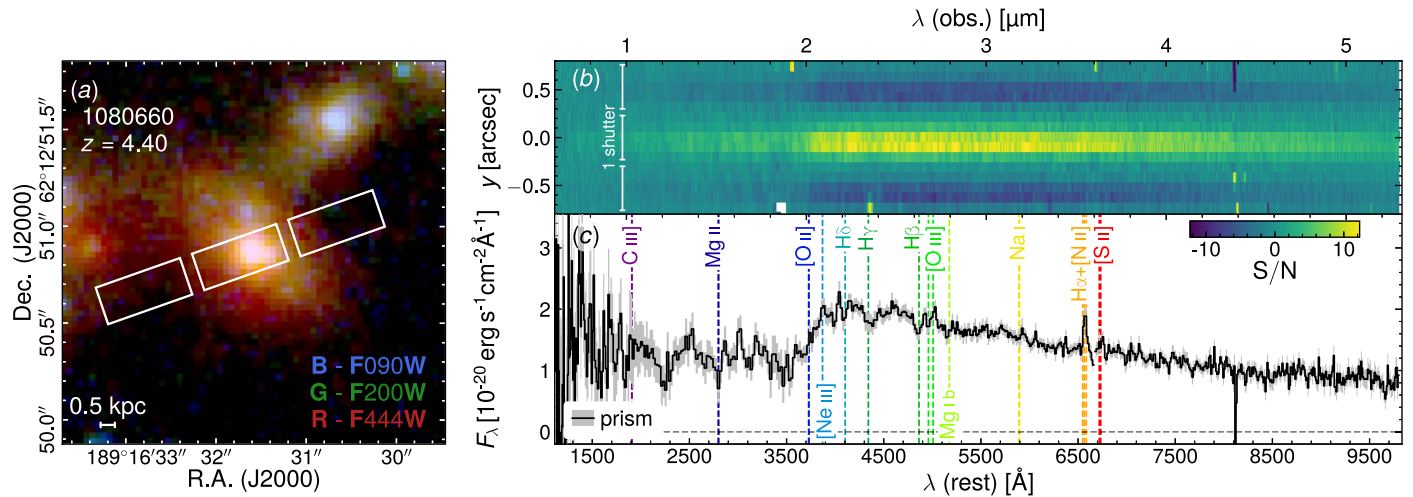


Figure 17. Example of a quiescent galaxy at $z = 4.4$, ID 1080660. This object displays a complex morphology with both a blue core (white in panel (a)) and a redder extended component (in green). The prominent Balmer break and flat rest-frame UV spectrum indicate this galaxy is an early quiescent system. We see clear emission from the $H\alpha + [N II] \lambda\lambda 6548, 6583$ blended complex, from [O III] $\lambda\lambda 4959, 5007$, and from Mg II $\lambda\lambda 2796, 2803$, indicating AGN activity and, possibly, ongoing outflows, as seen in quiescent galaxies at lower redshifts. All symbols and panels are the same as Figure 14.

enable the study of Mg II $\lambda\lambda 2796, 2803$ emission and absorption, high-ionization species ([Ne V] $\lambda\lambda 3346, 3426$), electron densities ([O II] $\lambda\lambda 3726, 3729$ and [S II] $\lambda\lambda 6716, 6731$), and stellar α -element abundance (Mg I $\lambda\lambda 5167\text{--}5184$ and Ca II $\lambda\lambda 8498\text{--}8662$). Stringent upper limits on Pa β disfavor a dust-obscured starburst.

1080660 is an example of a higher-redshift quiescent galaxy at $z = 4.4$ (Figure 17), among the highest-redshift quiescent galaxies known (see A. C. Carnall et al. 2023; T. Nanayakkara et al. 2024). NIRCcam (panel (a)) shows two interlopers (northwest; photometric redshift of 2.5) and a possible dusty companion to the east (1080661, with a photometric redshift of 3.8, but this value is highly uncertain due to the dusty nature of this target). 1080660 itself has an evolved morphology, consisting of a bright central core and more extended emission along the northeast–southwest direction; the extended emission appears significantly redder than the core (green versus white in the false-color image

of panel (a)), suggesting a possible central starburst, as seen in some local poststarburst galaxies (F. D’Eugenio et al. 2020) and, recently, in NIRCcam imaging (L. Wright et al. 2024). The spectrum (panel (c)) exhibits a clear Balmer break, H δ , H γ , and H β absorption, and [O III] $\lambda\lambda 4959, 5007$ and $H\alpha + [N II] \lambda\lambda 6548, 6583$ emission of relatively low equivalent width. There is no evidence for spatially extended nebular emission in the 2D spectrum (panel (c)).

Figure 18 shows 1028761, a merger between a relatively unobscured galaxy and a dusty galaxy at $z = 6.76$. This system displays high values of the emission-line ratios [O II] $\lambda\lambda 3726, 3729$ /[O III] $\lambda 5007$, [N II] $\lambda 6584$ /H α , and [S II] $\lambda\lambda 6716, 6731$ /H α , characteristic of high-metallicity gas or shock-dominated emission.

In Figure 19 we show 99915, which displays a strong single emission line at $4.8 \mu\text{m}$. The line is also seen in the G395M grating spectrum, and in the NIRCcam grism spectrum

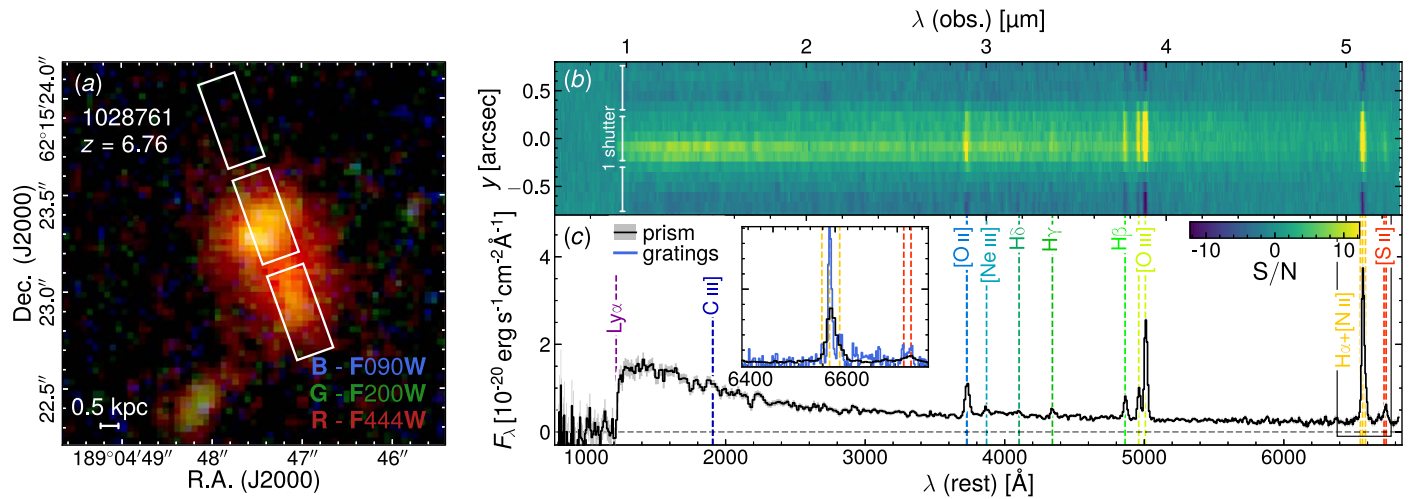


Figure 18. Example of a high-redshift galaxy with high metallicity and/or signatures of shocked gas, ID 1028761. The NIRSpec 2D S/N map (panel (b)) clearly reveals spatially extended emission; a different background-subtraction strategy is clearly required for this class of targets. In cases like this, using the provided emission-line fluxes may result in unphysical line ratios, or harder-to-identify bias. From A. Cameron et al. (2025, in preparation). All symbols and panels are the same as Figure 14.

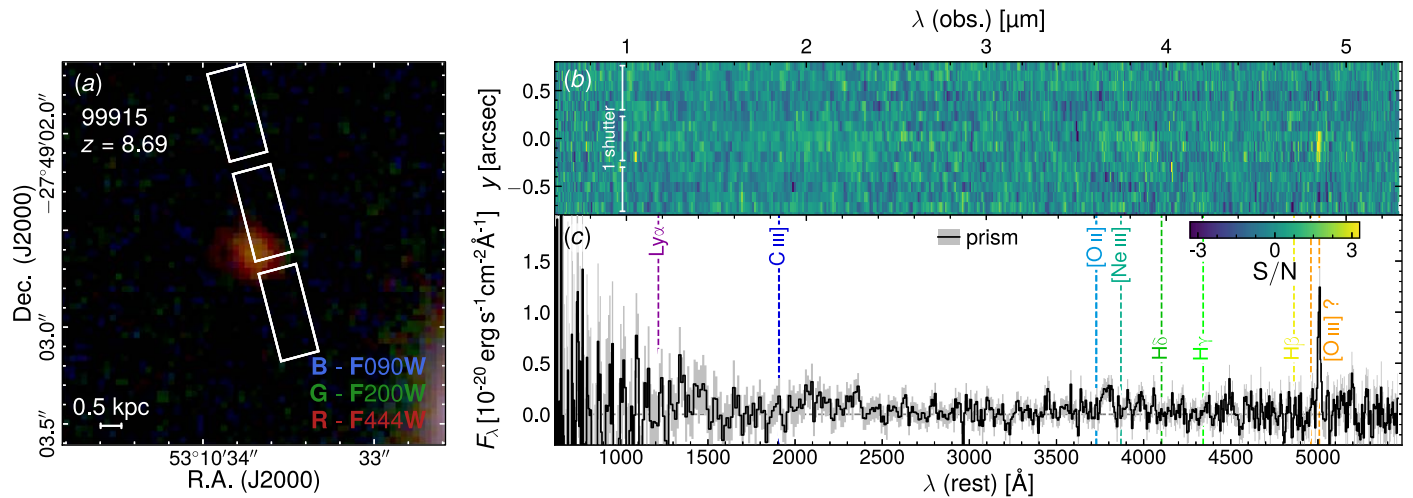


Figure 19. Example of a high-redshift galaxy with an uncertain redshift, ID 36424. The clear emission line at $4.8 \mu\text{m}$ could be identified as H α , but this would be inconsistent with the photometric break between F090W and F115W. A tentative identification of the line as [O III] $\lambda 5007$ is presented here; while consistent with the photometric break, this solution is itself problematic due to the missing [O III] $\lambda 5007$ [$\lambda 4959$]. We can rule out an artifact, because the line is also detected in our G395M spectrum and in the NIRCcam grism (from FRESCO; P. A. Oesch et al. 2023a; see also F. Sun et al. 2025, in preparation). All symbols and panels are the same as Figure 14.

(F. Sun et al. 2025, in preparation), which rules out an artifact. The galaxy also shows a photometric drop between the NIRCcam F090W and F150W filters, which at face value rules out a solution where the emission line is H α . Identifying the line as either H β or [O III] $\lambda 5007$ would match the Ly α break— seen in NIRCcam, but is not without problems. If the line was H β , we would expect to observe H γ at about half the H β flux; similarly, the tentative solution at $z = 8.69$, which identifies the observed line with [O III] $\lambda 5007$, would require observing [O III] $\lambda 5007$ [$\lambda 4959$] at about one-third of the line flux. None of these accompanying lines (the putative H γ nor [O III] $\lambda 5007$ [$\lambda 4959$]) are seen either in prism, grating, or NIRCcam grism data, leaving this object as a tentative redshift determination.

Finally, in Figure 20 we show JADES-GS-z12-0 (E. Curtis-Lake et al. 2023; B. E. Robertson et al. 2023), which at the time of this data release is the highest-redshift detection of a metal emission line (F. D'Eugenio et al. 2024b). The data included in this release consist separately of observations from PID 3215 and PID 1210. In this data release, we use the redshift from

F. D'Eugenio et al. (2024b), based off clearly detected C III] $\lambda\lambda 1907, 1909$ emission. This value is lower than the redshift reported in our previous articles (E. Curtis-Lake et al. 2023, B. E. Robertson et al. 2023, B24); the latter was measured from the wavelength of the Ly α break, assuming only intergalactic medium absorption, and the discrepancy with the C III] $\lambda\lambda 1907, 1909$ redshift is explained by damped Ly α (DLA) absorption (e.g., A. M. Wolfe et al. 2005). Increasing evidence is building up that a substantial fraction of $z > 10$ galaxies may have DLA absorption (e.g., K. E. Heintz et al. 2024), which may bias photometric and Ly α -drop redshifts to higher values (e.g., F. D'Eugenio et al. 2024b; see especially K. N. Hainline et al. 2024.)

12. Conclusions

In this work, we presented new and updated JADES NIRCcam and NIRSpec observations obtained up until 2023 October in the two GOODS fields. The spectra include both medium-depth and deep observations up to redshift $z \sim 13$, reaching the deepest unlensed spectroscopic observations to date (up to 45 hr on

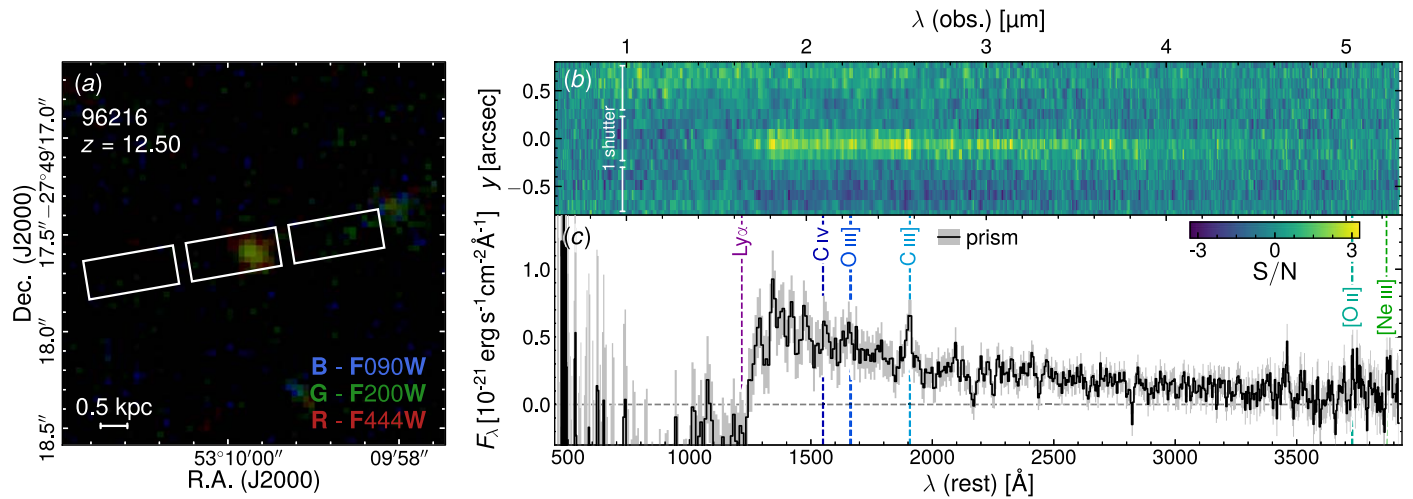


Figure 20. One of the highest-redshift sources in this data release, 96216 (JADES-GS-z12-0; E. Curtis-Lake et al. 2023; B. E. Robertson et al. 2023; 2773; B24). This system shows the highest-redshift detection of metals to date (F. D'Eugenio et al. 2024b). All symbols and panels are the same as Figure 14.

source). The sample size and data quality of the spectra are a testament to the success of the NIRSpec/MSA instrument. The high success rate of the redshift identification validates the selection criteria, including the quality of NIRCcam data, the accuracy of the photometric analysis, and the precision of the photometric redshift determination with EAZY and BEAGLE.

We release fully reduced and calibrated images and spectra, and present catalogs of photometry, photometric redshifts, spectroscopic redshifts, and emission-line fluxes. Insight from this large sample enabled us to pin down some remaining challenges in the data reduction: a mismatch in the redshift and flux calibration between different dispersers, background-subtraction and slit-loss corrections appropriate for extended sources, and residual wavelength calibration issues. Future calibration programs will certainly address these problems. An additional challenge is deriving weights for each spectroscopic target to recover luminosity functions and number densities, which we will provide in the next data release.

In the future, significantly larger samples of the general galaxy population in the redshift and mass range probed by JADES would require a substantial investment of JWST time, or a revised observing strategy. Larger samples of specific classes of objects will still be crucial for understanding rare types, where JADES has only hinted at the potential (e.g., high-redshift quiescent galaxies, extremely reddened galaxies, little red dots, and $z > 8$ Ly α emitters).

In the meantime, the current sample is the largest extragalactic sample with low- and medium-resolution spectroscopy spanning 0.6–5.3 μm ; the depth of the medium and deep spectra, and the synergy with medium- and wide-band imaging, enables for the first time a statistical study combining morphology and rest-frame optical spectroscopy of galaxies between the peak of the SFR density and the first few hundred Myr after the Big Bang.

Acknowledgments

F.D.E., J.S., R.M., T.J.L., J.W., W.M.B., X.J., I.J., and C.S. acknowledge support by the Science and Technology Facilities Council (STFC), by the ERC through Advanced Grant 695671 “QUENCH,” and by the UKRI Frontier Research grant RISEandFALL. R.M. also acknowledges funding from a research professorship from the Royal Society. A.J.C., A.J.B., J.C., A.S., and G.C.J. acknowledge funding from the

“FirstGalaxies” Advanced Grant from the European Research Council (ERC) under the European Union’s Horizon 2020 research and innovation program (grant agreement No. 789056) S.C., E.P., and G.V. acknowledge support by the European Union’s HE ERC Starting grant No. 101040227 - WINGS. E.C. L. acknowledges support of an STFC Webb Fellowship (ST/W001438/1). S.A., B.R.P., and M.P. acknowledge support from grant PID2021-127718NB-I00 funded by the Spanish Ministry of Science and Innovation/State Agency of Research (MICIN/AEI/ 10.13039/501100011033). M.P. also acknowledges support from the Programa Atracción de Talento de la Comunidad de Madrid via grant 2018-T2/TIC-11715. C.N.A.W., B.E.R., B.D.J., D.J.E., P.A.C., E.E., M.J.R., and F.S. acknowledge JWST/NIRCcam contract to the University of Arizona NAS5-02015. B.E.R. also acknowledges support from the JWST Program 3215. D.J.E. is supported as a Simons Investigator. The Cosmic Dawn Center (DAWN) is funded by the Danish National Research Foundation under grant DNR140. S.T. acknowledges support by the Royal Society Research grant G125142. H.Ü. gratefully acknowledges support by the Isaac Newton Trust and by the Kavli Foundation through a Newton-Kavli Junior Fellowship. This research is supported in part by the Australian Research Council Centre of Excellence for All Sky Astrophysics in 3 Dimensions (ASTRO 3D), through project No. CE170100013. A.L.D. thanks the University of Cambridge Harding Distinguished Postgraduate Scholars Program and Technology Facilities Council (STFC) Center for Doctoral Training (CDT) in Data intensive science at the University of Cambridge (STFC grant number 2742605) for a PhD studentship. Funding for this research was provided by the Johns Hopkins University, Institute for Data Intensive Engineering and Science (IDIES). P.G.P.-G. acknowledges support from grant PID2022-139567NB-I00 funded by Spanish Ministerio de Ciencia e Innovación MICIN/AEI/10.13039/501100011033, FEDER, UE. D.P. acknowledges support by the Huo Family Foundation through a P.C. Ho PhD Studentship. M.S.S. acknowledges support by the Science and Technology Facilities Council (STFC) grant ST/V506709/1. R.S. acknowledges support from a STFC Ernest Rutherford Fellowship (ST/S004831/1). N.C.V. acknowledges support from the Charles and Julia Henry Fund through the Henry Fellowship. The research of C.C.W. is supported by NOIRLab, which is

managed by the Association of Universities for Research in Astronomy (AURA) under a cooperative agreement with the National Science Foundation. This work was performed using resources provided by the Cambridge Service for Data Driven Discovery (CSD3) operated by the University of Cambridge Research Computing Service (<http://www.csd3.cam.ac.uk>), provided by Dell EMC and Intel using Tier-2 funding from the Engineering and Physical Sciences Research Council (capital grant EP/T022159/1), and DiRAC funding from the Science and Technology Facilities Council (<http://www.dirac.ac.uk>). The authors acknowledge use of the lux supercomputer at UC Santa Cruz, funded by NSF MRI grant AST 1828315. This study made use of the Prospero high-performance computing facility at Liverpool John Moores University.

Facility: JWST (NIRCam), JWST (NIRSpec/MSA), HST (ACS), HST (WFC3)

Software: astropy²⁸ (Astropy Collaboration et al. 2013), corner²⁹ (D. Foreman-Mackey 2016), ds9³⁰ (W. A. Joye & E. Mandel 2003), emcee³¹ (D. Foreman-Mackey et al. 2013), fitsmap³² (R. Hausen & B. E. Robertson 2022), fsps³³ (C. Conroy et al. 2009; C. Conroy & J. E. Gunn 2010), ltsfit³⁴ (M. Cappellari et al. 2013), matplotlib³⁵ (J. D. Hunter 2007), numpy³⁶ (C. R. Harris et al. 2020), ppxf³⁷

(M. Cappellari 2017, 2023), scipy³⁸ (P. Virtanen et al. 2020), smplotlib³⁹ (J. Li 2023), and topcat⁴⁰ (M. B. Taylor 2005).

Appendix A Observations Affected by Microshutter Array Short Circuits

Some observations in this data release were affected by MSA short circuits, or “shorts.” For most programs, these were only a minority, and were excluded from the data reduction (e.g., PID 3215, Section 3.6). However, for PID 1180 shorts affected two-thirds of the initial observations. The brightness of the shorts emission can vary drastically between occurrences: the brightest can render the entire integration unusable (Figure 21), while the faintest may contaminate only a few sources near the affected region of the field of view.

As we argued in Section 3.2, these shorts-contaminated data are still useful to measure redshifts, and are included in this data release (Figure 22).

There are three major ways in which shorts affect the quality of the data. First, shorts increase the background level, reducing the S/N of the observations. Second, the shorts’ background is tied to a given exposure, and, therefore can vary

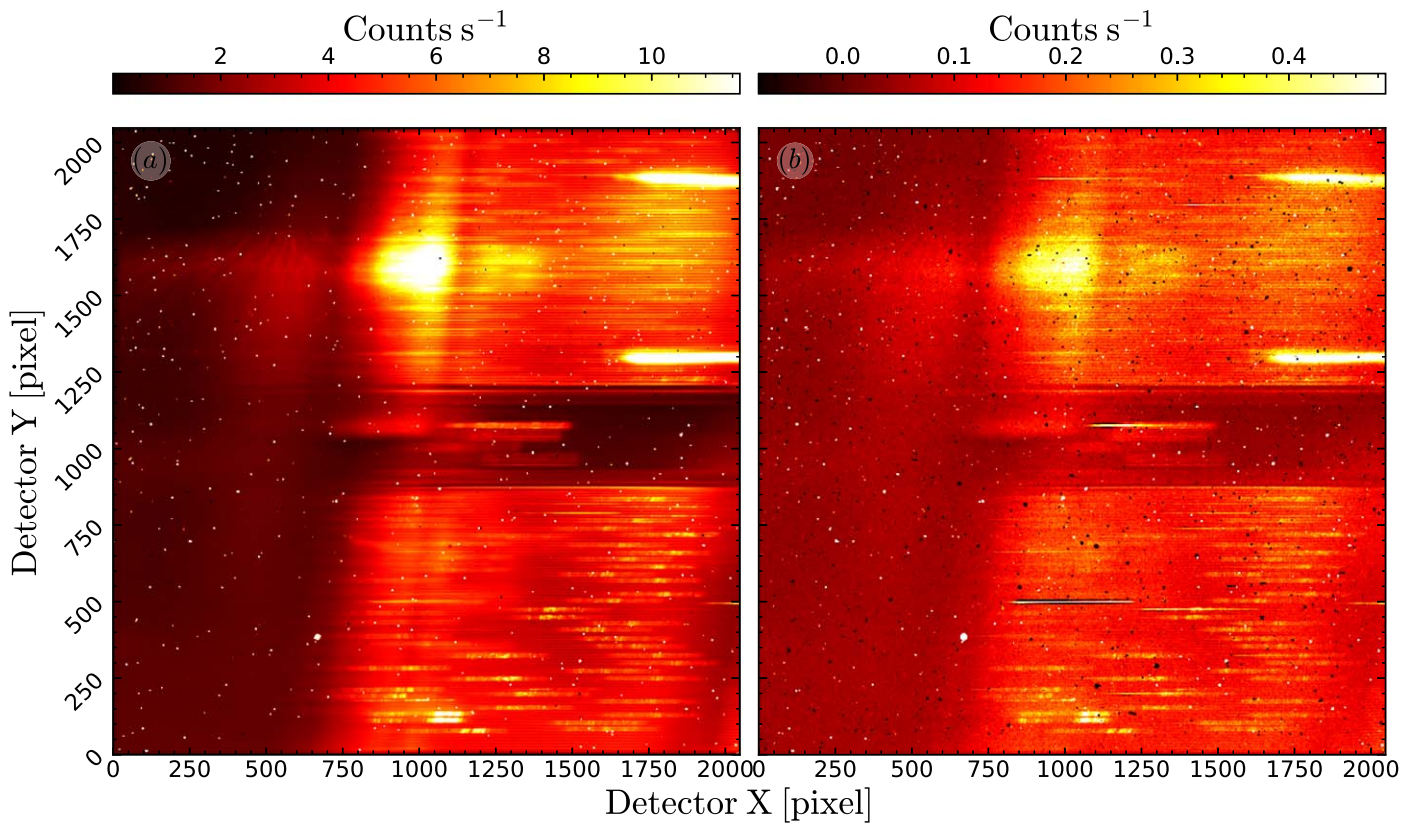


Figure 21. Imaging count-rate maps from NIRSpec detector NRS1 carried out during one of the visit of program PID 1180. Left and right panels illustrate the effect of the short circuits on the count-rate maps before (left) and after (right) background subtraction.

²⁸ <https://pypi.org/project/astropy/>

²⁹ <https://pypi.org/project/corner/>

³⁰ <https://sites.google.com/cfa.harvard.edu/saoimageds9>

³¹ <https://pypi.org/project/emcee/>

³² <https://github.com/ryanhausen/fitsmap>

³³ <https://github.com/cconroy20/fsps>

³⁴ <https://pypi.org/project/ltsfit/>

³⁵ <https://pypi.org/project/matplotlib/>

³⁶ <https://pypi.org/project/numpy/>

³⁷ <https://pypi.org/project/ppxf/>

³⁸ <https://pypi.org/project/scipy/>

³⁹ <https://github.com/AstroJacobLi/smplotlib>

⁴⁰ <https://www.star.bris.ac.uk/~mbt/topcat/>

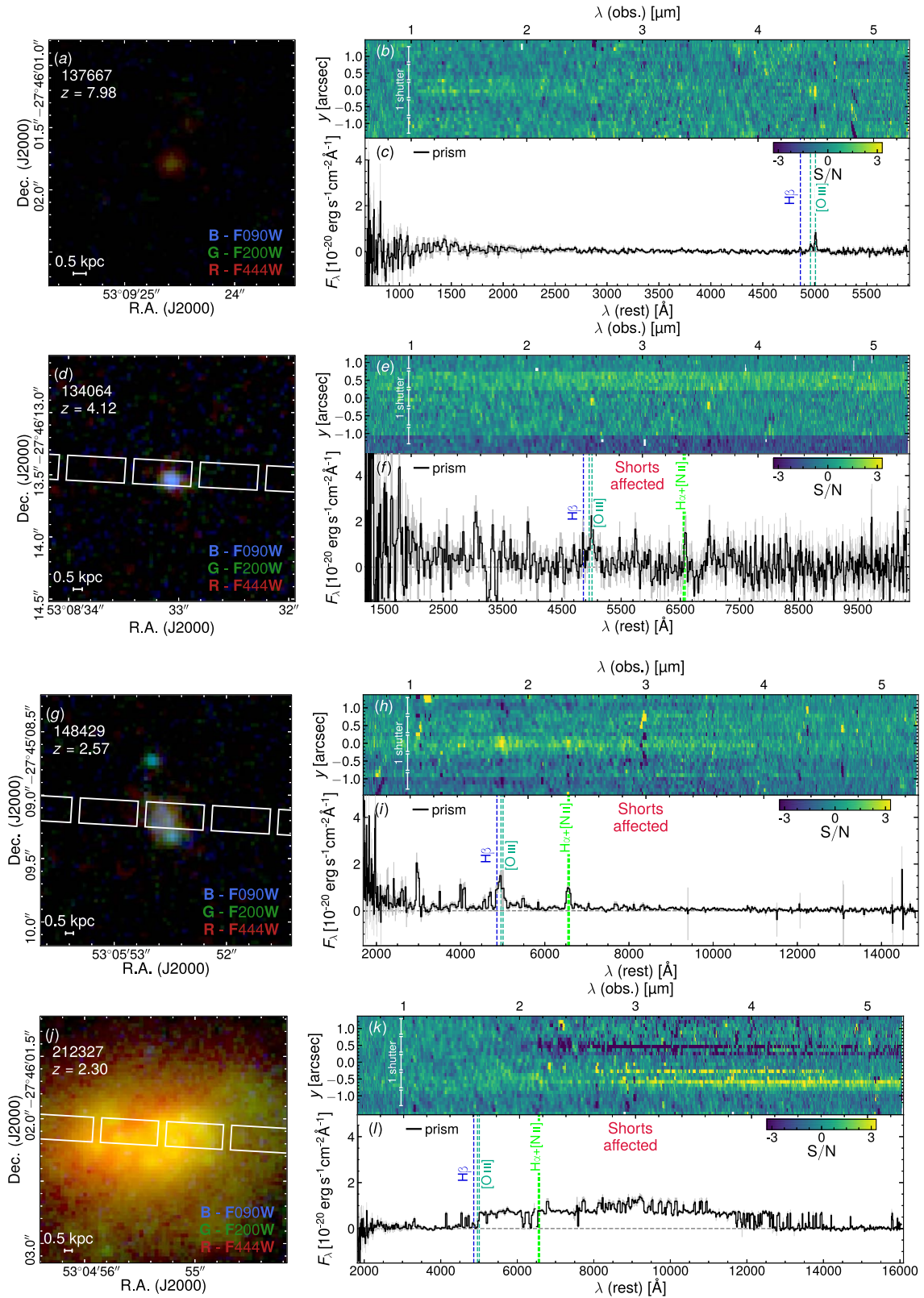


Figure 22. A selection of targets from Program 1180, comparing a successful observation (panels (a)–(c)) and an observation affected by ‘shorts’ (panels (d)–(l)). The successful observation shows the expected S/N both in the 2D map (panel (b)) and in the extracted 1D spectrum (panel (c)). In contrast, panels (e), (h), and (k) show clear problems. Panel (e) shows different background levels between different nod positions, resulting in horizontal striping. Panels (h) and (k) have similar background to panel (b), but the shorts affect the data-reduction pipeline in other ways. For 148429, the shorts are likely responsible for the excess of outliers in the region 1–2 μ m; nevertheless, the data can still be used to measure the galaxy redshift. For 212327 (whose redshift is known from the medium-resolution grating), the shorts caused a misalignment of the already extended source; the resulting data are unusable.

between different sky and nod positions; this causes our background subtraction to fail, because our strategy assumes the same background between different nods. Third, the combination of increased and varying background affects subsequent steps of the pipeline, which can cause excessive or insufficient outlier removal. Users are encouraged to treat these observations with caution, particularly for measurements using the spectral continuum. The flag `DR_flag` in the published tables identifies all spectra where there is a problem in the data reduction, or where the observations were affected by shorts (including when the actual contamination is low).

Appendix B Comparison with Data Release 1

In this section, we compare the measurements obtained by applying the algorithms used in this data release (DR3), to the data previously released in DR1 (B24). We remark that NIRSpec DR1 and DR3 use the same data reduction, hence the spectra are exactly the same as in B24. In Figure 23 we compare the flux

(top rows) and uncertainties (bottom rows) between DR3 and DR1. We find excellent agreement for the overall flux measurements, even though some bright lines ($F > \times 10^{18} \text{ erg s}^{-1} \text{ cm}^{-2}$, panel (a)) display highly significant differences.

Unlike for flux, the measurement uncertainties from DR3 and DR1 are different, with the present values 3% smaller. We find a statistically significant trend with flux, suggesting the mismatch in the uncertainties is due to systematics at the bright end of the sample; adding 1% systematic uncertainty to the flux measurements removes this correlation (gray points in panel (d)).

The agreement presented in Figure 23 varies from line to line; in Figure 24, as an example, we show $\text{H}\beta$. Here the DR3 fluxes are 4% higher, with the discrepancy correlating with flux and decreasing with redshift, as expected from the continuum correction applied by PPXF, and not present in the local-continuum subtraction adopted in DR1.

A similar result is found for the medium-resolution gratings (Figure 25), where again we find excellent agreement in the overall flux (within 1%), but smaller uncertainties (by 16%).

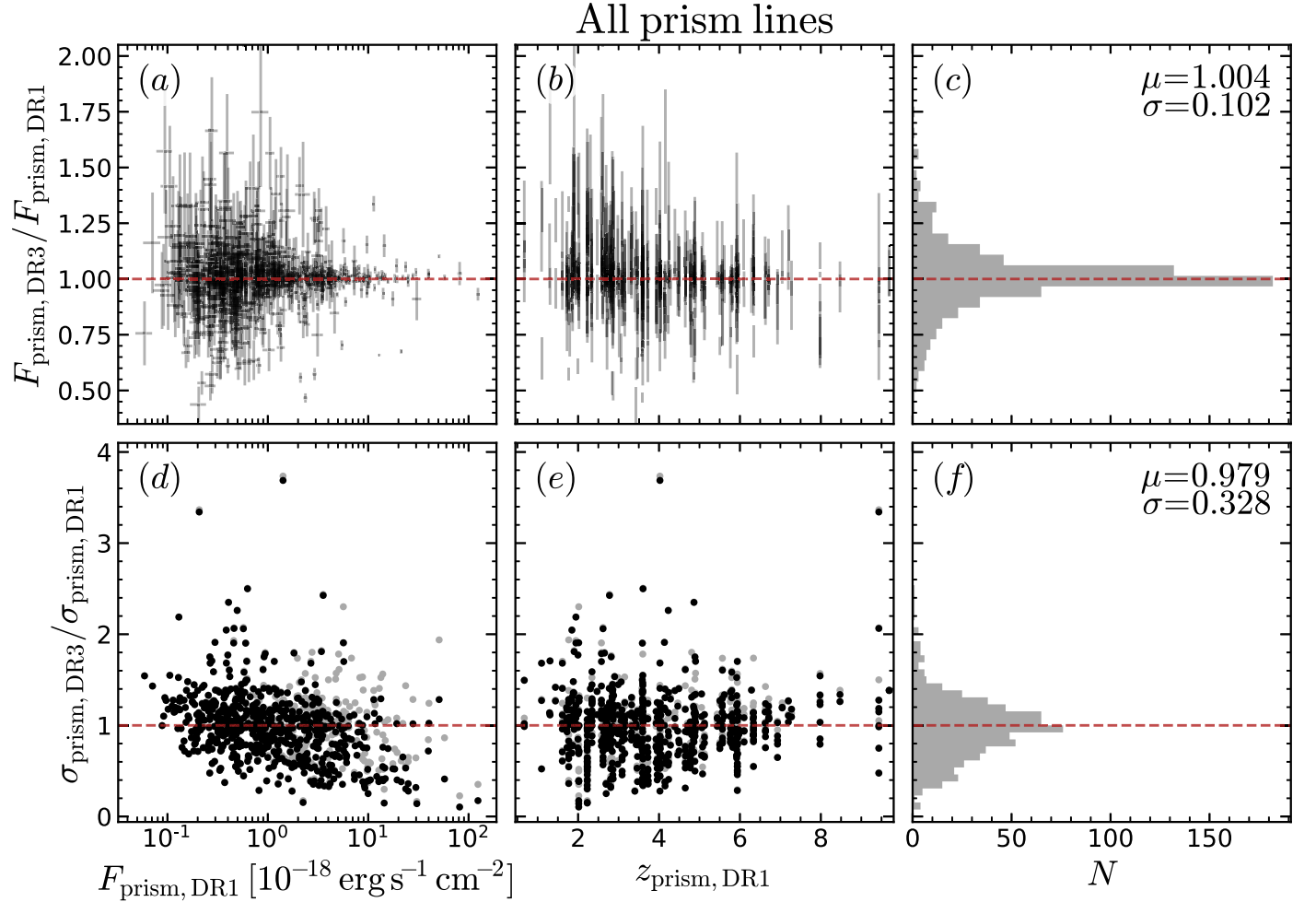


Figure 23. Comparison of the prism emission-line fluxes and their uncertainties between DR1 and DR3: the top row compares the fluxes, the bottom row compares the uncertainties. We find a statistically significant correlation between the ratio of uncertainties and flux (panel (d)), indicating that our PPXF implementation tends to underestimate the line noise in the high-S/N regime, relative to DR1. The gray points in the bottom panel illustrate the effect of adding 1% relative uncertainties to the DR3 flux measurements.

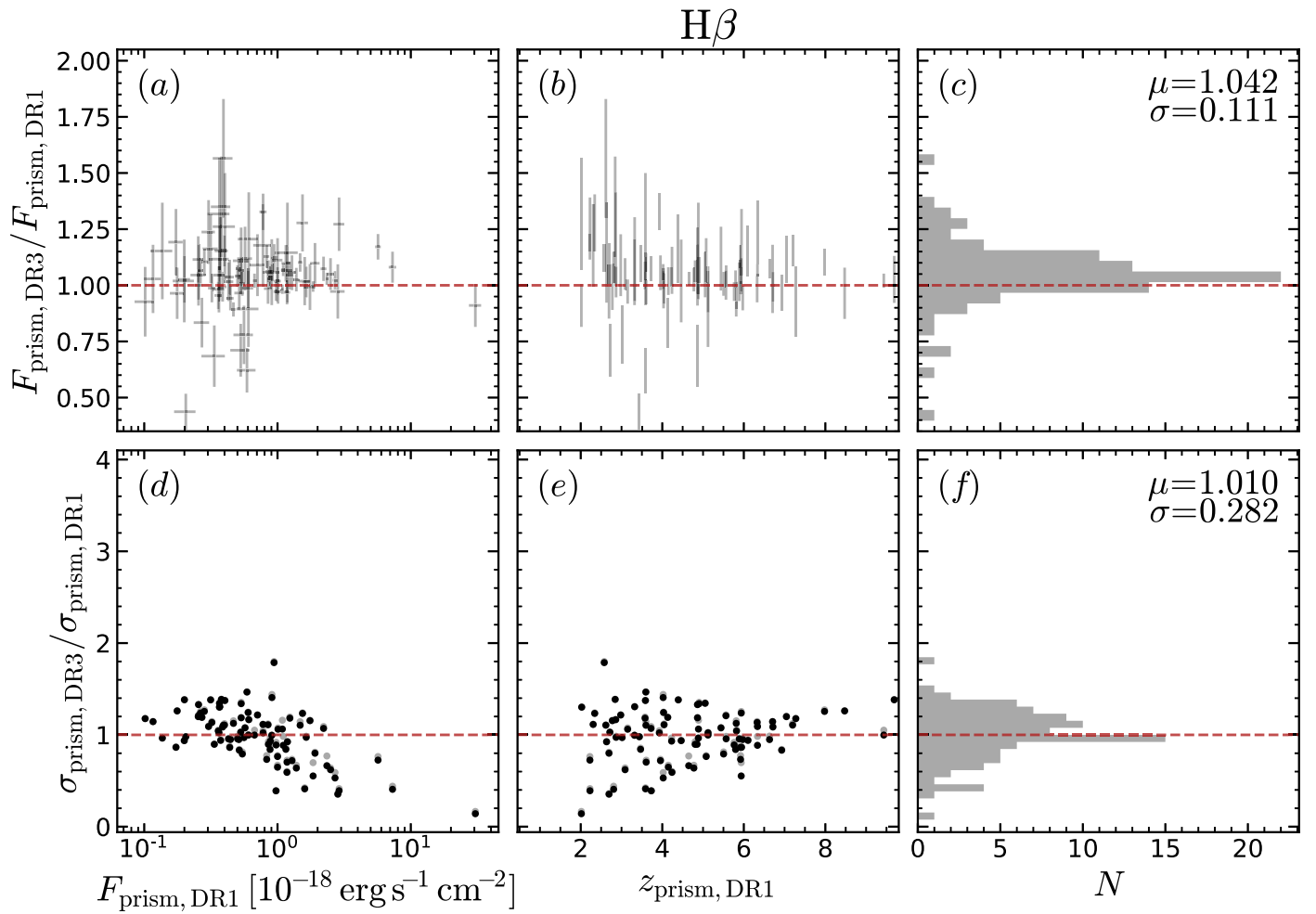


Figure 24. Comparison of the $H\beta$ flux measured from the prism between DR1 and DR3; the symbols are the same as in Figure 23. Below redshift $z = 2$, $H\beta$ is blended with $[O \text{ III}] \lambda\lambda 4959, 5007$ and is not reported in this figure. The $H\beta$ flux ratio between DR3 and DR1 is 1.04, while for all emission lines the ratio is 1.003.

All medium-gratings lines

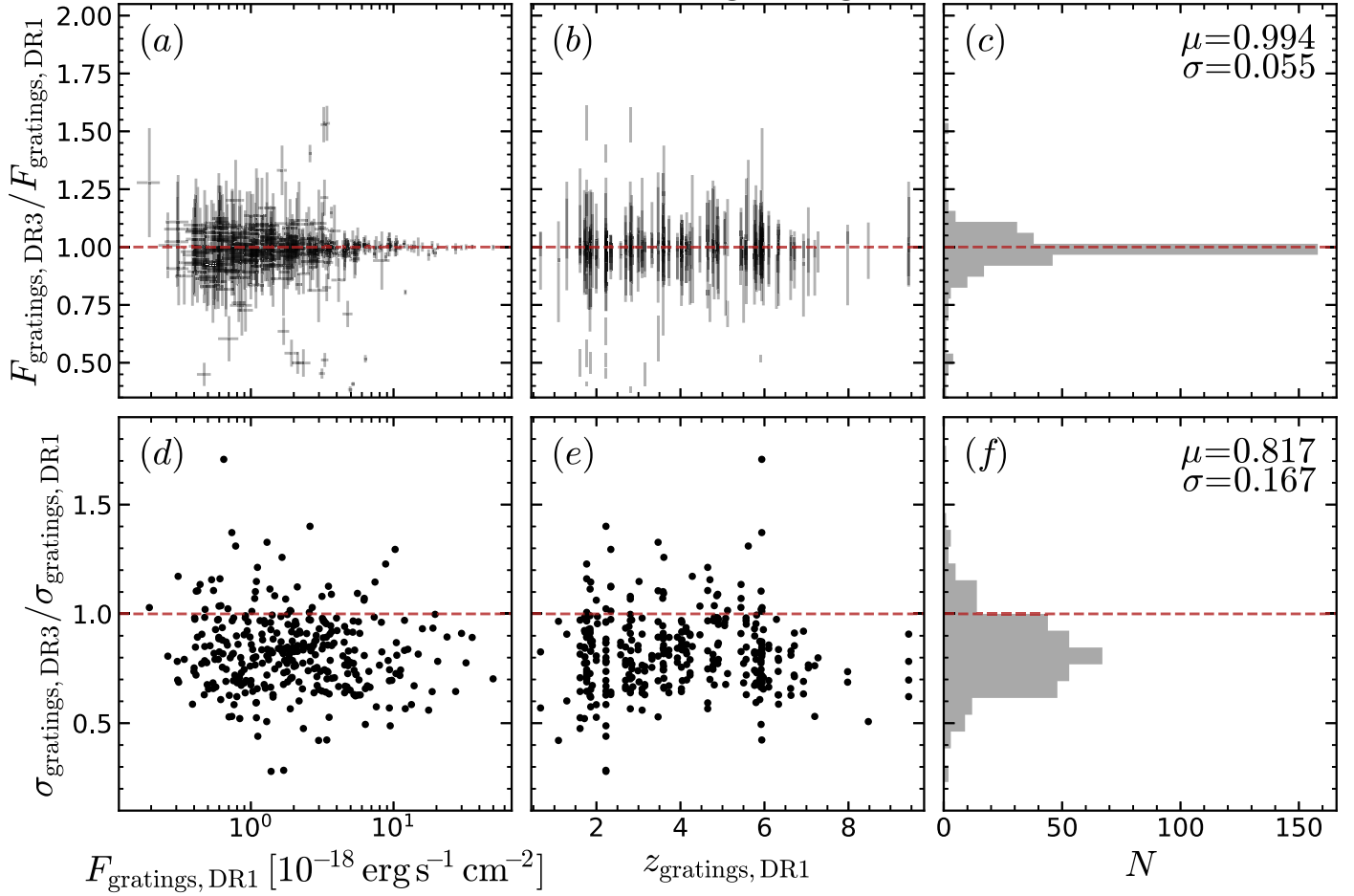


Figure 25. Comparison of the medium-resolution emission-line fluxes and their uncertainties between DR1 and DR3: the top row compares the fluxes, the bottom row compares the uncertainties. Fluxes are in excellent agreement, while we find the uncertainties to be smaller by 20%, on average.

Appendix C Field Dependence of the Prism Wavelength Calibration Bias

In this appendix, we show that the bias in the wavelength calibration of the prism spectra has a residual dependence on the source position within the MSA. We calculate $\Delta\nu$ for each galaxy (with the same definitions and cuts as in Section 9), then average $\Delta\nu$ inside each of the four MSA quadrants. This reveals a bias only in quadrant 2 (hereafter, Q2), with a 4σ detection. We then use the best-fit linear relation of Figure 13

to remove the wavelength bias trend with δx , and repeat the test. The results are shown in Figure 26; there is a clearly detected zero-point offset in $\langle\Delta\nu\rangle$, as expected from Figure 13. The offset is smallest in quadrant 3 (Q3; 2.5σ significance) and highest in Q2 (8σ), with intermediate values in Q1 and quadrant 4 (Q4; $3-4\sigma$ significance). The diagonal direction from Q3 to Q2 is also the direction where the field-dependent spectral resolution increases, suggesting that the observed bias could be due to insufficient correction of the wavelength bias due to intrashutter source position.

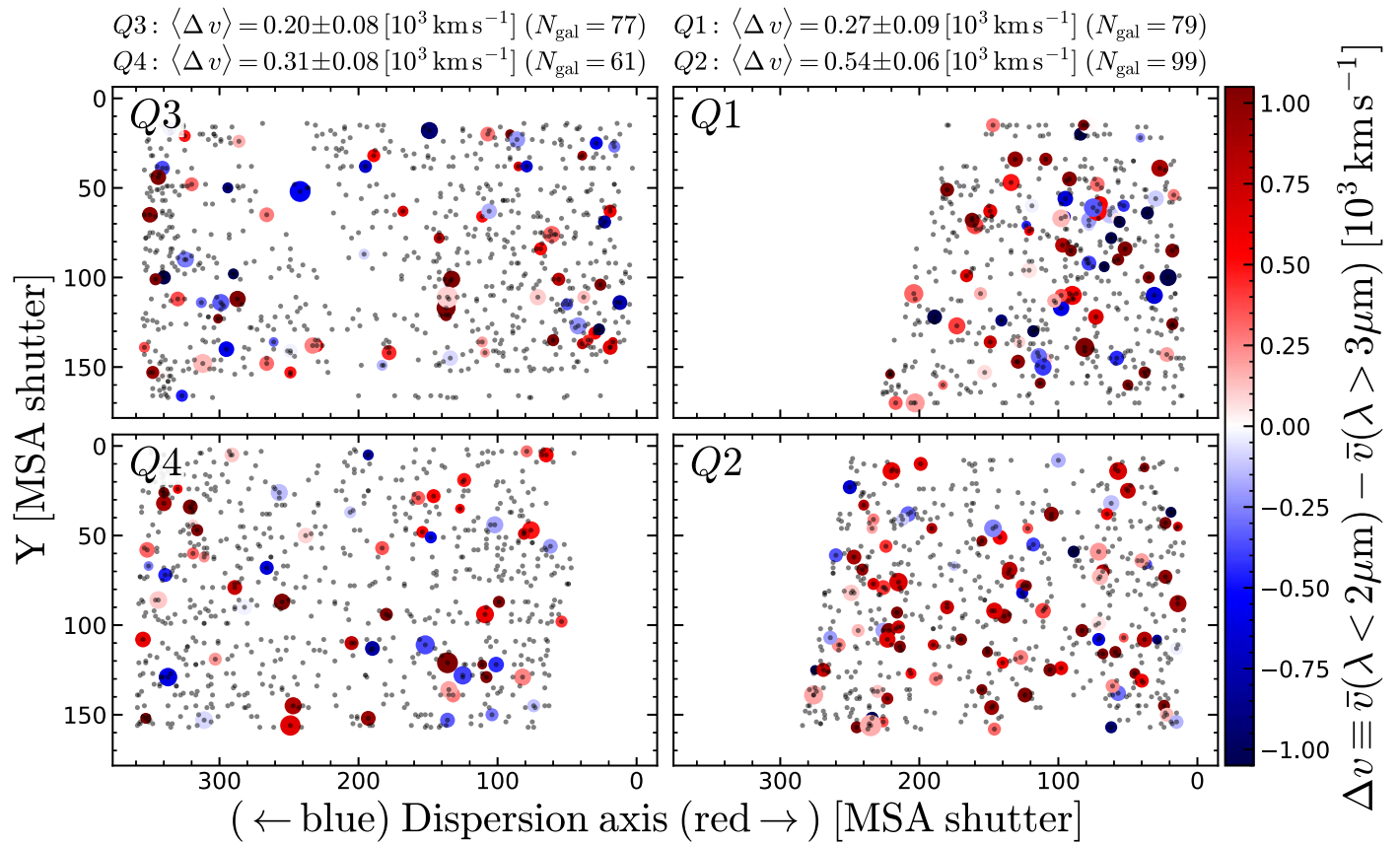


Figure 26. Wavelength solution bias Δv as a function of location on the MSA; the four rectangles are the four MSA quadrants Q1–Q4, with the location of the sample galaxies marked by small gray dots. The large dots represent galaxies with more than four emission lines detected at $S/N > 5$, for which we could calculate the velocity offset between lines observed at wavelengths of 1–2 μm and lines observed at 3–5.3 μm . Δv has been corrected empirically for the residual intrashutter wavelength bias (Section 9). $\langle \Delta v \rangle$ is the average of Δv inside each of the quadrants, illustrating a trend of increasing bias diagonally from Q3 to Q2.

ORCID iDs

Francesco D'Eugenio <https://orcid.org/0000-0003-2388-8172>
 Alex J. Cameron <https://orcid.org/0000-0002-0450-7306>
 Jan Scholtz <https://orcid.org/0000-0001-6010-6809>
 Stefano Carniani <https://orcid.org/0000-0002-6719-380X>
 Chris J. Willott <https://orcid.org/0000-0002-4201-7367>
 Emma Curtis-Lake <https://orcid.org/0000-0002-9551-0534>
 Andrew J. Bunker <https://orcid.org/0000-0002-8651-9879>
 Eleonora Parlanti <https://orcid.org/0000-0002-7392-7814>
 Roberto Maiolino <https://orcid.org/0000-0002-4985-3819>
 Christopher N. A. Willmer <https://orcid.org/0000-0001-9262-9997>
 Peter Jakobsen <https://orcid.org/0000-0002-6780-2441>
 Brant E. Robertson <https://orcid.org/0000-0002-4271-0364>
 Benjamin D. Johnson <https://orcid.org/0000-0002-9280-7594>
 Sandro Tacchella <https://orcid.org/0000-0002-8224-4505>
 Phillip A. Cargile <https://orcid.org/0000-0002-1617-8917>
 Tim Rawle <https://orcid.org/0000-0002-7028-5588>
 Santiago Arribas <https://orcid.org/0000-0001-7997-1640>
 Jacopo Chevallard <https://orcid.org/0000-0002-7636-0534>
 Mirko Curti <https://orcid.org/0000-0002-2678-2560>
 Eiichi Egami <https://orcid.org/0000-0003-1344-9475>
 Daniel J. Eisenstein <https://orcid.org/0000-0002-2929-3121>
 Nimisha Kumari <https://orcid.org/0000-0002-5320-2568>
 Tobias J. Looser <https://orcid.org/0000-0002-3642-2446>
 Marcia J. Rieke <https://orcid.org/0000-0002-7893-6170>
 Bruno Rodríguez Del Pino <https://orcid.org/0000-0001-5171-3930>

Aayush Saxena <https://orcid.org/0000-0001-5333-9970>
 Hannah Übler <https://orcid.org/0000-0003-4891-0794>
 Giacomo Venturi <https://orcid.org/0000-0001-8349-3055>
 Joris Witstok <https://orcid.org/0000-0002-7595-121X>
 William M. Baker <https://orcid.org/0000-0003-0215-1104>
 Rachana Bhatawdekar <https://orcid.org/0000-0003-0883-2226>
 Nina Bonaventura <https://orcid.org/0000-0001-8470-7094>
 Kristan Boyett <https://orcid.org/0000-0003-4109-304X>
 Stephane Charlot <https://orcid.org/0000-0003-3458-2275>
 A. Lola Danhaive <https://orcid.org/0000-0002-9708-9958>
 Kevin N. Hainline <https://orcid.org/0000-0001-9262-9997>
 Ryan Hausen <https://orcid.org/0000-0002-8543-761X>
 Jakob M. Helton <https://orcid.org/0000-0003-4337-6211>
 Xihan Ji <https://orcid.org/0000-0002-1660-9502>
 Zhiyuan Ji <https://orcid.org/0000-0001-7673-2257>
 Gareth C. Jones <https://orcid.org/0000-0002-0267-9024>
 Ignas Juodžbalis <https://orcid.org/0009-0003-7423-8660>
 Michael V. Maseda <https://orcid.org/0000-0003-0695-4414>
 Pablo G. Pérez-González <https://orcid.org/0000-0003-4528-5639>
 Michele Perna <https://orcid.org/0000-0002-0362-5941>
 Dávid Puskás <https://orcid.org/0000-0001-8630-2031>
 Irene Shivaie <https://orcid.org/0000-0003-4702-7561>
 Maddie S. Silcock <https://orcid.org/0009-0002-0651-5761>
 Charlotte Simmonds <https://orcid.org/0000-0003-4770-7516>
 Renske Smit <https://orcid.org/0000-0001-8034-7802>
 Fengwu Sun <https://orcid.org/0000-0002-4622-6617>
 Natalia C. Villanueva <https://orcid.org/0000-0001-6917-4656>

Christina C. Williams  <https://orcid.org/0000-0003-2919-7495>
 Yongda Zhu  <https://orcid.org/0000-0003-3307-7525>

References

- Abazajian, K. N., Adelman-McCarthy, J. K., Agüeros, M. A., et al. 2009, *ApJS*, 182, 543
- Alexander, D. M., Bauer, F. E., Brandt, W. N., et al. 2003, *AJ*, 126, 539
- Alves de Oliveira, C., Birkmann, S. M., Böker, T., et al. 2018, *Proc. SPIE*, 10704, 107040Q
- Arrabal Haro, P., Dickinson, M., Finkelstein, S. L., et al. 2023, *ApJL*, 951, L22
- Ashby, M. L. N., Willner, S. P., Fazio, G. G., et al. 2013, *ApJ*, 769, 80
- Astropy Collaboration, Robitaille, T. P., Tollerud, E. J., et al. 2013, *A&A*, 558, A33
- Baker, W. M., Lim, S., D'Eugenio, F., et al. 2024, arXiv:2410.14773
- Baker, W. M., Maiolino, R., Bluck, A. F. L., et al. 2022, *MNRAS*, 510, 3622
- Barger, A. J., Cowie, L. L., & Wang, W. H. 2008, *ApJ*, 689, 687
- Baro, G., Pérez-González, P. G., Cava, A., et al. 2019, *ApJS*, 243, 22
- Barsanti, S., Colless, M., D'Eugenio, F., et al. 2023, *MNRAS*, 526, 1613
- Beckwith, S. V. W., Stiavelli, M., Koekemoer, A. M., et al. 2006, *AJ*, 132, 1729
- Belli, S., Park, M., Davies, R. L., et al. 2024, *Natur*, 630, 54
- Bezanson, R., Labbe, I., Whitaker, K. E., et al. 2024, *ApJ*, 974, 92
- Bluck, A. F. L., Maiolino, R., Brownson, S., et al. 2022, *A&A*, 659, A160
- Bonaventura, N., Jakobsen, P., Ferruit, P., Arribas, S., & Giardino, G. 2023, *A&A*, 672, A40
- Bouwens, R. J., Illingworth, G. D., Oesch, P. A., et al. 2015, *ApJ*, 803, 34
- Bouwens, R. J., Oesch, P. A., Stefanon, M., et al. 2021, *AJ*, 162, 47
- Boyet, K., Bunker, A. J., Curtis-Lake, E., et al. 2024, *MNRAS*, 535, 1796
- Brammer, G., 2023 grizli, v1.8.10, Zenodo, doi:10.5281/zenodo.7963066
- Brammer, G. B., van Dokkum, P. G., & Coppi, P. 2008, *ApJ*, 686, 1503
- Bunker, A. J., Stanway, E. R., Ellis, R. S., & McMahon, R. G. 2004, *MNRAS*, 355, 374
- Bunker, A. J., Cameron, A. J., Curtis-Lake, E., et al. 2024, *A&A*, 690, A288
- Bunker, A. J., Saxena, A., Cameron, A. J., et al. 2023, *A&A*, 677, A88
- Caldwell, J. A. R., McIntosh, D. H., Rix, H.-W., et al. 2008, *ApJS*, 174, 136
- Cameron, A. J., Katz, H., Witten, C., et al. 2024, *MNRAS*, 534, 523
- Capak, P., Cowie, L. L., Hu, E. M., et al. 2004, *AJ*, 127, 180
- Cappellari, M. 2017, *MNRAS*, 466, 798
- Cappellari, M. 2023, *MNRAS*, 526, 3273
- Cappellari, M., Scott, N., Alatalo, K., et al. 2013, *MNRAS*, 432, 1709
- Carnall, A. C., McLure, R. J., Dunlop, J. S., et al. 2019, *MNRAS*, 490, 417
- Carnall, A. C., McLure, R. J., Dunlop, J. S., et al. 2023, *Natur*, 619, 716
- Chapin, E. L., Pope, A., Scott, D., et al. 2009, *MNRAS*, 398, 1793
- Choi, J., Dotter, A., Conroy, C., et al. 2016, *ApJ*, 823, 102
- Circo, C., Vignali, C., Gilli, R., et al. 2019, *A&A*, 623, A172
- Coe, D., Benítez, N., Sánchez, S. F., et al. 2006, *AJ*, 132, 926
- Conroy, C., & Gunn, J. E., 2010 FSPS: Flexible Stellar Population Synthesis, Astrophysics Source Code Library, ascl:1010.043
- Conroy, C., Gunn, J. E., & White, M. 2009, *ApJ*, 699, 486
- Conroy, C., Naidu, R. P., Zaritsky, D., et al. 2019, *ApJ*, 887, 237
- Cowie, L. L., Barger, A. J., Hsu, L. Y., et al. 2017, *ApJ*, 837, 139
- Curti, M., D'Eugenio, F., Carniani, S., et al. 2023, *MNRAS*, 518, 425
- Curti, M., Maiolino, R., Curtis-Lake, E., et al. 2024, *A&A*, 684, A75
- Curtis-Lake, E., Carniani, S., Cameron, A., et al. 2023, *NatAs*, 7, 622
- Dalton, G., Trager, S. C., Abrams, D. C., et al. 2012, *Proc. SPIE*, 8446, 84460P
- Davies, R. L., Belli, S., Park, M., et al. 2024, *MNRAS*, 528, 4976
- de Jong, R. S., Agertz, O., Berbel, A. A., et al. 2019, *Msngr*, 175, 3
- DESI Collaboration, Aghamousa, A., Aguilar, J., et al. 2016, arXiv:1611.00036
- D'Eugenio, F., Maiolino, R., Carniani, S., et al. 2024b, *A&A*, 689, A152
- D'Eugenio, F., van der Wel, A., Wu, P.-F., et al. 2020, *MNRAS*, 497, 389
- D'Eugenio, F., Pérez-González, P. G., Maiolino, R., et al. 2024a, *NatAs*, 8, 1443
- Dorner, B. 2012, PhD thesis, Université Claude Bernard - Lyon I, <https://theses.hal.science/tel-00738070>
- Driver, S. P., Andrews, S. K., da Cunha, E., et al. 2018, *MNRAS*, 475, 2891
- Eisenstein, D. J., Johnson, B. D., Robertson, B., et al. 2023b, arXiv:2310.12340
- Eisenstein, D. J., Willott, C., Alberts, S., et al. 2023a, arXiv:2306.02465
- Ellis, R. S., McLure, R. J., Dunlop, J. S., et al. 2013, *ApJL*, 763, L7
- Endsley, R., Stark, D. P., Whitler, G., et al. 2024, *MNRAS*, 533, 1111
- Ferruit, P., Jakobsen, P., Giardino, G., et al. 2022, *A&A*, 661, A81
- Finkelstein, S. L., Ryan, R. E. J., Papovich, C., et al. 2015, *ApJ*, 810, 71
- Foreman-Mackey, D. 2016, *JOSS*, 1, 24
- Foreman-Mackey, D., Hogg, D. W., Lang, D., & Goodman, J. 2013, *PASP*, 125, 306
- Fujimoto, S., Arrabal Haro, P., Dickinson, M., et al. 2023, *ApJL*, 949, L25
- Garilli, B., Le Fèvre, O., Guzzo, L., et al. 2008, *A&A*, 486, 683
- Giavalisco, M., Ferguson, H. C., Koekemoer, A. M., et al. 2004, *ApJL*, 600, L93
- Glazebrook, K., Nanayakkara, T., Schreiber, C., et al. 2024, *Natur*, 628, 277
- Goulding, A. D., Greene, J. E., Setton, D. J., et al. 2023, *ApJL*, 955, L24
- Graves, G. J., & Faber, S. M. 2010, *ApJ*, 717, 803
- Grogin, N. A., Kocevski, D. D., Faber, S. M., et al. 2011, *ApJS*, 197, 35
- Guo, Y., Ferguson, H. C., Giavalisco, M., et al. 2013, *ApJS*, 207, 24
- Hainline, K. N., D'Eugenio, F., Jakobsen, P., et al. 2024, *ApJ*, 976, 160
- Hainline, K. N., Johnson, B. D., Robertson, B., et al. 2024, *ApJ*, 964, 71
- Harikane, Y., Ouchi, M., Ono, Y., et al. 2016, *ApJ*, 821, 123
- Harris, C. R., Millman, K. J., van der Walt, S. J., et al. 2020, *Natur*, 585, 357
- Hausen, R., & Robertson, B. E. 2022, *A&C*, 39, 100586
- Heintz, K. E., De Cia, A., Thöne, C. C., et al. 2023, *A&A*, 679, A91
- Heintz, K. E., Watson, D., Brammer, G., et al. 2024, *Sci*, 384, 890
- Herenz, E. C., Urrutia, T., Wisotzki, L., et al. 2017, *A&A*, 606, A12
- Hunter, J. D. 2007, *CSE*, 9, 90
- Inami, H., Bacon, R., Brinchmann, J., et al. 2017, *A&A*, 608, A2
- Jakobsen, P., Ferruit, P., Alves de Oliveira, C., et al. 2022, *A&A*, 661, A80
- Ji, Z., Williams, C. C., Tacchella, S., et al. 2024, *ApJ*, 974, 135
- Jones, G. C., Bunker, A. J., Saxena, A., et al. 2025, *MNRAS*, 536, 2355
- Joye, W. A., & Mandel, E. 2003, in ASP Conf. Ser. 295, Astronomical Data Analysis Software and Systems XII, ed. H. E. Payne, R. I. Jedrzejewski, & R. N. Hook (San Francisco, CA: ASP), 489
- Kauffmann, G., Heckman, T. M., White, S. D. M., et al. 2003a, *MNRAS*, 341, 33
- Kauffmann, G., Heckman, T. M., White, S. D. M., et al. 2003b, *MNRAS*, 341, 54
- Kocevski, D. D., Onoue, M., Inayoshi, K., et al. 2023, *ApJL*, 954, L4
- Koekemoer, A. M., Faber, S. M., Ferguson, H. C., et al. 2011, *ApJS*, 197, 36
- Kokorev, V., Brammer, G., Fujimoto, S., et al. 2022, *ApJS*, 263, 38
- Kriek, M., Shapley, A. E., Reddy, N. A., et al. 2015, *ApJS*, 218, 15
- Kurk, J., Cimatti, A., Daddi, E., et al. 2013, *A&A*, 549, A63
- Leja, J., Carnall, A. C., Johnson, B. D., Conroy, C., & Speagle, J. S. 2019, *ApJ*, 876, 3
- Li, J. 2023, AstroJacobLi/smplotlib: v0.0.8, Zenodo, doi:10.5281/zenodo.796683
- Looser, T. J., D'Eugenio, F., Maiolino, R., et al. 2023, arXiv:2306.02470
- Looser, T. J., D'Eugenio, F., Maiolino, R., et al. 2024, *Natur*, 629, 53
- Lorenzoni, S., Bunker, A. J., Wilkins, S. M., et al. 2011, *MNRAS*, 414, 1455
- Lorenzoni, S., Bunker, A. J., Wilkins, S. M., et al. 2013, *MNRAS*, 429, 150
- Luo, B., Brandt, W. N., Xue, Y. Q., et al. 2017, *ApJS*, 228, 2
- Magnelli, B., Popesso, P., Berta, S., et al. 2013, *A&A*, 553, A132
- Maiolino, R., Cirasuolo, M., Afonso, J., et al. 2020, *Msngr*, 180, 24
- Maiolino, R., Scholtz, J., Witstok, J., et al. 2024a, *Natur*, 627, 59
- Maiolino, R., Übler, H., Perna, M., et al. 2024b, *A&A*, 687, A67
- Maseda, M. V., de Graaff, A., Franx, M., et al. 2024, *A&A*, 689, A73
- Maseda, M. V., van der Wel, A., Rix, H.-W., et al. 2018, *ApJ*, 854, 29
- McLure, R. J., Dunlop, J. S., Bowler, R. A. A., et al. 2013, *MNRAS*, 432, 2696
- Momcheva, I. G., Brammer, G. B., van Dokkum, P. G., et al. 2016, *ApJS*, 225, 27
- Morris, A. M., Kocevski, D. D., Trump, J. R., et al. 2015, *AJ*, 149, 178
- Morrison, G. E., Owen, F. N., Dickinson, M., Ivison, R. J., & Ibar, E. 2010, *ApJS*, 188, 178
- Mullaney, J. R., Pannella, M., Daddi, E., et al. 2012, *MNRAS*, 419, 95
- Murphy, E. J., Momjian, E., Condon, J. J., et al. 2017, *ApJ*, 839, 35
- Nakajima, K., Ouchi, M., Isobe, Y., et al. 2023, *ApJS*, 269, 33
- Nanayakkara, T., Glazebrook, K., Jacobs, C., et al. 2024, *NatSR*, 14, 3724
- Newman, J. A., Cooper, M. C., Davis, M., et al. 2013, *ApJS*, 208, 5
- Oesch, P. A., Bouwens, R. J., Illingworth, G. D., et al. 2010, *ApJL*, 709, L16
- Oesch, P. A., Bouwens, R. J., Illingworth, G. D., et al. 2013, *ApJ*, 773, 75
- Oesch, P. A., Bouwens, R. J., Illingworth, G. D., et al. 2014, *ApJ*, 786, 108
- Oesch, P. A., Brammer, G., Naidu, R. P., et al. 2023, *MNRAS*, 525, 2864
- Oesch, P. A., Brammer, G., van Dokkum, P. G., et al. 2016, *ApJ*, 819, 129
- Oke, J. B., & Gunn, J. E. 1983, *ApJ*, 266, 713
- Peng, Y.-j., Lilly, S. J., Kovač, K., et al. 2010, *ApJ*, 721, 193
- Pentericci, L., McLure, R. J., Garilli, B., et al. 2018a, *A&A*, 616, A174
- Pentericci, L., Vanzella, E., Castellano, M., et al. 2018b, *A&A*, 619, A147
- Rafelski, M., Teplitz, H. I., Gardner, J. P., et al. 2015, *AJ*, 150, 31
- Rauscher, B. J., Arendt, R. G., Fixsen, D. J., et al. 2017, *PASP*, 129, 105003
- Rauscher, M., Arendt, H. I., Fixsen, J. P., et al. 2012, *Proc. SPIE*, 8453, 84531F
- Rawle, T. D., Giardino, G., Franz, D. E., et al. 2022, *Proc. SPIE*, 12180, 121803R
- Reddy, N. A., Steidel, C. C., Erb, D. K., Shapley, A. E., & Pettini, M. 2006, *ApJ*, 653, 1004

- Rieke, M. J., Robertson, B., Tacchella, S., et al. 2023, *ApJS*, 269, 16
- Robertson, B., Johnson, B. D., Tacchella, S., et al. 2024, *ApJ*, 970, 31
- Robertson, B. E., Tacchella, S., Johnson, B. D., et al. 2023, *NatAs*, 7, 611
- Rousseuw, P. J., & Driessen, K. 2006, *Data Min. Knowl. Discov.*, 12, 29
- Salpeter, E. E. 1955, *ApJ*, 121, 161
- Schenker, M. A., Robertson, B. E., Ellis, R. S., et al. 2013, *ApJ*, 768, 196
- Scholtz, J., D'Eugenio, F., Maiolino, R., et al. 2024, arXiv:2405.19401
- Shapley, A. E., Sanders, R., Berg, D., et al. 2021, JWST Proposal, 1914
- Skelton, R. E., Whitaker, K. E., Momcheva, I. G., et al. 2014, *ApJS*, 214, 24
- Stark, D. P., Ellis, R. S., & Ouchi, M. 2011, *ApJL*, 728, L2
- Stark, D. P., Schenker, M. A., Ellis, R., et al. 2013, *ApJ*, 763, 129
- Stott, J. P., Swinbank, A. M., Johnson, H. L., et al. 2016, *MNRAS*, 457, 1888
- Strait, V., Brammer, G., Muzzin, A., et al. 2023, *ApJL*, 949, L23
- Sun, F., Egami, E., Pirzkal, N., et al. 2023, *ApJ*, 953, 53
- Tamura, N., Takato, N., Shimono, A., et al. 2016, *Proc. SPIE*, 9908, 99081M
- Tasca, L. A. M., Le Fèvre, O., Ribeiro, B., et al. 2017, *A&A*, 600, A110
- Taylor, M. B. 2005, in ASP Conf. Ser. 347, *Astronomical Data Analysis Software and Systems XIV*, ed. P. Shopbell, M. Britton, & R. Ebert (San Francisco, CA: ASP), 29
- Treu, T., Ellis, R. S., Liao, T. X., & van Dokkum, P. G. 2005, *ApJL*, 622, L5
- Treu, T., Roberts-Borsani, G., Bradac, M., et al. 2022, *ApJ*, 935, 110
- U. V., Hemmati, S., Darvish, B., et al. 2015, *ApJ*, 815, 57
- Übler, H., Maiolino, R., Curtis-Lake, E., et al. 2023, *A&A*, 677, A145
- Umeda, H., Ouchi, M., Nakajima, K., et al. 2024, *ApJ*, 971, 124
- Virtanen, P., Gommers, R., Oliphant, T. E., et al. 2020, *NatMe*, 17, 261
- Walmsley, M., Géron, T., Kruk, S., et al. 2023, *MNRAS*, 526, 4768
- Wang, B., Fujimoto, S., Labbé, I., et al. 2023, *ApJL*, 957, L34
- Whitaker, K. E., Ashas, M., Illingworth, G., et al. 2019, *ApJS*, 244, 16
- Williams, R. E., Blacker, B., Dickinson, M., et al. 1996, *AJ*, 112, 1335
- Williams, R. J., Quadri, R. F., Franx, M., van Dokkum, P., & Labbé, I. 2009, *ApJ*, 691, 1879
- Wirth, G. D., Willmer, C. N. A., Amico, P., et al. 2004, *AJ*, 127, 3121
- Wisnioski, E., Förster Schreiber, N. M., Wuyts, S., et al. 2015, *ApJ*, 799, 209
- Wolfe, A. M., Gawiser, E., & Prochaska, J. X. 2005, *ARA&A*, 43, 861
- Wright, L., Whitaker, K. E., Weaver, J. R., et al. 2024, *ApJL*, 964, L10
- Xue, Y. Q., Luo, B., Brandt, W. N., et al. 2016, *ApJS*, 224, 15
- Yan, H., & Windhorst, R. A. 2004, *ApJL*, 612, L93
- Yan, H.-J., Windhorst, R. A., Hathi, N. P., et al. 2010, *RAA*, 10, 867